Ψ_k Newsletter

AB INITIO (FROM ELECTRONIC STRUCTURE) CALCULATION OF COMPLEX PROCESSES IN MATERIALS

Number 108 December 2011

Editor: Z (Dzidka) Szotek
E-mail: psik-coord@stfc.ac.uk

Sponsored by: UK's CCP's and Psi-k

Contents

1 Editorial

In this last issue of the 2011 Psi-k Newsletter we have a number of workshop/meeting reports, job announcements and abstracts of newly submitted or recently published papers. Just before the scientific highlight there is a short information on opening of the ICTP South American Institute for Fundamental Research.

The scientific highlight article is by Christoph Friedrich, Markus Betzinger, Martin Schlipf, and Stefan Blügel (Jülich) and Arno Schindlmayr (Paderborn) on "Hybrid functionals and *GW* approximation in the FLAPW method".

For further details please check the table of content of this issue.

The *Uniform Resource Locator* (URL) for the Psi-k webpage is:

http://www.psi-k.org.uk/

Please submit all material for the next newsletters to the email address below.

The email address for contacting us and for submitting contributions to the Psi-k newsletters is

	function
psik-coord@stfc.ac.uk	**messages to the coordinators, editor & newsletter**

Z (Dzidka) Szotek, Martin Lüders, Leon Petit and Walter Temmerman
e-mail: psik-coord@stfc.ac.uk

2 Psi-k Activities

"Towards Atomistic Materials Design"

2.1 Reports on the Workshops supported by Psi-k

2.1.1 X-ray Spectroscopy : Recent Advances in Modelling and New Challenges

ETH Zurich

July 13, 2011 to July 15, 2011

CECAM, Psi-k, ESF

M. Iannuzzi, M. Odelius, D. Passerone

http://www.cecam.org/workshop-537.html

Scope of the workshop

Representatives for many different methods to simulate x-ray spectra have been gathered to present the state-of-the-art in the field and discuss the applicability and limitations of the available theoretical tools. Experimental specialists were also invited to show recently developed techniques, thus suggesting future challenges direction for future development of the theoretical methods.

The presentations of invited speakers and contributing talks were a mixture of method development and applications, which gave opportunities for lively discussions on technical details of the methods, as well as on the kind of physical properties that can be addressed and on general issues concerning the various level of theory and range of reliability. The crucial role of these methods in the interpretation and design of new experiments are obvious from the strong interest from the experimental groups and a continuous interplay between theory and experiment is valid to the field.

Main outcomes

A variety of advanced new computational approaches based on the Bethe-Salpeter equation, multi-configurational wave function methods and time-dependent density functional theory (DFT) have been discussed in depth. Several speakers presented new or renewed program packages a variety of features related to the calculation of x-ray spectra at different level of approximation, which points to a stimulating development in the field. Several cases of successful applications of the simplest transition potential DFT methods to both simple and large complex systems have

been illustrated. Among these, there were a few examples of disordered systems like polymers, molecular liquids and solutions, for which there is a need of extensive configurational sampling in extended systems. Applications on more realistic systems have become possible thanks to the implementation of X-ray spectroscopy tools within fast DFT based codes for simulations on condensed matter systems, like GPAW, CP2K, QuantumEspresso, and Wein2k. On the other hand, limitations of DFT methods have been highlighted in comparison to new results obtained from more advanced methods, which however are still strongly limited to small system size. Many contributions presenting new methodology from wave function based methods and response-theory formalism have shown that the field is extending into new areas. Although multi-configurational post-Hartree-Fock methods are only applicable to small systems, they serve as an important calibration schemes. This helps the evaluation of more approximated, providing a systematic way to improve the description of more and more complex effects, thus bringing new ideas for method development. One of the hot topics in the workshop was transition metal L-edge spectra, and the related issues affecting x-ray absorption, x-ray emission and resonant inelastic x-ray scattering. Presentations of experimental groups showed the rapid development of new techniques and facilities in this direction, pointing to an urgent demand for accurate theoretical tools. Especially, the new achievements in the field of time-resolved measurements pose new challenges for the interpretation of the spectra and the theoretical modeling. The speakers were positively inspired by the scope of the workshop and made reference to different methods in their presentations, which created an open minded atmosphere and stimulated frank discussions. The richness of comparison between experiments and electronic structure calculations seen at the workshop is expected to increase with new insights onto e.g. orbital ordering and x-ray spectro-microscopy. Indeed, the importance and strength of x-ray spectroscopy is that it enables studies of the electronic properties in which the length scales from experiment and theory is meeting.

From the discussion on the modeling of transition metal L-edge spectra, we can extract the following conclusions. The L-edge spectra of transition metals are particularly complicated and the simplified transition potential approach based on DFT does not reproduce the pre-edge features accurately. This is due to the lack of multi-configurational effects, which results in wrong intensity and energy positions of the peaks. It can be argued that TD-DFT has some success but the representation of the interaction between the core-hole and the excited electron is only approximate. But the conclusion seems to be that one has to resort to the Bethe-Salpeter equation methods to have real predictive power. However, more extensive testing in various applications is necessary to clarify this statement. The development of new techniques and sources for acquiring time-resolved x-ray spectra of chemical reactions is beginning to approach the time-scales were it is meaningful to speak about electronic changes during the reaction rather then just differences between the reactants and the products. Applications of time resolved spectroscopy in the field of solution chemistry, surface science, and solid state physics were presented.

Conclusive remarks

The announcement of this workshop was followed by strong interest and we got requests for attendance long after the official dead-line. This resulted in an almost full room for both the invited and contributed presentations. Thanks to the excellent facilities and support at ETH we also enjoyed a highly appreciated video conference with Vancouver, Canada. In the poster session, the foyer was crowded and lively discussions around the 25 poster presentations continued until late in the evening. Our aim to gather representative scientists working on many different branches in the field of x-ray spectrum calculations was achieved and was a key ingredient in the intense and balanced discussion about the performance and limitations of the methods. In some cases, however, the methodologies were not fully explored and it was not possible to reach conclusive and comprehensive statements of the applicability range of the methods. We suggest that a conference on similar topics should be organized in a few years time, when the new methodologies have matured, have a better chance of being successful . Applications to large systems primarily employed transition potential DFT calculations. As a consequence of the only partially conclusive discussion of the limitations of that approach, the issues with simulating large systems and sampling of configurations were not addressed very much.

We would look forward to a future workshop within a few years at a time when the recently developed methodologies are more mature and on a particular timely topic. That would inspire the participants to really provide prerequisites for a conclusive comparison of methods in particular applications

Program

Day 1 .
Introduction to problems and overview: Chair Michael Odelius

- 08:30 to 08:45 Welcome
- 08:45 to 09:30 Nils Martensson: New Opportunities for Multidimensional Electron Spectroscopy
- 09:30 to 10:15 Frank Neese:A new first principle approach to calculate transition metal L-edge spectra

Methods in core-level spectroscopy I: Chair Frank DeGroot

- 10:45 to 11:30 Benjamin Watts: Scanning Transmission X-ray Spectro-microscopy of Organic Materials
- 11:30 to 12:15 Lars Pettersson: X-ray spectroscopies and scattering applied to water: What can we learn from experiment and simulations?
- 12:15 to 12:45 Moniek Tromp: Development of XAS and XES techniques as a tool in homogeneous catalysis

Methods in core-level spectroscopy II: Chair John Rehr

- 14:00 to 14:45 Mauro Stener: TDDFT and DFT approaches for core electron excitations: molecules, bulk materials and large clusters
- 14:45 to 15:30 Patrick Norman: Response theory calculations of near-edge X-ray absorption and circular dichroism spectra
- 15:45 to 16:30 Nicholas A Besley: Development of Exchange-Correlation Functionals for Time-Dependent Density Functional Theory Calculations of Core Excitations
- 16:30 to 17:15 Delphine Cabaret: Successful and unsuccessful applications of DFT for XANES simulations and how to improve
- 17:15 to 17:45 Weijie Hua: X-ray spectroscopy of DNA

Poster Session wit Apero

Day 2 .
Time-resolved x-ray spectroscopy - experiment and theory: Chair Thomas James Penfold

- 08:30 to 09:15 Shaul Mukamel: Coherent Attosecond Multidimensional X-ray Spectroscopy of Molecules
- 09:15 to 10:00 Wilfried Wurth: Ultrafast dynamics in solids and at surfaces probed with time-resolved x-ray spectroscopy

Time-resolved x-ray spectroscopy - experiment and theory: Chair Wilfried Wurth

- 10:30 to 11:15 Thomas James Penfold: Time-resolved X-ray absorption spectroscopy
- 11:15 to 11:45 Amelie Bordage: Probing the electronic structure of Fe in switchable molecules using time-resolved hard X-rays spectroscopies
- 11:45 to 12:15 Enrique Sanchez Marcos: Coupling Computer Simulations and X-ray Absorption Spectroscopy for Solving the Structure of Metal Ion Solutions
- 12:15 to 12:45 Artur Braun: Application of x-ray and electron spectroscopy to energy materials

Methods in core-level spectroscopy III: Chair Lars Pettersson

- 14:00 to 14:45 John Rehr: Advances in the Theory of X-ray Spectra Beyond the Quasiparticle Approximation
- 14:45 to 15:30 Frank de Groot: Towards an ab-initio description of X-ray absorption spectra of transition metal systems
- 15:30 to 16:00 Sonia Coriani: Coupled Cluster Methods for X-ray absorption spectroscopy

Applications of x-ray spectroscopy: Molecules, Liquids, Materials: Chair Daniele Passerone

- 16:30 to 17:15 Serena DeBeer: Valence to Core X-ray Emission as a Novel Probe of Metal-Ligand Interactions
- 17:15 to 18:00 Peter Blaha: BSE calculations of L23 edges of transition metal compounds
- 18:00 to 19:00 George Sawatzky : The pros,cons and problem related selection of theoretical approaches to x-ray spectroscopies

Social dinner.

Day 3 .
Methods in core-level spectroscopy IV: Chair Mauro Stener

- 09:00 to 09:45 Calogero Natoli: Multiple Scattering Theory: a versatile tool for calculating x-ray spectroscopic response functions as well as ground state properties of a condensed matter system.
- 09:45 to 10:30 Peter Kruger: Multichannel multiple scattering calculations on dichroic L23-edge spectra of titanium oxide nanostructures
- 11:00 to 11:45 Eric Shirley: The NIST Core BSE program (NBSE) and OCEAN, its nearly Turn-key Implementation
- 11:45 to 12:30 Pieter Glatzel: Electronic structure analysis by hard X-ray photon-in/photon-out spectroscopy
- 12:30 to 13:00 Donat Adams: Characterization of conformational changes in small molecules and polymers by means of ab initio MD and X-ray absorption spectroscopy

Applications of x-ray spectroscopy: Catalysis, material science: Chair Marcella Iannuzzi

- 14:00 to 14:45 Jeroen Anton van Bokhoven: Application of X-ray absorption in catalysis
- 14:45 to 15:30 John Tse: X-rays at high pressures
- 15:30 to 16:00 Grigory Smolentsev: X-ray absorption and emission spectroscopy to study the local structure in coordination complexes

List of participants

Supported participants
Nicholas A BESLEY United Kingdom, University of Nottingham
Peter BLAHA Austria, Technical University Vienna
Artur BRAUN Switzerland, EMPA Swiss Federal Laborato...
Delphine CABARET France, University Pierre and Marie Curie, Paris
Frank DE GROOT The Netherlands, Utrecht University

Serena DEBEER USA, Cornell University, Ithaca
Pieter GLATZEL France, European Synchrotron Radiation Facility, Grenoble
Weijie HUA Sweden, Royal Institute of Technology, Stockholm
Peter KRUGER France, CNRS-Universite de Bourgogne, Dijon
Shaul MUKAMEL USA, University of California at Irvine
Nils MARTENSSON Sweden, Uppsala University
Calogero NATOLI Italy, Research Division INFN- LNF, Frascati
Frank NEESE Germany, University of Bonn
Patrick NORMAN Sweden, Linköping University
Thomas James PENFOLD Switzerland, Swiss Federal Institue of Technology
Lars PETTERSSON Sweden, Stockholm University
John REHR USA, University of Washington, Seattle
George SAWATZKY Canada, University of British Columbia, Vancouver
Eric SHIRLEY USA, National Institute of Standards and Technology, Gaithersburg
Mauro STENER Italy, University of Trieste
John TSE Canada, University of Saskatchewan, Saskatchewan
Jeroen Anton VAN BOKHOVEN Switzerland, Swiss Federal Institute of Technology, Zurich
Benjamin WATTS Switzerland, Paul Scherrer Institut, Villingen PSI
Wilfried WURTH Germany, University of Hamburg, Germany

Not supported participants
Donat ADAMS Switzerland, Empa - Materials Science andTechnology, Duebendorf
Joost BEUKERS The Netherlands, University of Twente
Amelie BORDAGE Hungary, Research Institute for Particle and Nuclear Physics, Budapest
Francois BOTTIN France, Commissariat a l Energie Atomique, Bruyares-le-Chatel
Marta Kinga BRUSKA Switzerland, Swiss Federal Institute of Technology, Zurich
Oana BUNAU France, University Pierre and Marie Curie
Pieremanuele CANEPA United Kingdom, University of Kent, Canterbury
Maria CHAN USA, Argonne National Laboratory
Sonia CORIANI Denmark, University of Aarhus
Fabiana DA PIEVE Belgium, University of Antwerp
Mario DELGADO-JAIME USA, Cornell University, Ithaca
Bernard DELLEY Switzerland, Paul Scherrer Institut
Arndt FINKELMANN Switzerland, Swiss Federal Institute of Technology, Zurich
Henrik GRÖNBECK Sweden, Chalmers University of Technolog, Göteberg
Mikko HAKALA Finland, University of Helsinki
Reshmi KURIAN The Netherlands, Utrecht University
Teodoro LAINO Switzerland, IBM Research - Zurich
Hongbao LI Sweden, Royal Institute of Technology, Stockholm
Mathias LJUNGBERG Sweden, Stockholm University
Yong MA Sweden, Royal Institute of Technology, Stockholm
Markus MEINERT Germany, Bielefeld University
Piter MIEDEMA The Netherlands, Utrecht University

Elena NAZARENKO Sweden, Gothenburg University
Weine OLOVSSON Sweden, Linköping University
Enrique SANCHEZ MARCOS Spain, University of Sevilla
Che SEABOURNE United Kingdom, University of Leeds
Ari Paavo SEITSONEN Switzerland, University of Zurich
Ondrej SIPR Czech Republic, Fyzikalni University, Prague
Grigory SMOLENTSEV Sweden, Lund University
Nikolay SMOLENTSEV France, European Synchrotron Radiation Facility, Grenoble
Xiuneng SONG Sweden, Royal Institute of Technology, Stockholm
Moniek TROMP Germany, Technical University Munich
Gyorgy VANKO Hungary, Research Institute for Particle and Nuclear Physics, Budapest
Min WU Canada, University of Saskatchewan, Saskatchewan

2.1.2 16th ETSF Workshop on electronic excitations (ETSF2011)

Turin Italy

26/9 to 1/10 2011

CECAM, Psi-k, ESF, and MaiMosine

Claudio Attaccalite, Myrta Grüning, Patrick Rinke, Matthieu Verstraete

http://www.tddft.org/ETSF2011/

Report

The 2011 ETSF conference was centered on building bridges between theorists and experimentalists in our key fields, namely time-resolved, X-Ray, photoemission, optical, and other spectroscopies. The conference was constructed around the different types of techniques, with one or two invited talks by prominent experimentalists, followed by theoretical contributed (and a few invited) talks. A few additional sessions were added to account for methodological and fundamental developments, but these were kept to a minimum in the 2011 instance of the conference. Overall the interaction was very efficient, featuring both the development of collaborations between theoreticians on excited states in electron systems, which is the hallmark of the ETSF network, and also between experimentalists and theoreticians. The former were asked to be both pedagogical and engaging in their talks, presenting their techniques in terms comprehensible to theoretical physicists, but also stimulating discussion and interactions by pointing out the frontiers and grey areas in experimental understanding.

The central location in Turin was a very efficient and agreeable venue, providing excellent facilities, transport, and restaurant and hotel services at reasonable prices.

The annual conference is also an important venue for organization between members of the growing European Theoretical Spectroscopy Facility. Steering committee and working group meetings were held before and after the conference. Important advances were made in structuring both the ETSF and the different themed collaboration teams, many of which echo specific preoccupations of Psi-k: electron correlation, electron-vibration coupling, and the simulation of large and/or biological systems. Several of the teams will submit workshop proposals to Psi-k in the coming application periods, as a result of organization carried out during this meeting.

Main themes addressed

Time resolved spectroscopies Femto and attosecond laser pulses are now engineered routinely in experiments on ultrafast chemistry and physics, probing and stimulating electron and nuclear dynamics on the shortest possible time scales. These systems remain extremely challeng-

ing experimentally, and were presented by Julia Stähler (FHI Berlin) and Franck Lépine (CNRS U Lyon), representing the different timescales of (respectively) vibrational and purely electronic phenomena. This area of spectroscopy has seen a huge increase in theoretical investment in the past 5-10 years, which has been tracked by the development of the corresponding beamline in the ETSF. Theoretical models to treat real-time and ultrafast dynamics were presented by invited speakers Fausto Rossi (Politecnico Torino) and Alexander V. Soudackov (Penn State), covering both advanced open quantum systems and non-adiabatic time evolution - two crucial topics linking time resolved and transport spectroscopies (see next subsection).

Nanoscale electron transport The transport properties of nano and atomic scale systems are the future of electronic devices, and one of the main driving forces for applied research in materials science. Latha Venkataraman (Columbia University) presented her ground breaking work on making nanoscale junctions reproducible, functional, and on understanding the electronic states and dynamics which determines the final macroscopic observables. Her existing collaborations with theoreticians in Density Functional Theory provided a clear demonstration of the symbiosis this conference wished to foster. The complex many-body physics which has been revealed in certain partly filled and spin-dependent nanoscopic junctions was Erio Tosatti (ICTP Trieste)

Photoemission spectroscopy The delicate nanoscale manipulation of electronic properties was demonstrated by Alexander Grüneis (U Vienna) who has tuned the band gap and electron phonon coupling of graphene through functionalization under CVD. Using angle resolved photoemission experiments exquisitely detailed information on electronic bands can be obtained, and compared directly to theoretical calculations, in particular many-body perturbation theory (MBPT). Two powerful and new implementations of MBPT were presented by Xavier Blase (CNRS Grenoble) using a Gaussian basis set for very large systems and by Stefan Blügel (FZ Jülich) using the FLAPW formalism for all-electron precision and heavy-element systems.

Vibrational spectroscopies Vibrational spectroscopies have several intersections with the themes mentioned above, through adiabatic effects and low energy excitations or renormalizations, and also stand alone as very popular and powerful tools for molecular and materials analysis. Johannes Neugebauer (U Braunschweig) presented systematic chemical-accuracy calculations of vibrational structure in large systems and resonant Raman spectroscopy. Nedjma Bendiab (U Lyon) studies nanoscale carbon structures using Raman and local probe microscopies. Long standing mysteries about the vibrational modes of graphite, graphene and carbon nanotubes can be answered and explained microscopically using these techniques.

Conclusion

The ETSF 2011 conference was a very successful edition, both through the rich interactions and the high quality of the experimental speakers which were attracted. Students benefitted extensively from the talks and informal discussions during coffee breaks, obtaining a systematic overview of the field of spectroscopy, both for cutting edge experimental techniques and the latest theoretical developments. The conference in this form was only possible thanks to vital sources of conference-specific funding provided by Psi-k, the ESF, MaiMoSine, and CECAM. The low conference fee and additional bursaries for students was particularly welcome in the

present context of wide budget cuts in science and travel funding in particular. Researchers from the USA, Italy, but also France and Spain would not have been able to come without the basic financial support provided to the conference. We look forward to continuing the ETSF conference series - the next edition will be at the University of Coimbra in Portugal, and return to the core business of the ETSF in the development of theory, algorithms, and code for the calculation of electronic excited states, and the wide variety of electronic correlations.

Program

Tuesday 27 September
Opening
Ultrafast changes of lattice symmetry at the onset of the photoinduced insulator-metal transition of VO2, Julia Staehler
Microscopic theory of energy dissipation and decoherence in open quantum devices, Fausto Rossi
Theoretical studies of ultrafast photoinduced proton-coupled electron transfer reactions, A.V. Soudackov
Coffee Break
Non-linear phenomena in time-dependent density-functional theory: What Rabi physics can teach us, Johanna Fuks
Size-consistency and fractional spin in Reduced Density-Matrix Functional Theory, Nicole Helbig
Exact exchange-correlation potentials for steady-state and time-dependent electronic systems, James Ramsden
Lunch
First-principles GW and BSE calculations for molecules of interest for organic photovoltaic applications, Xavier Blase
Physics with short light pulses: experiments and perspectives, Franck Lépine
First-principles study of the electronic and optical properties of ZnO and ZnS wurtzite nanoclusters, Giuliano Malloci
Exploring the conformations, stability, and dynamics of helix-forming alanine-based polypeptides: first-principles predictions and benchmarks, Mariana Rossi
Ab initio electronic spectra of peptides, Elena Molteni Effects of N-doping on the electronic properties of carbon atomic chains with distinct sp2 graphene-like terminations, G. Gueorguiev
Welcome Aperitif
ETSF general meeting CT reports and meetings

Wednesday 28 September
Electronic properties of functionalized graphene Alexander Gruneis
The GW approximation in the FLAPW method: Applications to Oxides and Topological Insulators, Stefan Blügel
Satellites in Valence Photoemission Spectroscopy, Matteo Guzzo
Coffee Break
Exotic quasi-one-dimensional systems: graphene-based superlattices, Lars Matthes

Optical response calculations of gold alloys from first principles, Deniz Kecik
Strong excitons in novel two-dimensional crystals: graphane, silicane and germanane, Friedhelm Bechstedt
Lunch + Poster Session
Towards a novel approach for the calculation of many-body Green's functions, Giovanna Lani
Exact solution for 2-particle Green's function: an alternative to Bethe Salpeter Equation, Lorenzo Sponza
Strong electronic correlation in the Hydrogen chain: a variational Monte Carlo study, Lorenzo Stella
Properties of the screened interaction in finite systems, Adrian Stan
Coffee Break
GW/BSE Calculations of X-ray Spectra, John Vinson
Many-pole models of inelastic losses and satellites in x-ray spectra, Joshua Kas
Solids under intense ultrafast excitations: a time-dependent Bethe-Salpeter approach, Andrea Marini
ASE: A programmable environment for calculations with many electronic structure codes, Ask Hjorth Larsen
The PRACE infrastructure Micael Oliveira
Short GUI demos, Massimo Conter, Flavio Abreu Araujo

Thursday 29 September
Kondo screening and antiscreening in electron transport across metallic and molecular magnetic nanocontacts, Erio Tosatti
Electronics and Mechanics of Single Molecule Circuits, L. Venkataram
Spatio-Temporal description of Quantum Transport, Björn Oetzel
Coffee Break
Ab initio many-body effects in TiSe2, Marco Cazzaniga
Electronic Structure of Dye-Sensitized TiO2 Clusters from G0W0, Noa Marom
Multi-pole models for the approximation of spectral properties in GW, Martin Stankovski
Lunch + Poster Session
Probing Excited-State Potential-Energy Surfaces by Theoretical Resonance Raman Spectroscopy, J. Neugebauer
Electronic and mechanical properties of sp carbon atomic nanowires, Nicola Manini
Electron-phonon coupling in STO, Bin Xu
Coffee Break
Bootstrap approximation for the exchange-correlation kernel of time-dependent density functional theory, S. Sharma
Special Quasirandom Structures: application to liquid systems, A. Mosca Conte
A unified description of ground and excited state properties of finite systems: the self-consistent GW approach, Fabio Caruso
Simple preconditioning for time-dependent density-functional perturbation theory, L. Lehtovaara
Social Dinner

Friday 30 September
Unravelling the properties of graphene and nanotubes with Raman spectroscopy, N. Bendiab
NMR and EPR with Density Functional Perturbation Theory, S. de Gironcoli
Coffee Break
The polarizability and hyperpolarizability of C and BN nanotubes. A quantum-mechanical simu- lation, Roberto Dovesi
Auger Recombination and Impact Ionization from first-principles: from bulk to nanocrystals, Marco Govoni
Excited state properties of TiO2 surfaces and nanostructures, Letizia Chiodo
Optical characterization of Au nanowires on Si(111) surfaces, Conor Hogan
Lunch
Phase transitions within the GW approximation, Matteo Gatti
Momentum Distribution and Renormalization Factor in Sodium and the Electron Gas, Valerio Olevano
Current issues in the description of charged defects: the case of hydrogen in amorphous silica, David Waroquiers
Coffee Break
Insights in the T-matrix approximation, Pina Romaniello
TDDFT dynamics for strongly correlated model systems, Claudio Verdozzi
Closing remarks
Collaboration Teams Meetings

Participant list

Adrian Stan, University of Jyvaskyla
Adriano Mosca Conte, University of Rome Tor Vergata
Amilcare Iacomino, CSIC and Nano-Bio Spectroscopy Group UPV/EHU
Andrea Cucca, LSI
Andrea Marini, University of Rome Tor Vergata
Anne Matsuura, Université Catholique de Louvain
Alexander Grueneis, Uni Wien and IFW Dresden
Alexander Soudackov, Pennsylvania State University
Ask Hjorth Larsen, Center for Atomic-scale Materials Design
Bendiab Nedjma, Institut Néel-Université Joseph Fourier
Bhaarathi Natarajan, University of Joseph Fourier
Bin XU, University of Liege
Björn Oetzel, IFTO
Bruno Bertrand, Université Catholique de Louvain
Christine Giorgetti, LSI - CNRS - Ecole Ploytechnique- CEA
Claudia Rödl, Ecole Polytechnique
Claudio Attaccalite, Insitut Neel

Claudio Verdozzi, Lund University
Conor Hogan, CNR-ISM and Univ. Rome Tor Vergata
Davide Sangalli, Laboratorio MDM, IMM, CNR
David Waroquiers, Université Catholique de Louvain
Deniz Kecik, Paul Scherrer Institut
Diakhate Momar, Universite de Liège
Elena Ferraro, Universit'a di Roma Tor Vergata
Elena Molteni, Department of Physics, University of Milan
Erio Tosatti, SISSA, ICTP, and CNR-IOM Democritos, Trieste
Faber Carina, Institut Néel
Fabio Caruso, Fritz-Haber-Institut der Max-Planck-Gesellschaft
Flavio Abreu Araujo, Université catholique de Louvain, IMCN
Francesca Risplendi, Politecnico di Torino
Francesco Sottile, Ecole Polytechnique
Franck Lépine, CNRS
Friedhelm Bechstedt, Friedrich-Schiller-Universit?at Jena
Gian-Marco Rignanese, Université Catholique de Louvain
Giovanna Lani, Ecole Polytechnique
Giovanni Onida, University of Milan
Giuliano Malloci, CNR - Istituto di Officina dei Materiali - SLACS
Gueorgui Gueorguiev, Linkoping University
Hans-Christian Weissker, CINaM-CNRS
James Ramsden, University of York
Johanna Fuks, University of Basque Country
Johannes Neugebauer, Technical University of Braunschweig
Joshua Kas, University of Washington
Julia St?ahler, Fritz-Haber-Institut der Max-Planck-Gesellschaft
John Vinson, University of Washington
Lars Matthes, University of Rome 'Tor Vergata'
Latha Venkataraman, Columbia University
Lauri Lehtovaara, Universite Claude Bernard Lyon 1
Letizia Chiodo, CBN@Unile, Istituto Italiano di Tecnologia IIT and ETSF
Linda Hung, Ecole Polytechnique
Lorenzo Sponza, LSI - Ecole Polytechnique, Palaiseau, France
Lorenzo Stella, Universidad del Pais Vasco
Lucia Caramella, Universita degli Studi di Milano (Italy)
Lucia Reining, CNRS
Marco Casadei, FHI Berlin
Marco Cazzaniga, Universit'a degli Studi di Milano
Marco Di Gennaro, Universite de Liege
Marco Govoni, Universit'a di Modena e Reggio Emilia
Mariana Rossi, FHI-Berlin
Martin Stankovski, Universite Catholique de Louvain-la-Neuve, Belgium

Matteo Bertocchi, LSI - Ecole Polytechnique
Matteo Gatti, UPV San Sebastian
Matteo Guzzo, Ecole Polytechnique, Palaiseau, France
Matthieu Verstraete, Universite de Liege, Belgium
Micael Oliveira, Universidade de Coimbra
Mocanu Marian, 'Politehnica' University of Bucharest (Romania)
Myrta Grüning, Universidade de Coimbra
Nader Slama, Ecole Polytechnique
Nicola Manini, University of Milano
Nicole Helbig, Universidad del Pais Vasco/FZ Jülich
Nicky Thrupp, Université Catholique de Louvain
Nikitas Gidopoulos, ISIS STFC
Noa Marom, University of Texas at Austin
Olivia Pulci, ETSF, Dept. of Physics University of Rome Tor Vergata
Pablo Garcia-Gonzalez, Universidad Autonoma de Madrid
Patrick Rinke, Fritz-Haber-Institut der Max-Planck-Gesellschaft
Pina Romaniello, Laboratoire de Physique Théorique, Université Paul Sabatier
Rex Godby, University of York
Roberto Dovesi, Torino University
Paola Gori, Istituto di Struttura della Materia
Pierluigi Cudazzo, University of the Basque Country
Samuel Poncé, Université Catholique de Louvain
Sangeeta Sharma, MPI Halle
Sri Chaitanya Das Pemmaraju, Trinity College Dublin
Stefan Blügel, Forschungszentrum Jülich
Stefano de Gironcoli, SISSA and CNR-IOM DEMOCRITOS
Ulf von Barth, Dept. of Mathematical Physics, Lund University
Valerio Olevano, CNRS, Institut Neel
Veniard Valerie, Laboratoire des Solides Irradies, Ecole Polytechnique, CNRS
Viviana Garbuio, Tor Vergata University, Rome
Xavier Gonze, Université Catholique de Louvain
Xavier Blase, Institut Néel, CNRS and Université Joseph Fourier
Yann Pouillon, Universidad del Pais Vasco UPV/EHU

2.1.3 Report on Workshop: Superconductivity 100 Years Later: A Computational Approach

P l a c e: Hotel Porto Conte, Alghero, Sardinia, Italy

D a t e: September 15, 2011 to September 18, 2011

S p o n s o r s: CECAM, Psi-k, ESF-Intelbiomat, Regione Sardegna

O r g a n i z e r s: Lilia Boeri (Max Planck Institute for Solid State Research, Stuttgart, Germany), Sandro Massidda (University of Cagliari, Italy), E.K.U. Gross (Max Planck Institute of Microstructure Physics, Halle, Germany)

Web Page: http://www.fkf.mpg.de/conf/sc100/

Report:

The workshop has been scientifically quite successful, the talks have been very interesting with many questions to all the speakers. Both at the round table and during the pauses of the scientific program there have been many discussions on the physics of superconducting materials and on the state-of-the-art and future of the field. Furthermore, all the participant have enjoyed the stimulating and friendly atmosphere of the meeting.

More in detail, the materials under attention have been mostly the pnictides, but also C-related materials as picene, graphene and intercalation graphite compounds, MgB_2, cuprates and ruthenates. For pnictides there has been a wide consensus on the magnetic origin of the superconducting mechanism. The major topics examined in these materials were: (i) the symmetry of the order parameter (Gonnelli, Singh, Mazin, Johannes), with a few experimental presentations (*e.g.* point-contact Andreev reflection spectroscopy, Gonnelli) and the corresponding implications on the nature of the pairing and on the strength of the pairing and electronic interactions; (ii) the nature of magnetism, the spin-fluctuation spectra and the relationship between magnetism and superconductivity (Antropov, Singh, Mazin, Johannes, Toschi); (iii) the importance of correlation effects (Cappelluti, Toschi, and the experimental presentation of the ARPES results by Borisenko); (iii) the role of impurities (Golubov); (iv) multiband effects within an Eliashberg approach (Golubov and Efremov, who substituted Dolgov). (v) the role of the quantum critical point (Mackenzie), renormalization group techniques (Honerkamp). (vi) Optical spectra and correlation effects (Cappelluti).

The talks on cuprates and ruthenates (*e.g.* J. Annet,) were also concerned with the problems of symmetry of the order parameter, magnetism and superconductivity and correlation. The problem of correlation has also been examined in the context of dynamical properties, within the DFT+U approach (Floris).

A significant part of the meeting has been devoted to electron-phonon superconductivity (EPS). Particular attention has been devoted to C-based materials and MgB_2 (Profeta, Yildirim, Calandra), to relativistic effects in Pb (Heid) ,and to experimental techniques to estimate the electron-phonon coupling (Carbone). Always within EPS, we mention the presentation of Sanna on the status of the density functional theory applied to the superconducting state (SCDFT). Sanna has shown how from the solution of the Sham–Schlüter equations it is possible to derive the Kohn-Sham superconducting gap, and finally obtain a critical temperature which follows very closely the Eliashberg result in the ideal test case where Coulomb interaction is turned off.

Finally, we mention two presentations (Bianconi and Peeters) where quantum effects become important at the nanoscale level.

Programme

		Friday, 16th September 2011
8:50:9:00	Opening remarks	
9:00-9:30	O. K. Andersen	Speculations about making nickelate high-temperature superconductors
9:30-10:00	C. Honerkamp	Unconventional superconductivity viewed by the functional renormalization group1s's recent applications
10:00-10:30	G. Profeta	How to make graphene superconducting
10:30-11:00		Coffee Break
11:00-11:30	F. Peeters	Quantum size effects in nano-scale superconductors
11:30-12:00	V. P. Antropov	Spin-fluctuations induced metallicity, and key magnetic interactions in super- conducting iron pnictides and selenides
12:00-12:30	S. Borisenko	Superconductivity and magnetism in iron pnictides
12:30-14:30		Lunch Break
14:30-15:00	R. S. Gonnelli	Directional point-contact Andreev-reflection spectroscopy of Fe-based superconductors: Gap symmetry and Fermi surface topology
15:00-15:30	O. V. Dolgov	Multiband Eliashberg Model for Pnictides
15:30-17:00		Short Poster Presentations
17:00-20:00		Poster Session
20:00-...	Dinner	

		Saturday, 17th September 2011
9:00-9:30	D. J. Singh	Superconductors Near Magnetism
9:30-10:00	A. Mackenzie	Phase formation in quantum critical systems
10:00-10:30	J. Annett	Intrinsic orbital magnetism and optical dichroism of the multi-band pairing state of the chiral superconductor Sr2RuO4
10:30-11:00		Coffee Break
11:00-11:30	F. Carbone	The electron-phonon coupling in strongly correlated solids studied by ultrafast techniques
11:30-12:00	A. Floris	Vibrational properties of MnO and NiO from DFT+U-based Density Functional Perturbation Theory
12:00-12:30	A. Sanna	State of the art and new developments in superconducting density functional theory
12:30-14:30	Lunch Break	
14:30-15:00	R. Heid	Electron-phonon coupling and superconductivity in bulk and thin films of lead: importance of relativistic corrections
15:00-15:30	T. Yildirim	Electron-Phonon Coupling From Finite-Displacement Approach: A Case Study for Metal Doped Picene and Fe-based Superconductors
15:30-16:00	M. Calandra	Adiabatic and non-adiabatic phonon frequencies in a Wannier function approach: applications to CaC6, MgB2 and K-doped Picene
16:00-17:30		Round Table
19:00-20:00		Poster Session
		Sunday, 18th September 2011
9:00-9:30	I. I. Mazin	Symmetry-allowed pairing states in overdoped 122 iron selenides
9:30-10:00	E. Cappelluti	Interband interactions and optical conductivity in iron-based superconductors
10:00-10:30	A. Bianconi	Shape resonances in multigap superconductors: a common pairing mechanism in pnictides, diborides and cuprates
10:30-11:00		Coffee Break
11:00-11:30	M. Johannes	Magnetism, superconductivity and spin fluctuations in Fe-based superconductors
11:30-12:00	A. A. Golubov	Strong impurity scattering in multiband superconductors
12:00-12:30	A. Toschi	Spectral and magnetic properties of the iron-based superconductors: The role of electronic correlations
12.30-12.50		Closing remarks
13:00-14:30		Lunch Break
14:30-19:00		Excursion

List of participants

1. Ole Krogh Andersen, Max Planck Institute for Solid State Research, Stuttgart, Germany
2. James Annet, HH Wills Physics Laboratory, United Kingdom
3. Vladimir Antropov, Ames Lab, ISU, Ames, USA
4. Fabio Bernardini, University of Cagliari, Italy
5. Christophe Bersier, Max-Planck-Institut für Mikrostrukturphysik, Halle, Germany

6. Antonio Bianconi, Universita' la Sapienza, Roma, Italy
7. Lilia Boeri, Max Planck Institute for Solid State Research, Stuttgart, Germany
8. Sergey Borisenko, IFW Dresden, Germany
9. Pawel Buczek, Max-Planck-Institut für Mikrostrukturphysik, Halle
10. Matteo Calandra, CNRS and IMPMC, Paris, France
11. Emmanuele Cappelluti, CNR-ISC, Rome, Italy
12. Fabrizio Carbone, EPFL, Lausanne, Switzerland
13. Michele Casula, CNRS et UPMC, Paris, France
14. Giorgio Concas, University of Cagliari, Italy
15. Lucian Covaci, University Antwerp, Belgium
16. Dario Daghero, Politecnico di Torino, Italy
17. Anatoly Davydov, Max-Planck-Institut für Mikrostrukturphysik, Halle, Germany
18. Luca de Medici, Laboratoire de Physique des Solides - Orsay, France
19. John K. Dewhurst, Max-Planck-Institut für Mikrostrukturphysik, Halle, Germany
20. Oleg Dolgov, Max Planck Institute for Solid State Research, Stuttgart, Germany
21. Dimitry Efremov, Max Planck Institute for Solid State Research, Stuttgart, Germany
22. Frank Essenberger, Max-Planck-Institut für Mikrostrukturphysik, Halle, Germany
23. Andrea Floris, King's College London, United Kingdom
24. Sara Galasso, Politecnico di Torino, Italy
25. Hennings Glawe, Max-Planck-Institut für Mikrostrukturphysik, Halle, Germany
26. Alexander Golubov, University of Twente, The Netherlands
27. Renato Gonnelli, Politecnico di Torino, Italy
28. Eberhard K.U. Gross, Max-Planck-Institut für Mikrostrukturphysik, Halle, Germany
29. Rolf Heid, Karlsruhe Institute of Technology, Karlsruhe, Germany
30. Carsten Honerkamp, RWTH Aachen, Germany
31. Michelle Johannes, Naval Research Laboratory, Washington, D.C., USA
32. Aleksey Kolmogorov, University of Oxford, United Kingdom
33. Andreas Linscheid, Max-Planck-Institut für Mikrostrukturphysik, Halle, Germany
34. Andrew Mackenzie, University of St Andrews, United Kingdom
35. Roxana Margine, University of Oxford, United Kingdom
36. Sandro Massidda, University of Cagliari, Italy
37. Bayan Mazidian, University Bristol, United Kingdom
38. Igor Mazin, Naval Research Laboratory, Washington, D.C., USA
39. Milorad Milosevic, University Antwerp, Belgium
40. Marco Monni, University of Cagliari, Italy
41. Luciano Ortenzi, Max Planck Institute for Solid State Research, Stuttgart, Germany
42. Francois Peeters, University of Antwerp, Belgium
43. Gianni Profeta, CNR - University of L'Aquila, Italy
44. Antonio Sanna, Max-Planck-Institut für Mikrostrukturphysik, Halle, Germany
45. Tobias Schickling, Philipps-Universität Marburg, Germany
46. Sangeeta Sharma, Max-Planck-Institut für Mikrostrukturphysik, Halle, Germany
47. David Singh, Oak Ridge National Laboratory, USA
48. Sergey Skornyakov, Institute of Metal Physics, Russian Academy of Sciences, Russia

49. Alaska Subedi, Max Planck Institute for Solid State Research, Stuttgart, Germany
50. Simone Taioli, Laboratorio Interdisciplanare di Scienze Computazionali, Trento
51. Alessandro Toschi, Technical University of Vienna, Austria
52. Taner Yildirim, NIST, USA
53. Paolo Zoccante, CNRS et UPMC, Paris, France

2.1.4 Report on Workshop CPMD2011: Extending the limits of ab initio molecular dynamics for Chemistry, Materials Science and Biophysics

Barcelona

September 5-9 2011

CECAM, ESF and Psi-k

Roberto Car, Michele Parrinello, Paolo Carloni and Carme Rovira

http://www.pcb.ub.es/cpmd2011

Summary

Density functional theory based molecular dynamics simulation (ab initio or Car-Parrinello MD) represented a milestone in computational physics and has dramatically influenced the methodology behind electronic structure calculations for solids, liquids and molecules. Ab initio MD is becoming a standard tool in molecular simulations of physical, chemical and biological processes. The CPMD2011 workshop aimed to be a platform for discussion of the latest progress in theory and applications, as well as defining the dominant trends in the field for the next years. The conference facilitated interactions betweenthe most prominent researchers working in this area and emerging young scientists in an informal environment. The lectures included new AIMD developments, metadynamics, QM/MM methods, CP2K, AIMD applications in materials science, chemistry and biochemistry, water and aqueous solutions and large scale simulations.

Clearly, the improvements of algorithms and increase in computer power have stimulated the field of AIMD in recent years. It is today possible to study problems of a level of complexity that was inconceivable ten years ago. The selected applications were intended not only to survey some of these problems, but also to highlight current limitations and future challenges. The topics of interest were the following: phase transformations, phase-change materials, thermoelectric materials, actinide materials, graphene, polyoxometalates, Li-air batteries, photo- and electrocatalysis, water/hydrophobic interfases, ionic liquids, chemical reactions in solution, enzymatic reactions, heme proteins, hydrogen oxidation and hydrogen production, anticancer prodrugs, photoactive proteins.

Scientific content

The conference lasted five days and it was organized as follows. The first half was oriented towards methods and AIMD applications in solid state physics and materials science, whereas the second half was devoted to chemistry and biochemistry. Due to the high number of posters

received (93) we decided to make two poster sessions. The full list of posters and abstracts are available at the conference web page.

Erio Tosatti opened the meeting with a speech on "Open problems problems in solid state physics" such as changes from Mott insulating to metallic and superconducting, friction and nanofriction, phase transitions, stick-slip sliding, etc. Some of these problems cannot be tackled with first-principles approaches yet, thus being future challenges. This was an aspect of discussion that continued specially after the plenary talks of Michael L. Klein ("HPC challenges for the next decade and beyond") and Giulia Galli ("On the search of sustainable energy sources").

There were several sessions dedicated to methods (especially metadynamics and QM/MM) and codes/tools (CPMD, CP2K and Plumed). One morning session was devoted to metadynamics, which enables the simulation of rare events and, as a consequence, the search for transition states and the exploration of reaction mechanisms of increasing complexity. The metadynamics session (Tuesday morning) covered recent advances such as well tempered MTD, bias exchange MTD and parallel tempering MTD, as well as the development of related tools (Plumed). Examples of application in materials science, physics, chemistry and biochemistry were presented during the rest of the meeting. The new methods being developed to enhance the sampling of the phase space generated a lively discussion on how to obtain quantitative energy data.

The description of van der Waals interactions (a well known shortcoming of the common DFT functionals) in AIMD simulations was discussed, specially after the talks of Robert DiStasio Jr. ("An efficient real-space implementation of the van der Waals energy and analytical forces in plane-wave ab initio molecular dynamics") and Pier Luigi Silvestrelli ("van der Waals interactions in DFT using wannier functions").

Starting with a plenary by Ursula Röthlisberger, the state of the art of hybrid methods (mainly QM/MM) was presented, following by a discussion on how to improve the computational overload and accuracy of such calculations. Other methods presented were those specifically devoted to calculation of acidity constants at interfaces (talk by Marialore Sulpizi), nuclear quantum effects (talk by Michele Ceriotti), neural network potential energy surfaces (talk by Jörg Behler), Montecarlo methods (talks by Ali Alavi and Leonardo Guidoni) and charge constrained density functional theory (talk by Jochen Blumberger). Three talks were focused on how to account for van der Waals interactions in DFT calculations. Concerning codes, Alessandro Curioni delivered a plenary on the state of CPMD code and new scalability frontiers in ab-initio MD. Starting with a plenary by Jürg Hutter, one afternoon session was devoted to CP2K, a very efficient AIMD code that is growing in importance as new capabilities are implemented.

On the topic of the simulation of chemical reactions, the talk of Pietro Vidossich on explicit solvent modeling in homogeneous cataysis showed that it starts to be feasible to model chemical reactions not only in aqueous environments. Irmgard Frank presented simulations of photoreactions and mechanically induced chemical reactions.

Because of the importance of classical simulations in many of the topics covered by the meeting (in the study of enzymatic reactions, for instance, classical simulations are the starting point of the QM/MM simulations, and metadynamics was initially formulated in the context of classical MD), we decided to open the meeting also to applications of classical approaches to favor constructive discussions on how to address realistic problems. (lectures by Jim Pfaendner, Modesto Orozco on biochemistry simulations, Davide Donadio and Jörg Behler on applications to mate-

rials science, for instance).
Answering relevant questions in Biochemistry and Biophysics requires modeling of large and complex systems. Quite impresive examples were presented such as Ribozyme/Protein systems, carbohydrate-building enzymes, heme proteins and DNA/RNA-processing enzymes. As discussed in the talk of Ursula Röthlisberger, size is not any more a problem (at least not so much as it used to be) but length still is. Therefore the development and continuous test of methods for enhancing the sampling of phase space becomes crucial.
Michele Parrinello closed the conference highlighting the quality of the research presented, the importance of the new programs and tools being developed (such as CP2K and Plumed). He also stressed the importance of accuracy issues in AIMD simulations.

To what extent were the objectives of the workshop achieved

The workshop excellently fulfilled the expectations of very high-level oral presentations and constructive discussions. Most participants were junior researchers, which is definitely a good point, but on the other hand they did not participate actively in the discussions, which were mainly centralized by senior researchers. The conference room was at full occupation during the complete meeting (even the last day), which is something not very common that tells about the high quality of the oral presentations.

Suggestions for new workshops/tutorials/conferences on the topic

Because of the high number of registrations (more than the size of the conference room can afford) we closed the registration some weeks before the deadline. Clearly, the topic of the conference, the low registration and accommodation fee and Barcelona itself, made the conference very attractive for both senior and young researchers (specially the last). We suggest that these aspects are taken into account for future CPMD conferences and that they should be planned for a higher number of participants (200-250). Due to the large number of topics presented, parallel sessions should also be considered.

CONFERENCE PROGRAM

Monday, September 5, 2011

08:00 − 09:30 Registration

09:30 − 10:00 Opening ceremony: Fernando Albericio (Director of Parc Científic de Barcelona, Spain) Michael Klein (Temple University, USA), Roberto Car (Princeton University, USA), Michele Parrinello (ETH Zurich), Carme Rovira (ICREA − Parc Científic de Barcelona)

10:00 − 10:50 Opening lecture (Chair: Michele Parrinello) by Erio Tosatti (International School for Advanced Studies, SISSA, Trieste, Italy). The most beautiful sea: open problems in solid state physics.

10:50 − 11:20 Coffee break

Session I: materials science (Chair: Giovanni Bussi). 11:20 − 11:50 Roman Martoňák (Comenius University Bratislava, Slovakia). Pressure-induced structural transitions in BN from ab initio metadynamics 11:50 − 12:20 Davide Donadio (Max Planck Institute for Polymer Science, Mainz, Germany). Thermal transport in thermoelectric materials 12:20 − 12:50 Jörg Behler (Lehrstuhl für Theoretische Chemie, Ruhr-Universität Bochum, Germany) Neural network potential energy surfaces for atomistic simulations

12:50 − 15:00 Lunch

15:00 − 15:50 Plenary II (Chair: Roberto Car). Giulia Galli (University of California, Davis, USA) It's all about energy and clean water

Session II: methods (Chair: Roberto Car) 15:50 − 16:20 Marialore Sulpizi (University of Mainz, Germany) Calculation of acidity constants at interfaces

16:20 − 16:40 Michele Ceriotti (University of Oxford, UK) Nuclear quantum effects in water by colored-noise path integral dynamics

16:40 − 17:00 Chao Zhang (German Research School for Simulation Sciences, Jülich, Germany) Excess proton at water/hydrophobic interfaces: an ab initio molecular dynamics study

17:00 − 18:30 Coffee break & POSTER SESSION I (odd numbers)

Tuesday, September 6, 2011

09:00 − 09:50 Plenary III (Chair: Ursula Röthlisberger). Michael L. Klein (Temple University, Pennsylvania, USA). HPC Challenges for the Next Decade and Beyond − From Discovery to Applications at the Nano-Bio-Med Frontier

Session III: metadynamics (Chair: Ursula Röthlisberger) 09:50 − 10:20 Giovanni Bussi (International Scho ol for Advanced Studies, SISSA, Trieste, Italy) Accelerated sampling of the conformational space in biomolecules: From small proteins to RNAs

10:20 − 10:40 Gareth Tribello (ETH Zurich, Lugano, Switzerland) Exploiting machine learning in enhanced sampling calculations

10:40 − 11:10 Coffee break

Session III: metadynamics (cont.) (Chair: Michael L. Klein)

11:10 − 11:40 Francesco Gervasio (Centro Nacional de Investigaciones Oncológicas, Madrid, Spain) Understanding the plasticity of oncogenic tyrosine kinases through experimentally validated ParallelTempering-metadynamics and PathCV calculations

11:40 − 12:00 Alessandro Barducci (ETH Zurich, Lugano, Switzerland) Determination of protein multimerization free-energy landscape using explicit-solvent MD simulations

12:00 − 12:20 Massimiliano Bonomi (University of California, San Francisco, USA) Enhanced sampling in the well-tempered ensemble

12:20 − 12:40 Xevi Biarnés (IQS-Universitat Ramon Llull, Barcelona, Spain) METAGUI − A new VMD extension to analyze and visualize metadynamics simulations

12:40 − 13:00 Albert Ardèvol (Parc Científic de Barcelona, Spain) How does nature make glycosidic bonds. A metadynamics investigation

13:00 – 15:00 Lunch

15:00 – 15:50 Plenary IV (Chair: Marialore Sulpizi) Jürg Hutter (University of Zurich, Switzerland). CP2K: Developments and Applications

Session IV: methods/CP2K (Chair: Marialore Sulpizi)

15:50 – 16:20 Matthias Krack (PSI Lugano, Switzerlad). Simulation of Actinide Materials

16:20 – 16:50 Joost Vandevondele (University of Zurich, Switzerland) Simulating large condensed phase systems with GGA and hybrid density functionals

16:50 – 17:20 Coffee break

Session IV: methods/CP2K (cont.) (Chair: Leonardo Guidoni)

17:20 – 17:50 Ivano Tavernelli (Ecole Federale Polytechnique de Lausanne, EPFL, Switzerland)Nonadiabatic molecular dynamics with explicit external electrostatic and electromagnetic fields

17:50 – 18:20 Ali Alavi (University of Cambridge, UK). Quantum Monte Carlo approach to the Full CI problem.

Wednesday, September 7, 2011

09:00 – 09:50 Plenary V (Chair: Paolo Carloni). Alessandro Curioni (IBM Zurich, Switzerland) New scalability frontiers in ab-initio MD

Session V: materials science (Chair: Paolo Carloni)

09:50 – 10:20 Marcella Iannuzzi (University of Zurich, Switzerland) Moire structure or nanomesh: the case of graphene and h-BN epitaxially grownon transition metals

10:20 – 10:40 Rustam Khaliullin (University of Zurich, Switzerland) Unraveling microscopic origins of complex behavior in carbon and sodium

10:40 – 11:10 Coffee break

Session V: materials science (cont.) (Chair: Agusti Lledos)

11:10 – 11:30 Antonio Rodriguez-Fortea (Universitat Rovira Virgili, Tarragona, Spain) Formation mechanisms of small polyoxometalates: a combined study using computational methods and mass spectrometry

11:30 – 12:00 Irmgard Frank (U. Hannover, Germany). First-principles simulation of chemical dynamics

12:00 – 12:30 Eduardo Hernández (Instituto de Ciencia de Materiales de Madrid, CSIC, Spain) Melting of lithium from first principles simulations

12:30 – 15:00 Lunch

15:00 – 15:50 Plenary VI (Chair: Simone Raugei). Annabella Selloni (Princeton University, USA) First principles simulations of materials and processes in photo- and electro-catalysis

Session VI: water / aq. solutions (Chair: Simone Raugei)

15:50 – 16:20 Chris Mundy (Pacific Northwest National Laboratory, PNNL, USA) A first-principles approach to understanding the specific ion effect

16:20 – 16:40 Robert A. DiStasio Jr. (Princeton University, USA) An efficient real-space implementation of the van der Waals energy and analytical forces in plane-wave ab initio molecular dynamics with applications to liquid water

16:40 – 17:00 Jun Cheng (University of Cambridge, UK) Oxidative dehydrogenation of water on aqueous rutile TiO2(110) from DFTMD simulations

17:00 – 18:30 Coffee break & POSTER SESSION II (even numbers)

Thursday, September 8, 2011

09:00 – 09:50 Plenary VII (Chair: Ute Röhriger). Ursula Röthlisberger (Ecole Federale Polytechnique de Lausanne, EPFL, Switzerland) About positive and negative catalysis: biochemistry with the Car-Parrinello method

Session VII: biochemistry (Chair: Ute Röhrig)

09:50 – 10:20 Mauro Boero (Institut de Physique et Chimie des Materiaux de Strasbourg, France) LeuRS Synthetase: A Reactive QM/MM Investigation of Water Mediated Editing Reactions in a Hybrid Ribozyme/Protein System

10:20 – 10:40 Mercedes Alfonso-Prieto (Temple University, Pennsylvania, USA) Understanding the redox properties of catalases by means of CPMD QM/MM calculations

10:40 – 11:10 Coffee break

Session VIII: chemistry (Chair: Elvira Guardia)

11:10 – 11:40 Marie-Pierre Gaigeot (Universite d'Evry val d'Essonne, France) DFT-based molecular dynamics simulations applied to vibrational spectroscopy. Illustrations on floppy polypeptides in the gas phase and immersed in the liquid phase, and on solid-liquid interfaces

11:40 – 12:10 Barbara Kirchner (University of Leipzig, Germany) Ionic liquids from ab initio molecular dynamics simulations

12:10 – 12:40 Pier Luigi Silvestrelli (University of Padova, Italy) Van der Waals interactions in DFT using Wannier functions

12:40 – 13:00 Pietro Vidossich (Universitat Autonoma de Barcelona, Spain) Explicit solvent modeling in homogeneous catalysis: selected case studies

13:00 – 15:00 Lunch

15:00 – 15:50 Plenary VIII (Chair: Carla Molteni). Marco Bernasconi (University ofMilano-Bicocca, Milano, Italy) Ab-initio simulations of phase change materials for data storage

Session IX: materials (Chair: Carla Molteni)

15:50 – 16:20 Jochen Blumberger (University College London, UK) Charge constrained density functional theory: implementation, successes and failures

16:20 – 16:50 Simone Raugei (Pacific Northwest National Laboratory, PNNL, USA) Ni(II) complexes for hydrogen oxidation and hydrogen production: an ab-initio MD investigation

16:50 – 17:20 Leonardo Guidoni (University of Rome, Italy) Geometry relaxation and vibrational spectroscopy by Quantum Monte Carlo 20:30 Conference dinner

Friday, September 9, 2011

Session XI: biochemistry (Chair: Emiliano Ippoliti)

09:30 – 10:00 Jim Pfaendner (University of Washington, Seattle, USA) Adventures in the well-tempered ensemble – getting more by spending less

10:00 – 10:30 Modesto Orozco (University of Barcelona, Spain) New aproaches to represent protein dynamics

10:30 – 11:00 Coffee break

Session XI: biochemistry (cont.) (Chair: Jochen Blumberger)

11:00 – 11:30 Alessandra Magistrato (International School for Advanced Studies, SISSA, Italy) Molecular mechanism of cancer disease investigated via molecular dynamics simulations

11:30 – 12:00 Mateo Dal Peraro (Ecole Federale Polytechnique de Lausanne, EPFL, Switzerland) Computational characterization of the catalytic two-metal-ion mechanism in DNA/RNA-processing enzymes

12:00 – 12:30 Michele Cascella (University of Bern, Switzerland) Understanding and engineering functionality of vitamin transporters of the CRAL-TRIO family by computer simulations

12:30 – 13:00 Carla Molteni (Kings College London, UK) Is green tea good for you? Insights from atomistic simulations

13:00 – 15:00 Lunch

Session XII: biochemistry (Chair: Mauro Boero)

15:00 – 15:20 Pablo Campomanes (Ecole Federale Polytechnique de Lausanne, EPFL, Switzerland) Molecular basis of novel anticancer prodrugs activation

15:20 – 15:50 Bern Ensing (University of Amsterdam, Netherlands) CPMD simulation of photoactive proteins in action

Session XIII: materials science (Chair: Mauro Boero)

15:50 – 16:20 Teodoro Laino (IBM Zurich, Switzerland) Toward the understanding of chemical degradation of aprotic solvents for Li-air batteries

16:20 – 16:40 Concluding remarks (Michele Parrinello)

16:40 Departure

LIST OF PRESENTED POSTERS

P1. Computer modelling of quantum effects by using classical mechanics. H. Dammak, M. Laroche, M. Hayoun, J. J. Greffet and Y. Chalopin.

P2. Amorphous TeGeI: Structure and Comparison with Similar Systems. Iva Voleska, Jaakko Akola and Tomas Wagner.

P3. Rationalizing the stereoselectivity of proline-catalyzed asymmetric aldol reactions in water. J. Ribas-Ariño, M.A. Carvajal, A. Chaumont and M. Masia.

P4. The conformational free energy landscape of 2−deoxy−b−D−glucopyranose by ab initio metadynamics. Implications for catalysis of b−glycosidases. Javier Iglesias-Fernandez, Albert Ardevo1, Xevi Biarnés, Antoni Planas and Carme Rovira.

P5. Density Functional Surface Stability Study of Oxidized Cu(110)/AFM Tip identification. J. Bamidele, Y. Kinoshita, T. Satoh, S. H. Lee, Y. Naitoh, Y. J. Li et al.

P6. Molecular Modeling of Interfacial Proton Transport in Polymer Electrolyte Membranes. Swati Vartak, Ata Roudgar and Michael Eikerling.

P7. Force-transformed free energy surfaces. Przemyslaw Dopieralski, Jordi Ribas-Arino and D. Marx.

P8. Protonation states of active site of class C b−lactamase. Ravi Tripathi and Nisanth N. Nair.

P9. AIMD study of the mechanism of Wacker reaction. Janos Daru and Andras Stirling.

P10. Oxidative addition of water and spontaneous formation of H2 at rhodium/alumina interface. Tushar K Ghosh and Nisanth N. Nair.

P11. The role of water in metal catalyzed transfer hydrogenation. Anna Pavlova and Evert J. Meijer.

P12. Solvent reorganization effect on electron transfer to a flavin molecule. Murat Kilic and B. Ensing.

P13. Superhalogen molecules as strong electron acceptors. Celina Sikorska and Piotr Skurski.

P14. First principles study of LiNH2/Li2NH hydrogen storage system. Giacomo Miceli, M. Ceriotti, C. Cucinotta, M. Bernasconi, M. Parrinello.

P15. Frequency modulation of vibrational N-H modes by collective molecular motions in porphycene from ab initio calculations and IR spectroscopy. Łukasz Walewski, Sylwester Gawinkowski, Jacek Waluk and Bogdan Lesyng.

P16. Ethylene polymerization processes catalyzed by half-metallocene titanium(IV) complexes − molecular dynamics approach. Łukasz Pikekos, Artur Michalak.

P17. Ab initio molecular dynamics study of finite temperature and pressure effects on the structural and electronic properties of the SiC/double layer graphite interface. A. M. Ukpong and Nitthaya Chetty.

P18. Atomic level characterisation of the binding and secretion of FHA by the TpsB transporter FhaC. Harish Kumar Ravi, Francesca Collu and Michele Cascella.

P19. Ab initio molecular dynamics simulation and free energy exploration of copper (I) complexation by chloride and bisulphide in hydrothermal fluids. Yuan Mei, D. M Sherman, J. Brugger and W. Liu.

P20. Ab Initio Molecular Dynamics Simulations for Endocyclic Cleavage-Induced Anomerization Reactions of Glycosides. Hiroko Satoh, Teodoro Laino, and Jürg Hutter.

P21. Activation parameters and their variation from molecular simulation. Christof Drechsel-Grau and Michiel Sprik.

P22. Vibrational Spectroscopy of Biomolecules by mixed Quantum/Classical Molecular Dynamics. Daniele Bovi, R. Spezia, A. Mezzetti, R. Vuilleumier, M.-P. Gaigeot, L. Guidoni.

P23. In Silico Prescreening of Computanionally Designed Enzymes. Bernardo Sosa Padilla Araujo, Thomas F. Miller III and Stephen L. Mayo

P24. Ab initio molecular dynamics study of AunTi clusters. J. Beloševic-Cavor, V. Koteski and J. Radakovic.

P25. Computation of equilibrium isotope fractionation between minerals and aqueous solutions. Piotr M. Kowalski and Sandro Jahn.

P26. Spectroscopic fingerprint of water around small hydrophobic solutes. Maria Montagna, Fabio Sterpone, and Leonardo Guidoni.

P27. Quantum Monte Carlo methods for molecular polarizabilities within a hybrid QMC/MM scheme. Emanuele Coccia and Leonardo Guidoni

P28. Modelling solute-solvent interactions in molecular liquids. Ling Ge

P29. Ab Initio Molecular Dynamics Simulations of Aqueous Glycine Solutions: Solvation Structure and Vibrational Spectra. Jian Sun, Harald Forbert, and Dominik Marx.

P30. Computational studies on the selectivity of a−tocopherol transfer protein. R. Helbling, W. Aeschimann, F. Simona, A. Stocker and M. Cascella.

P31. Deamidation of Peptides: Succinimide Hydrolysis Pathways. Saron Catak, Bart De Sterck, Rosa E. Bulo, Michel Waroquier and Veronique Van Speybroeck.

P32. Solvation properties of alkai and halide ions in water from Car-Parrinello molecular dynamics simulations. Ausias-March Calvo, M. Masia, I. Skarmoutos, and E. Guardia.

P33. Structure, Dynamics and Computational Vibrational Spectroscopy for Ac−Alan−LysH+ Peptides (n = 5, 10, 15). Mariana Rossi, V. Blum, A. Tkatchenko, and M. Scheffler.

P34. Modeling of non-adiabatic transitions in energetic materials. Andrey Mukhanov and V. Stegailov

P35. Density Functional Evaluation of the Composition, Charge, and Magnetic Structure of Nitrogenase FeMo-Cofactor. Travis V. Harris and Robert K. Szilagyi

P36. Adsorption of hydrazine (N2H4) and fluoroform (F3CH) on hexagonal ice(0001): first principles investigations on blue-shifted hydrogen bonds and the mechanism of chirality changes. Pawel Rodziewicz and Bernd Meyer.

P37. The role of d-shell polarization in the dynamics of nanocluster collisions. Ricardo Ramrez, F. Muñoz, M. Kiwi, G. Garcia, J. Rogan and J. A. Valdivia

P38. DFT and Molecular Dynamic study of metal ions in different solvents. N. Sadanandam, Srinivas Tulishetti, and Jayant K. Singh.

P39. Magnetostructural Dynamics of a Rieske-type 2Fe−2S Protein. Md. Ehesan Ali, Nisanth N. Nair, Volker Staemmler, and Dominik Marx.

P40. Stochastic Optimization of Capping Potentials for Hybrid QM/MM Calculations. Christoph Schiffmann, Daniel Sebastiani.

P41. Scaling and convergence of all-atom DFT calculations by order-N density-matrix-based methods. Antonio S. Torralba, Tsuyoshi Miyazaki and David R. Bowler.

P42. The nature of PdCl2(C2H4)(H2O) as active species in the wacker process. New insights from ab initio molecular dynamics simulations. Gábor Kovacs, Andras Stirling, Agusti Lledos and Gregori Ujaque.

P43. Ab initio molecular dynamics simulation of proton transport in a biological ion channel. Jens Dreyer, Chao Zhang, Emiliano Ippoliti, Paolo Carloni.

P44. The mechanism of ozonolysis on C70 fullerene surface. The influence of endohedral noble gas substituent. Andrzej Bil, Zdzislaw Latajka, Carole A. Morrison.

P45. Electronic and optical properties of carotenoids: The case of Peridnin. Daniele Varsano and Leonardo Guidoni.

P46. Predicting color tuning in opsin proteins: A difficult case for first-principle methods? Omar Valsson

P47. EPR spectral lineshapes via ab initio MD simulations. Hossam Elgabarty and Daniel Sebastiani

P48. Physisorption and diffusion pathways of H2 molecule on graphene by first principle calculations. Francesca Costanzo, Francesco Ancilotto and Pier Luigi Silvestrelli

P49. First principles molecular dynamics simulation of liquid cyclopentasilane. Pham Tien Lam, Tatsuya Shimoda, Nobuo Otsuka and Dam Hieu Chi

P50 Proton transport mechanisms in phosphorus oxoacids. L. Vilciauskas, M. E. Tuckerman, G. Bester, S. J. Paddison, K.-D. Kreuer

P51. An Efficient Novel Method for Smooth and Adaptive MM−QM Switching. M. Böckmann, N.L. Doltsinis and D. Marx

P52. Study of cisplatin and transplatin binding to the copper transporter Ctr1 from QM/MM and classical MD simulations. T. H. Nguyen, E. Ippoliti, F. Arnesano, G. Natile and P. Carloni

P53. Structure and solvation effects on ionic liquids. Alfonso S. Pensado, Martin Brehm, Barbara Kirchner

P54. Protonation of a hydroxide anion bridging two divalent magnesium cations in water. Jung Mee Park and Mauro Boero

P55. Excited state solvation dynamics of a molecular THz probe. Christoph Allolio and Daniel Sebastiani

P56. Investigation of the CO2 reaction mechanisms on Ni-clusters deposited on a CeO2(111) surface using CP2K. K. Hahn, A. Seitsonen and J. Hutter

P57. Density Functional Theory study on the Molecular Structure and Reactivity of 5-fluorouracil. Iskra Koleva, Paulina Gorolomova and Galina Gencheva

P58. Infrared gas phase spectra of strongly hydrogen bonded ammonia hydrogen halides complexes obtained from CPMD simulations. Pawel Panek and Zdzislaw Latajka

P59. Determination of the potential energy surface of small molecules via Quantum Monte Carlo for the calculation of equilibrium structures and harmonic frequencies. A. Zen, M. Barborini, D. Zhelyazov, S. Sorella and L. Guidoni

P60. Theoretical study on coordination ability of the ligands 2,2−Dipyridylamine and 2,2−Dipyridylketone. Paulina Gorolomova and Galina Gencheva

P61. Spectral tuning by protein field on peridinin molecules in two different forms of Peridinin - Chlorophyll a − Protein. Gaia Di Paolo and Leonardo Guidoni

P62. Hydrophobicity and hydrophilicity in ionic liquids: Car-Parrinello and classical molecular dynamics simulation. Mohammad H. Ghatee, Amin Reza Zolghadr and F. Moosavi

P63. Reconstruction of the Free Energy Surface of a Transition metal Catalyzed Reaction. Eva Perlt, M. Brssel, P. di Dio and B. Kirchner

P64. Calculation of the electronic structure of graphdiyne. Željko Crljen and G. Baranovic

P65. Cyclization reaction of trimeric aluminium complexes studied by ab initio metadynamics. G. Lanzani, A. P. Seitsonen, M. Iannuzzi, J. Hutter and S. O. Pehkonen

P66. Model systems approach to the study of UV light stimulated DNA-proteins crosslink reaction. Marco Micciarelli, C. Altucci, R. Velotta, B. Curchod, I.Tavernelli, U. Roethlisberger.

P67. A concerted triple-jump in the recombination of hydronium and hydroxide Ions. Ali Hassanali, Meher Prakash, Hagai Eshet and Michele Parrinello

P68. Atomistic simulation of the interaction of an electrolyte with graphite nanostructures. A. V. Lankin, G. E. Norman and V. V. Stegailov

P69. NCO weak bond as a solvation probe. D. Kozlowski, J. Pilmé and P. Fleurat-Lessard

P70. Charge localization dynamics induced by oxygen Vacancies on the TIO2(110) Surface and titania and gold-promoted titania surfaces interaction with small molecules. Matteo Farnesi Camellone and D. Marx

P71. Combining ab-initio molecular dynamics with a dipole-field model to study acid dissociation reactions. Patrick Maurer, Vibin Thomas and Radu Iftimie

P72. Theoretical investigation of the amino acid − titania interaction. S. Köppen, J. Bartels, W. Friedrichs, L. Colombi Ciacchi and W. Langel

P73. Catalytic synthesis of methanol over cu/zno: exploration of energy surfaces for determining adsorption sites for CO2. L. Martínez-Suárez, J. Frenzel, B Meyer and D. Marx

P74. Massively parallel applications in biophysics by using CPMD. Emiliano Ippoliti, Chao Zhang, Jens Dreyer and Paolo Carloni

P75. Predicting new crystal structures from first-principles. D. Schärf and T. Kühne

P76. Reaction pathways for the pyrolysis of glycerol, propylene glycol and triacetin in the gas phase and at solid surfaces. C. Tuma, T. Laino, A. Curioni, E. Jochnowitz and S. Stolz

P77. Tully's surface hopping method in practice: FIREBALL calculations of photoactive organic materials. Enrique Abad, James P. Lewis , Pavel Jelínek and José Ortega

P78. The interactions of nitrogen dioxide with graphene and with Rh clusters stabilized by graphene. Sara Furlan and Paolo Giannozzi

P79. Acidity constants of the $\beta-$MnO2 (110) surface from Density Functional Theory based molecular dynamics. J. A. Kattirtzi, J. Cheng, M. Sulpizi and M. Sprik

P80. Synthesis, characterization and modeling of ruthenium catalysts for water oxidation. Jose Luis Valles Pardo, M. C. Guijt, Khurram S. Joya, Francesco Buda and Huub J.M. de Groot

P81. A novel grand-canonical approach towards linear scaling: Application to liquid methane under extreme conditions. Dorothee Richters, M. Ceriotti and T. D. Kühne

P82. Supramolecular packing and hydrogen bonding in organic functionalized materials from first principles. Dmytro Dudenko, D. Sebastiani, M. Ryan Hansen and H. W. Spiess

P83. New insights into polonium solution chemistry. R. Ayala, J. M. Martinez, R. R. Pappalardo and E. Sanchez-Marcos

P84. IR spectra of some model complexes of biological importance from Born-Oppenheimer molecular dynamics calculations. Artur Smaga, Joanna Sadlej, Łukasz Walewski and Bogdan Lesyng

P85. Study of the structure of chalcogenide glasses by ab initio molecular dynamics and 77Se NMR simulation. Kateryna Sykina, C. Roiland, L. Le Polles, B. Bureau and Eric Furet

P86. Improving the convergence of estimators in path integral molecular dynamics via higher order Trotter factorization schemes. Alejandro Perez and Mark E. Tuckerman

P87. Thermodynamics of electron flow in the bacterial decaheme cytochrome MtrF. Marian Breuer, P. P. Zarzycki, K. M. Rosso and J. Blumberger

P88. Catalytic itinerary in 1,3-1,4-$\beta-$glucanase unraveled by QM/MM metadynamics. X. Biarnés, A. Ardevo1, A. Planas, C. Rovira.

P89. Locality and fluctuations: trends in imidazolium-based ionic liquids and beyond. Katharina Wendler, S. Zahn, F. Dommert, R. Berger, C. Holm, B. Kirchner and L. Delle Site

P90. The role of hydrogen bond in water diffusion. Qu Chen, Yingchun Liu, Qi Wang and K. E. Gubbins

P91. Understanding the instability of IRMOF-1 in humid environments. Luca Bellarosa and N. Lopez

P92. On binding and reactivity of potent covalent inhibitors of fatty acide amide hydrolase. G. Palermo, M. Neri, P. Campomanes, I. Tavernelli, A. Cavalli, U. Röthlisberger and M. De Vivo

P93. First step in the charge separation process in the reaction center of photosynthetic bacteria. Thomas Eisenmayer

ABSTRACTS OF PRESENTED PAPERS: The book of abstracts (7MB) is available at the conference web page (http: //www.pcb.ub.es/cpmd2011/)

LIST OF PARTICIPANTS

ORGANIZERS

1. Roberto Car (Princeton University, USA)
2. Michele Parrinello (ETH Zurich, Switzerland)
3. Paolo Carloni (German Research School, Germany)
4. Carme Rovira (ICREA - Parc Científic de Barcelona, PCB, Spain)

PLENARY SPEAKERS

5. Giulia Galli (University of California, Davis, USA)
6. Ursula Röthlisberger (EPFL Lausanne, Switzerland)
7. Michael L. Klein (Temple University, USA)
8. Erio Tosatti (SISSA, Trieste, Italy)
9. Annabella Selloni (University of Princeton, Princeton, USA)
10. Marco Bernasconi (University of Milano, Italy)
11. Jürg Hutter (University of Zurich, Switzerland)
12. Alessandro Curioni (IBM Research, Zurich, Switzerland)

INVITED SPEAKERS

13. Roman Martoňák (Comenius University, Bratislava, Slovakia)
14. Carla Molteni (Kings College, London, UK)
15. Marialore Sulpizi (University of Mainz, Germany)
16. Jochen Blumberger (University College London, UK)
17. Irmgard Frank (University of Hannover, Germany)
18. Mauro Boero (CNRS, Strasbourg, France)
19. Ali Alavi (University of Cambridge, Cambridge, UK)
20. Marcella Iannuzzi (PSI Villingen, Switzerland)
21. Chris Mundy (PNNL Richland, Washington, USA)
22. Alessandra Magistrato (SISSA, Trieste, Italy)
23. Simone Raugei (PNNL, Richland, Washington, USA)

24. Barbara Kirchner (University of Leipzig, Germany)
25. Pier Luigi Silvestrelli (University of Padova)
26. Jörg Behler (Ruhr-Universität, Bochum, Germany)
27. Eduardo Hernández (CSIC, Madrid, Spain)
28. Teodoro Laino (IBM Research, Zurich)
29. Bern Ensing (University of Amsterdam)
30. Francesco Luigi Gervasio (CNIO, Madrid, Spain)
31. Michele Cascella (Universität Bern, Switzerland)
32. Joost Vandevondele (University of Zurich, Switzerland)
33. Marie-Pierre Gaigeot (Université d'Evry val d'Essonne, France)
34. Ivano Tavernelli (EPFL Lausanne)
35. Leonardo Guidoni (University of Rome, Italy)
36. Jim Pfaendtner (University of Washington, USA)
37. Giovanni Bussi (SISSA, Trieste, Italy)
38. Mateo Dal Peraro (EPFL Lausanne, Switzerland)
39. Michele Ceriotti (University of Oxford, UK)
40. Rustam Khaliullin (University of Zurich, Switzerland)
41. Gareth Tribello (ETH Zurich, Switzerland)
42. Massimiliano Bonomi (University of California, USA)
43. M. Alfonso-Prieto (Temple University, USA)
44. Pietro Vidossich (Universitat Autònoma de Barcelona, Spain)
45. Xevi Biarnés (Universitat Ramon Llull, Barcelona)
46. Pablo Campomanes (EPFL Lausanne)
47. Chao Zhang (German Research School, Jülich, Germany)
48. Antonio Rodríguez-Fortea (University Rovira i Virgili, Tarragona, Spain)
49. Robert DiStasio (Princeton University, USA)
50. Jun Cheng (Emmanuelle College, London)
51. Albert Ardèvol (Parc Científic de Barcelona, Spain)
52. Alessandro Barducci (ETH Zurich, Switzerland)
53. Davide Donadio (Max Plank Institute for Polymer Science, Mainz, Germany)
54. Matthias Krack (Paul SCherrer Institute, Switzerland)
55. Modesto Orozco (IRB Barcelona, Spain)

REST OF PARTICIPANTS

56. Enrique Abad, Universidad Autònoma de Madrid, Spain
57. Md. Ehesan Ali, Ruhr-Universität Bochum, Germany
58. Christoph Allolio, FU Berlin, Germany
59. Regla Ayala, Universidad de Sevilla, Spain
60. David Balcells, Universitat Autònoma de Barcelona, Spain.
61. Samuel Baltazar, Universidad de Santiago de Chile, CHile
62. Radhakrishnan Balu, US Army Research Lab, USA
63. Joseph Bamidele, Kings College London, UK
64. Albert Bartok-Partay, University of Cambridge, UK
65. Luca Bellarosa, Institut Català d'Investigació Química (ICIQ), Spain
66. Jelena Beloševic−Cavor, Institute of Nuclear Sciences Vinca, Serbia
67. Andrzej Bil, University of Wroclaw, Poland
68. Marcus Böckmann, Ruhr-Universität Bochum, Germany
69. Josep Maria Bofill, Universitat de Barcelona, Spain
70. Monika Borkowska-Panek, University of Wroclaw, Poland
71. Daniele Bovi, University of Rome, Italy
72. Marian Breuer, University College London, UK
73. Ausias March Calvo, Universitat Politècnica de Catalunya, Spain
74. Alejandro Torres, Parc Científic de Barcelona, Spain
75. David Cantu, Iowa State University, USA
76. Rodrigo Casasnovas, Universitat de les Illes Balears, Spain
77. Saron Catak, Ghent University, Belgium
78. Qu Chen, Zhejiang University, China
79. Jun Cheng, University of Cambridge, UK
80. Nithaya Chetty, University of Pretoria, South Africa
81. Emanuele Coccia, University of Rome, Italy
82. Francesca Costanzo, University of Padova, Italy
83. Željko Crljen, Rudjer Boskovic Institute, Croatia
84. Hichem Dammak, Ecole Centrale Paris, France
85. Janos Daru, HAS Chemical Research Center, Hungary
86. Gaia Di Paolo, CNISM, Italy
87. Przemyslaw Dopieralski, Ruhr-Universität Bochum, Germany

88. Christof Drechsel-Grau, Ruhr-Universität Bochum, Germany
89. Jens Dreyer, German Research School for Simulation Sciences, Germany
90. Dmytro Dudenko, Max Planck Institute for Polymer Research, Germany
91. Thomas Eisenmayer, University of Leiden, Netherlands
92. Hossam Elgabarty, FU Berlin, Germany
93. Matteo Farnesi Camellone, Ruhr-Universität Bochum, Germany
94. Sara Furlan, University of Trieste, Italy
95. Alberto Garcia, Institut de Ciència de Materials de Barcelona-CSIC, Spain
96. Ling Ge, Imperial College, UK
97. Paulina Gorolomova, Sofia University, Bulgaria
98. Elvira Guardia, Universitat Politècnica de Catalunya, Spain
99. Konstanze Hahn, University of Zurich, Switzerland
100. Travis Harris, University of Montana, USA
101. Ali Hassanali, ETH Zurich, Switzerland
102. Marc Hayoun, CEA-Ecole Polytechnique, France
103. Rachel Helbling, Universität Bern, Switzerland
104. Javier Iglesias-Fernández, Parc Científic de Barcelona, Spain
105. Mehmet Ali, Ilhan Universität Duisburg-Essen, Germany
106. Ivan Infante, Universidad Pais Vasco, Spain
107. Emiliano Ippoliti, German Res. Sch. Simul. Sci., Germany
108. Tushar Kanti Ghosh, Indian Institute of Technology Kanpur, India
109. John Kattirtzi, University of Cambridge, UK
110. Murat Kilic, University of Amsterdam, Netherlands
111. Iskra Koleva, Sofia University, Bulgaria
112. Susan Köppen, University of Bremen, Germany
113. Gábor Kovacs, Universitat Autònoma de Barcelona, Spain
114. Piotr Kowalski, GFZ German Research Centre for Geosciences, Germany
115. David Kozlowski, CEA, DAM, DIF, France
116. Katarzyna Kulczycka-Mierzejewska, University of Warsaw, Poland
117. Giorgio Lanzani, University of Oulu, Finland
118. Agusti Lledos, Universitat Autònoma de Barcelona, Spain
119. Luis Martinez Suarez, Universitat Autònoma de Barcelona, Spain
120. Gerald Mathias, LMU Munich, Germany
121. Patrick Maurer, Private, Switzerland

122. Eloi Marin, Parc Científic de Barcelona
123. Yuan Mei, The University of Adelaide, Australia
124. Marco Micciarelli, EPFL Lausanne, Switzerland
125. Giacomo Miceli, Università Milano-Bicocca, Italy
126. Letif Mones, University of Cambridge, UK
127. Alessandro Monesi, University of Bolonia, Italy
128. Maria Montagna, University of L Aquila, Italy
129. M. Merced Montero-Campillo, Universidade do Porto, Portugal
130. Andrey Mukhanov, Joint Institute for High Temperature of RAS, Rusia
131. Víctor Muñoz, Universitat Autonoma de Barcelona, Spain
132. Sadanandam Namsani, Indian Institute of Technology Kanpur, India
133. Trung Hai, Nguyen German Res. School for Sim. Sciences, Germany
134. Elisabeth Ortega, Universitat Autonoma de Barcelona, Spain
135. Manuel Angel Ortuno, Universitat Autònoma de Barcelona, Spain
136. Giulia Palermo, EPFL Lausanne, Switzerland
137. Pawel Panek, University of Wroclaw, Poland
138. Jung Mee Park, Korea Institute for Advanced Study, Korea
139. Anna Pavlova, University of Amsterdam, Netherlands
140. Alejandro Perez Paz, University of the Basque Country, UPV/EHU, Spain
141. Eva Perlt, University of Leipzig, Germany
142. Tien Lam Pham, Japan Advanced Institute of Science and Technology, Japan
143. Łukasz Piekos, Jagiellonian University, Poland
144. Ricardo Ramirez, Universidad Catolica, Chile
145. Harish Ravi, Universität Bern, Switzerland
146. Jordi Ribas, Universitat de Barcelona, Spain
147. Dorothee Richters, Universitaet Mainz, Germany
148. Luis Rodriguez, Universitat Autonoma de Barcelona, Spain
149. Pawel Rodziewicz, University of Bialystok, Poland
150. Ute Röhrig, Swiss Institute of Bioinformatics, Switzerland
151. Victor Rojas, Parc Científic de Barcelona, Spain
152. Mariana Rossi, Fritz-Haber-Institut der MPG, Berlin, Germany
153. Antonio Sanchez Torralba, Spanish Nat. Cancer Res. Center (CNIO), Spain
154. Alfonso Sanmartin Pensado, University of Leipzig, Germany
155. Hiroko Satoh, National Institute of Informatics, Japan

156. Daniel Schaerf, Uni Mainz, Germany
157. Christoph Schiffmann, FU Berlin, Germany
158. Celina Sikorska, University of Gdansk, Poland
159. Artur Smaga, University of Warsaw, Poland
160. Xavier Solans-Monfort, Universitat Autònoma de Barcelona, Spain
161. Holger Somnitz, University of Duisburg-Essen, Germany
162. Bernardo Sosa Padilla Araujo, California Institute of Technology, USA
163. Vladimir Stegailov, Russian Academy of Sciences, Russia
164. Jian Sun, Ruhr-Universität Bochum, Germany
165. Kateryna Sykina, CNRS, France
166. Ravi Tripathi, Indian Institute of Technology Kanpur, India
167. Christian Tuma, IBM Zurich, Switzerland
168. Gregori Ujaque, Universitat Autònoma de Barcelona, Spain
169. Atsushi Urakawa, Institut Catala d'Investigacio Quimica (ICIQ), Spain
170. José Luis Vallés Pardo, Universiteit Leiden, Netherlands
171. Omar Valsson, University of Twente, Netherlands
172. Daniele Varsano, University of Rome, Italy
173. Swati Vartak, Simon Fraser University, Canada
174. Linas Vilciauskas, Max-Planck-Institut für Festkörperforschung, Germany
175. Iva Voleska, University of Pardubice, Czech Republic
176. Łukasz Walewski, University of Warsaw, Poland
177. Katharina Wendler, Max Planck Institute for Polymer Research, Poland
178. Andrea Zen, University of Rome, Italy
179. Changjun Zhang, UCL, London, UK
180. Amin Reza Zolghadr, Shiraz University, Iran

3 General Job Announcements

Faculty Position in Condensed Matter Theory

Department of Physics and Engineering Physics, College of Arts & Science

University of Saskatchewan, Canada

The Department of Physics and Engineering Physics, College of Arts & Science at the University of Saskatchewan and the Canadian Light Source invite applications for a tenure-track faculty position in the area of Condensed Matter Theory. Applications or nominations are encouraged from individuals with expertise and research accomplishments in one or more of the following areas: Electronic Structure Theory, Photon-Matter Interactions and Optical Properties of Materials, Quantum Transport in Materials and Nanostructures, X-ray Absorption and Scattering.

The University of Saskatchewan is home to the Canadian Light Source (CLS,

`http://www.lightsource.ca`)

synchrotron and a leading national center for research with synchrotron light. Candidates must hold a doctoral degree in a relevant discipline. Postdoctoral experience will be an asset. The successful candidate will have an excellent research record in the Theoretical Physics of Condensed Matter, and the potential to provide vision, leadership and theoretical guidance for research involving the Canadian Light Source. The Innovation Place Research Park and the twelve University Colleges provide further exciting opportunities for collaborative research.

The successful candidate will be appointed to a tenure-track faculty position in the Department of Physics and Engineering Physics. The candidate will be expected to establish an internationally leading research program, secure externally funded research, work collaboratively with the CLS experimental groups, supervise postdoctoral fellows and graduate students, and participate in graduate and undergraduate level teaching.

Located in the beautiful 'river city' of Saskatoon in Canada's high-growth province, the University of Saskatchewan and the College of Arts and Science are poised for unprecedented growth and transformation. Commitments to the growth of the graduate student and post-doctoral population are embedded in our Strategic Plan. The University forms a dynamic partnership of scholars dedicated to challenging old notions and creating new ideas to share with our students. We offer a thriving intellectual climate and countless opportunities for partnerships and collaboration in the heart of one of the world's most charming campuses. To learn more about the College of Arts and Science and the Department of Physics and Engineering Physics, visit

`http://artsandscience.usask.ca`

and

`http://artsandscience.usask.ca/physics`.

We anticipate that the position will be offered at assistant professor level. However, highly qualified and experienced candidates may be considered for an appointment at associate or full professor level. Interested candidates should submit curriculum vitae, a research plan, a teaching dossier and the name, mailing address, email address and phone number of at least three references to:

Attn: Marj Granrude
Condensed Matter Theory Search Committee
Department of Physics and Engineering Physics
University of Saskatchewan
116 Science Place, Saskatoon, SK, S7N 5E2, Canada
Email: marj.granrude@usask.ca

Review of applications began on July 1, 2011 and will continue until the position is filled. The starting date is anticipated to be January 1, 2012.

The University is committed to Employment Equity. Members of Designated Groups (women, Aboriginal people, people with disabilities and visible minorities) are encouraged to self-identify on their applications. All qualified candidates are encouraged to apply; however, Canadians and permanent residents will be given priority.

Post-doctoral Research Position (up to 3 years) in Computational Nanoscience

Nanoscience Center (NSC), University of Jyväskylä, Finland

Project: Metal nanoclusters for fluorescence, catalysis, and heavy metal scavenging

The goal of this project is to develop novel functionalities and applications for metal nanoclusters that are stabilized by functional organic ligands. Potential applications include biolabeling, sensing, imaging, nanocatalysis and scavenging of harmful heavy metals from Nature. The project involves collaboration with two experimental groups, one in Finland (Dr. R. Ras, Aalto University) and one in India (prof. T. Pradeep, IIT Madras / Chennai). The position is available in January 2012 and can be extended up to the end of 2014.

An ideal candidate for this position has a doctorate degree in chemical physics/physical chemistry/theoretical chemistry and practical experience in computations using time-dependent density functional theory and excited- state dynamics. Programming skills (C/Python/Fortran) are considered as bonus. Interested applicants should send their CV, list of publications, a short motivation letter and contact information of three (3) references to prof. Hannu Häkkinen by email (hannu.hakkinen@phys.jyu.fi).

Screening of the applicants starts December 10, 2011 and will continue until the position is filled.

For information about the NSC, see www.jyu.fi/nanoscience.

Contact: Prof. Hannu Häkkinen, hannu.hakkinen@phys.jyu.fi, cell: +358 400 247 973.

4 Abstracts

Calculating optical absorption spectra for large systems using linear-scaling density functional theory

Laura E. Ratcliff, Nicholas D. M. Hine and Peter D. Haynes
Department of Materials, Imperial College London, UK

Abstract

A new method for calculating optical absorption spectra within linear-scaling density functional theory (LS-DFT) is presented, incorporating a scheme for optimizing a set of localized orbitals to accurately represent unoccupied Kohn-Sham states. Three different schemes are compared and the most promising of these, based on the use of a projection operator, has been implemented in a fully functional LS-DFT code. The method has been applied to the calculation of optical absorption spectra for the metal-free phthalocyanine molecule and the conjugated polymer poly(para-phenylene). Excellent agreement with results from a traditional DFT code is obtained.

(Phys. Rev. B 84, 165131 (2011))
Contact person: Laura Ratcliff, laura.ratcliff08@imperial.ac.uk

System-size convergence of point defect properties: The case of the silicon vacancy

F. Corsetti and A. A. Mostofi
Thomas Young Centre, Imperial College London, London SW7 2AZ, United Kingdom

Abstract

We present a comprehensive study of the vacancy in bulk silicon in all its charge states from 2+ to 2−, using a supercell approach within plane-wave density-functional theory, and systematically quantify the various contributions to the well-known finite size errors associated with calculating formation energies and stable charge state transition levels of isolated defects with periodic boundary conditions. Furthermore, we find that transition levels converge faster with respect to supercell size when only the Γ-point is sampled in the Brillouin zone, as opposed to a dense k-point sampling. This arises from the fact that defect level at the Γ-point quickly converges to a fixed value which correctly describes the bonding at the defect center. Our calculated transition levels with 1000-atom supercells and Γ-point only sampling are in good agreement with available experimental results. We also demonstrate two simple and accurate approaches for calculating the valence band offsets that are required for computing formation energies of charged defects, one based on a potential averaging scheme and the other using maximally-localized Wannier functions (MLWFs). Finally, we show that MLWFs provide a clear description of the nature of the electronic bonding at the defect center that verifies the canonical Watkins model.

(Phys. Rev. B **84**, 035209 (2011))
Contact person: Fabiano Corsetti, fabiano.corsetti08@imperial.ac.uk

Orbital control in strained ultra-thin $LaNiO_3/LaAlO_3$ superlattices

J. W. Freeland[1], Jian Liu[2], M. Kareev[2], B. Gray[2], J. W. Kim[1], P. Ryan[1], R. Pentcheva[3] and J. Chakhalian[2]

[2] *Advanced Photon Source, Argonne National Laboratory - Argonne, IL 60439, USA*

[2] *Department of Physics, University of Arkansas - Fayetteville, AR 72701, USA*

[3] *Department of Earth and Environmental Sciences, Section Crystallography and Center of Nanoscience, University of Munich, Theresienstrasse 41, D-80333 Munich, Germany*

Abstract

In pursuit of rational control of orbital polarization, we present a combined experimental and theoretical study of single-unit-cell superlattices of the correlated metal $LaNiO_3$ and the band insulator $LaAlO_3$. Polarized X-ray absorption spectra show a distinct asymmetry in the orbital response under strain. A splitting of orbital energies consistent with octahedral distortions is found for the case of compressive strain. In sharp contrast, for tensile strain, no splitting is found although a strong orbital polarization is present. Density functional theory calculations including a Hubbard U-term reveal that this asymmetry is a result of the interplay of strain and confinement that induces octahedral rotations and distortions and altered covalency in the bonding across the interfacial Ni-O-Al apical oxygen, leading to a charge disproportionation at the Ni sites for tensile strain.

(Published in EPL, 96 (2011) 57004)

Contact person: Rossitza.Pentcheva@lrz.uni-muenchen.de, freeland@anl.gov

Confinement induced metal-to-insulator transition in strained $LaNiO_3/LaAlO_3$ superlattices

Ariadna Blanca-Romero and Rossitza Pentcheva
Department of Earth and Environmental Sciences,
Section Crystallography and Center of Nanoscience,
University of Munich, Theresienstrasse 41, D-80333 Munich, Germany

Abstract

Using density functional theory calculations including a Hubbard U term we explore the effect of strain and confinement on the electronic ground state of superlattices containing the band insulator $LaAlO_3$ and the correlated metal $LaNiO_3$. Besides a suppression of holes at the apical oxygen, a central feature is the asymmetric response to strain in single unit cell superlattices: For tensile strain a band gap opens due to charge disproportionation at the Ni sites with two distinct magnetic moments of $1.45\mu_B$ and $0.71\mu_B$. Under compressive stain, charge disproportionation is nearly quenched and the band gap collapses due to overlap of $d_{3z^2-r^2}$ bands through a semimetallic state. This asymmetry in the electronic behavior is associated with the difference in octahedral distortions and rotations under tensile and compressive strain. The ligand hole density and the metallic state are quickly restored with increasing thickness of the $(LaAlO_3)_n/(LaNiO_3)_n$ superlattice from $n = 1$ to $n = 3$

(Published in Phys. Rev. B 84, 195450 (2011))
Contact persons: Rossitza.Pentcheva@lrz.uni-muenchen.de,
blanca_romero@lrz.uni-muenchen.de

Reduced effective spin-orbital degeneracy and spin-orbital ordering in paramagnetic transition metal oxides: Sr_2IrO_4 vs. Sr_2RhO_4

Cyril Martins,[1,2] Markus Aichhorn,[1,3] Loïg Vaugier,[1] Silke Biermann[1,2]
[1] *Centre de Physique Théorique, Ecole Polytechnique, CNRS, 91128 Palaiseau Cedex, France*
[2] *Japan Science and Technology Agency, CREST, Kawaguchi 332-0012, Japan*
[3] *Institute of Theoretical and Computational Physics, TU Graz, Petersgasse 16, Graz, Austria*

Abstract

We discuss the notions of spin-orbital polarization and ordering in paramagnetic materials, and address their consequences in transition metal oxides. Extending the combined density functional and dynamical mean field theory scheme to the case of materials with large spin-orbit interactions, we investigate the electronic excitations of the paramagnetic phases of Sr_2IrO_4 and Sr_2RhO_4. We show that the interplay of spin-orbit interactions, structural distortions and Coulomb interactions suppresses spin-orbital fluctuations. As a result, the room temperature phase of Sr_2IrO_4 is a paramagnetic spin-orbitally ordered Mott insulator. In Sr_2RhO_4, the effective spin-orbital degeneracy is reduced, but the material remains metallic, due to both, smaller spin-orbit and smaller Coulomb interactions. We find excellent agreement of our *ab-initio* calculations for Sr_2RhO_4 with angle-resolved photoemission, and make predictions for spectra of the paramagnetic phase of Sr_2IrO_4.

(Accepted by Physicsal Review Letters; available electronically as arXiv:1107.1371)
Contact person: Cyril Martins (cyril.martins@cpht.polytechnique.fr)

Optical absorption in degenerately doped semiconductors: Mott transition or Mahan excitons?

André Schleife[1,2,3], Claudia Rödl[1,2], Frank Fuchs[1,2], Karsten Hannewald[1,2], and Friedhelm Bechstedt[1,2]

[1] *Institut für Festkörpertheorie und -optik, Friedrich-Schiller-Universität, Max-Wien-Platz 1, 07743 Jena, Germany*

[2] *European Theoretical Spectroscopy Facility (ETSF)*

[3] *Condensed Matter and Materials Division, Lawrence Livermore National Laboratory, Livermore, CA 94550, USA*

Abstract

Electron doping turns semiconductors conductive even when they have wide fundamental band gaps. The degenerate electron gas in the lowest conduction-band states, e.g. of a transparent conducting oxide, drastically modifies the Coulomb interaction between the electrons and, hence, the optical properties close to the absorption edge. We describe these effects by developing an *ab-initio* technique which captures also the Pauli blocking and the Fermi-edge singularity at the optical absorption onset, that occur in addition to quasiparticle and excitonic effects. We answer the question whether free carriers induce an excitonic Mott transition or trigger the evolution of Wannier-Mott excitons into Mahan excitons. The prototypical n-type zinc oxide is studied as an example.

(Phys. Rev. Lett., in press (2011).)

Contact person: André Schleife (a.schleife@llnl.gov)

Activation Energies for Diffusion of Defects in Silicon: The Role of the Exchange-Correlation Functional

Stefan K. Estreicher[1], Daniel J. Backlund[1],
Christian Carbogno[2], and Matthias Scheffler[2]
[1] *Texas Tech University, Lubbock, Texas 79409-1051, USA*
[2] *Fritz-Haber-Institut der Max-Planck-Gesellschaft,*
Faradayweg 4–6, 14195 Berlin, Germany

Abstract

DFT calculations were used to determine the activation energies (E_a values) for the diffusion of defects such as O atoms (O_i^0 red sphere in the picture) in silicon (blue spheres). The migration paths were obtained from the nudged elastic band method. The activation energies calculated with four exchange-correlation functionals (E_{xc}) were compared to experimental data. The E_a values of "atomic-like" interstitials are mostly independent of E_{xc}, but those of strongly bound impurities are sensitive to the choice of E_{xc}.

(Angew. Chem. Int. Ed., 50, 1-6 (2011))
Contact person: Christian Carbogno (carbogno@fhi-berlin.mpg.de)

Time-dependent density-functional and reduced density-matrix methods for few electrons: Exact versus adiabatic approximations

N. Helbig,[1,5] J.I. Fuks,[1,5] I.V. Tokatly,[1,2,5] H. Appel,[3,5]
E.K.U. Gross,[4,5] and A. Rubio[1,3,5]
[1] *Universidad del País Vasco,*
Av. Tolosa 72, E-20018 San Sebastián, Spain
[2] *IKERBASQUE, Basque Foundation for Science,*
E-48011 Bilbao, Spain
[3] *Fritz-Haber-Institut der Max-Planck-Gesellschaft,*
Faradayweg 4–6, 14195 Berlin, Germany
[4] *Max-Planck-Institut für Mikrostrukturphysik,*
Weinberg 2, D-06120 Halle, Germany
[5] *European Theoretical Spectroscopy Facility*

Abstract

To address the impact of electron correlations in the linear and non-linear response regimes of interacting many-electron systems exposed to time-dependent external fields, we study one-dimensional (1D) systems where the interacting problem is solved exactly by exploiting the mapping of the 1D N-electron problem onto an N-dimensional single electron problem. We analyze the performance of the recently derived 1D local density approximation as well as the exact-exchange orbital functional for those systems. We show that the interaction with an external resonant laser fields shows Rabi oscillations which are detuned due to the lack of memory in adiabatic approximations. To investigate situations where static correlations play a role, we consider the time-evolution of the natural occupation numbers associated to the reduced one-body density matrix. Those studies shed light on the non-locality and time-dependence of the exchange and correlation functionals in time-dependent density and density-matrix functional theories.

(Chem. Phys., in print (2011))
Contact person: Heiko Appel (appel@fhi-berlin.mpg.de)

Assessment of correlation energies based on the random-phase approximation

Joachim Paier,[1] Xinguo Ren,[2,3] Patrick Rinke,[2,3] Gustavo E. Scuseria,[4,5]
Andreas Grüneis,[6] Georg Kresse,[6] and Matthias Scheffler[2,3]
[1]*Institut für Chemie, Humboldt-Universität zu Berlin,*
Unter den Linden 6, 10099 Berlin, Germany
[2]*Fritz-Haber-Institut der Max-Planck-Gesellschaft,*
Faradayweg 4–6, 14195 Berlin, Germany
[3]*European Theoretical Spectroscopy Facility*
[4]*Department of Chemistry, Rice University,*
Houston, Texas 77005, USA
[5]*Department of Physics and Astronomy, Rice University,*
Houston, Texas 77005, USA
[6]*Faculty of Physics and Center for Computational Materials Science,*
Universität Wien, Sensengasse 8/12, A-1090 Wien, Austria

Abstract

The random-phase approximation to the ground state correlation energy (RPA) in combination with exact exchange (EX) has brought Kohn-Sham (KS) density functional theory one step closer towards a universal, "general purpose first principles method". In an effort to systematically assess the influence of several correlation energy contributions beyond RPA, this work presents dissociation energies of small molecules and solids, activation energies for hydrogen transfer and non-hydrogen transfer reactions, as well as reaction energies for a number of common test sets. We benchmark EX+RPA and several flavors of energy functionals going beyond it: second-order screened exchange (SOSEX), single excitation (SE) corrections, renormalized single excitation (rSE) corrections, as well as their combinations. Both the single excitation correction as well as the SOSEX contribution to the correlation energy significantly improve upon the notorious tendency of EX+RPA to underbind. Surprisingly, activation energies obtained using EX+RPA based on a KS reference alone are remarkably accurate. RPA+SOSEX+rSE provides an equal level of accuracy for reaction as well as activation energies and overall gives the most balanced performance, which makes it applicable to a wide range of systems and chemical reactions.

(Submitted to New J. Phys. (2011))
Contact person: Patrick Rinke (rinke@fhi-berlin.mpg.de)

New perspective on formation energies and energy levels of point defects in non-metals

Rampi Ramprasad,[1] Hong Zhu,[1] Patrick Rinke,[2] and Matthias Scheffler[2]
[1] *Chemical, Materials and Biomolecular Engineering and Institute of Materials Science, University of Connecticut, 97 North Eagleville Road, Storrs, CT 06269, USA*
[2] *Fritz-Haber-Institut der Max-Planck-Gesellschaft, Faradayweg 4–6, 14195 Berlin, Germany*

Abstract

We propose a powerful scheme to accurately determine the formation energy and thermodynamic charge transition levels of point defects in non-metals. Previously unknown correlations between defect properties and the valence-band width of the defect-free host material are identified allowing for a determination of the former via an accurate knowledge of the latter. These correlations are identified through a series of hybrid density functional theory computations and an *unbiased* exploration of the parameter space that defines the Hyde-Scuseria-Ernzerhof family of hybrid-functionals. The applicability of this paradigm is demonstrated for point defects in Si, Ge and ZrO_2.

(Submitted to Phys. Rev. Lett. (2011))
Contact person: Patrick Rinke (rinke@fhi-berlin.mpg.de)

Density-functional theory with screened van der Waals interactions for the modeling of hybrid inorganic/organic systems

Victor G. Ruiz,[1] Wei Liu,[1] Egbert Zojer,[2]
Matthias Scheffler,[1] and Alexandre Tkatchenko[1]
[1]*Fritz-Haber-Institut der Max-Planck-Gesellschaft, Faradayweg 4–6, 14195 Berlin, Germany*
[2]*Institute of Solid State Physics, Graz University of Technology, Petersgasse 16, A-8010 Graz, Austria*

Abstract

The electronic properties and the function of hybrid inorganic/organic systems (HIOS) are intimately linked to their interface geometry. Here we show that the inclusion of the many-body collective response of the substrate electrons inside the inorganic bulk enables us to reliably predict the HIOS geometries and energies. This is achieved by the combination of dispersion-corrected density-functional theory (the DFT+vdW approach) [*Phys. Rev. Lett.* **102**, 073005 (2009)], with the Lifshitz-Zaremba-Kohn theory for the non-local Coulomb screening within the bulk. Our method yields geometries in remarkable agreement (≈ 0.1 Å) with normal incidence x-ray standing wave measurements for the 3,4,9,10-perylene-tetracarboxylic acid dianhydride ($C_{24}H_6O_8$, PTCDA) molecule on Cu(111), Ag(111), and Au(111) surfaces. Similarly accurate results are obtained for xenon and benzene adsorbed on metal surfaces.

(Submitted to Phys. Rev. Lett. (2011))
Contact person: Alexandre Tkatchenko (tkatchenko@fhi-berlin.mpg.de)

Calculating dispersion interactions using maximally localized Wannier functions

Lampros Andrinopoulos, Nicholas D. M. Hine, Arash A. Mostofi
The Thomas Young Centre for Theory and Simulation of Materials,
Imperial College London,
London SW7 2AZ, United Kingdom

Abstract

We investigate a recently developed approach [P. L. Silvestrelli, Phys. Rev. Lett. **100**, 053002 (2008); J. Phys. Chem. A **113**, 5224 (2009)] that uses maximally localized Wannier functions to evaluate the van der Waals contribution to the total energy of a system calculated with density-functional theory. We test it on a set of atomic and molecular dimers of increasing complexity (argon, methane, ethene, benzene, phthalocyanine, and copper phthalocyanine) and demonstrate that the method, as originally proposed, has a number of shortcomings that hamper its predictive power. In order to overcome these problems, we have developed and implemented a number of improvements to the method and show that these modifications give rise to calculated binding energies and equilibrium geometries that are in closer agreement to results of quantum-chemical coupled-cluster calculations.

(J. Chem. Phys. **135**, 154105 (2011))
Contact person: l.andrinopoulos09@imperial.ac.uk

Visualization of Hydrogen-bonding and Associated Chirality in Methanol Hexamers

Timothy J. Lawtoni[1], Javier Carrasco[2], Ashleigh E. Baber[1],
Angelos Michaelides[3] and E. Charles H. Sykes[1]
[1]*Department of Chemistry, Tufts University, Medford, MA 02155-5813, USA*
[2]*Instituto de Catálisis y Petroleoquímica, CSIC,*
Marie Curie 2, E-28049 Madrid, Spain
[3]*London Centre for Nanotechnology and Department of Chemistry,*
University College London, London WC1E 6BT, United Kingdom

Abstract

Using a combination of scanning tunneling microscopy (STM) and density functional theory the hydrogen bond directionality and associated chirality of enantiopure clusters is visualized and controlled. This is demonstrated with methanol hexamers adsorbed on Au(111), which depending on their chirality, adopt two distinct molecular footprints on the surface. Controlled STM tip manipulations were used to interconvert the chirality of entire clusters and to break up metastable chain structures into hexamers.

(Phys. Rev. Lett., in press)
Contact person: angelos.michaelides@ucl.ac.uk

The Energy of Hydroxyl Coadsorbed with Water on Pt(111)

Wanda Lew[1], Matthew C. Crowe[1], Charles T. Campbell[1], Javier Carrasco[2,3,4], Angelos Michaelides[2]

[1]*Department of Chemistry, University of Washington, Seattle, WA 98195-1700, USA*

[2]*London Centre for Nanotechnology and Department of Chemistry, University College London, London WC1E 6BT, UK*

[3]*Fritz-Haber-Institut der Max-Planck-Gesellschaft, Faradayweg 4-6, 14195 Berlin, Germany*

[4]*Instituto de Catálisis y Petroleoquímica, CSIC, Marie Curie 2, E-28049 Madrid, Spain*

Abstract

Adsorbed OH is a key intermediate in many catalytic reactions and a common species on many materials' surfaces. We report here measurements of the calorimetric heats for forming the widely-studied and structurally well-defined coadsorbed ($H_2O\cdots OH$) complex on Pt(111) from water vapor and adsorbed oxygen adatoms. We further use these heats as benchmarks to evaluate the performance of density functional theory (DFT), modified to include van der Waals interactions and zero point energies, and find agreement to within 1 and 15 kJ/mol for the two adlayer structures studied.

(Journal of Physical Chemistry C, in press)

Contact person: angelos.michaelides@ucl.ac.uk

Acetone adsorption on ice investigated by X-ray spectroscopy and density functional theory

D. E. Starr[a], D. Pan[b], J. T. Newberg[a], M. Ammann[c], E. G. Wang[d], A. Michaelides[e] and H. Bluhm[a]

[a] *Chemical Sciences Division, Lawrence Berkeley National Laboratory, Berkeley, CA 94720, USA*

[b] *Institute of Physics, Chinese Academy of Sciences, P.O. Box 603, Beijing 100190, P. R. China*

[c] *Paul Scherrer Institut, Labor fur Radio-und Umweltchemie, 5232 Villigen, Switzerland*

[d] *School of Physics, Peking University, Beijing 100871, P. R. China*

[e] *London Centre for Nanotechnology and Department of Chemistry, University College London, London, WC1H 0AJ, UK*

Abstract

Using a combination of X-ray photoemission and near-edge X-ray absorption spectroscopy (NEXAFS) as well as density-functional theory (DFT), we have investigated the adsorption of acetone on ice in the temperature range from 218 to 245 K. The adsorption enthalpy determined from experiment (45 kJ mol^{-1}) agrees well with the adsorption energy predicted by theory (41 to 44 kJ mol^{-1}). Oxygen K-edge NEXAFS spectra indicate that the presence of acetone at the ice surface does not induce the formation of a pre-melted layer at temperatures up to 243 K. DFT calculations show that the energetically most favored adsorption geometry for acetone on ice is with the molecular plane almost parallel to the surface.

(Published on Phys. Chem. Chem. Phys., 2011, 13, 19988–19996)

Contact person: angelos.michaelides@ucl.ac.uk

Water-hydroxyl phases on an open metal surface: breaking the ice rules

Matthew Forster[a], Rasmita Raval[a], Javier Carrasco[b],
Angelos Michaelides[c] and Andrew Hodgson[a]
[a] *Surface Science Research Centre and Department of Chemistry, University of Liverpool, Oxford Street, Liverpool, UK L69 3BX*
[b] *Instituto de Catálisis y Petroleoquímica, CSIC, Marie Curie 2, E-28049, Madrid, Spain*
[c] *London Centre for Nanotechnology and Department of Chemistry, University College London, London, UK WC1E 6BT*

Abstract

Hydroxyl is a key reaction intermediate in many surface catalyzed redox reactions, yet establishing the phase diagram for water/hydroxyl adsorption on metal surfaces remains a considerable challenge for interfacial chemistry. While the structures formed on close packed metal surfaces have been discussed widely, the phase diagram on more reactive, open metal surfaces, is complex and the H-bonding structures are largely unknown. Based on scanning tunnelling microscopy and density functional theory calculations, we report the phase diagram for water/hydroxyl on Cu(110), providing a complete molecular description of the complex hydrogen bonding structures formed. Three distinct phases are observed as the temperature is decreased and the water/hydroxyl ratio increased: pure OH dimers, extended $1H_2O$:1OH chains, aligned along the close-packed Cu rows, and finally a distorted 2D hexagonal c(2×2) $2H_2O$:1OH network. None of these phases obey the conventional 'ice rules', instead their structures can be understood based on weak H donation by hydroxyl, which favours H-bonding structures dominated by water donation to hydroxyl, and competition between hydroxyl adsorption sites. Hydroxyl binds in the Cu bridge site in the 1D chain structures, but is displaced to the atop site in the 2D network in order to accommodate water in its preferred atop binding geometry. The adsorption site and stability of hydroxyl can therefore be tuned simply by changing the surface temperature and water content, giving a new insight as to how the open metal template influences the water/hydroxyl structures formed and the activity of hydroxyl.

(Chemical Science, in press)
Contact person: angelos.michaelides@ucl.ac.uk

Proton ordering in cubic ice and hexagonal ice; a potential new ice phase-XIc

Zamaan Raza[a], Dario Alfè[b], Christoph G. Salzmann[c], Jiří Kliměs[a,d], Angelos Michaelides[a,d] and Ben Slater[a]

[a] *Department of Chemistry, University College London, 20 Gordon Street, London WC1H 0AJ*

[b] *Department of Earth Sciences, University College London, Gower Street, London WC1E 6BT*

[c] *Department of Chemistry, Durham University, South Road, Durham DH1 3LE*

[d] *London Centre for Nanotechnology, 17-19 Gordon Street, London WC1H 0AH*

Abstract

Ordinary water ice forms under ambient conditions and has two polytypes, hexagonal ice (Ih) and cubic ice (Ic). From a careful comparison of proton ordering arrangements in Ih and Ic using periodic density functional theory (DFT) and diffusion monte carlo (DMC) approaches, we find that the most stable arrangement of water molecules in cubic ice is isoenergetic with that of the proton ordered form of hexagonal ice (known as ice XI). We denote this potential new polytype of ice XI as XIc and discuss a possible route for preparing XIc.

(Phys. Chem. Chem. Phys., in press)

Contact person: b.slater@ucl.ac.uk

5 Presenting New Initiatives

OPENING OF THE ICTP SOUTH AMERICAN INSTITUTE FOR FUNDAMENTAL RESEARCH

The ICTP South American Institute for Fundamental Research is a new South American regional center for theoretical physics created in a collaboration of the International Centre for Theoretical Physics (ICTP) with the State University of Sao Paulo (UNESP) and the Sao Paulo Research Funding Agency (FAPESP). Activities will begin in 2012 with international schools and workshops, and the center will have an active visiting program together with several postdoctoral and permanent research professor positions. The new South American center will be located on the campus of the Instituto de Fisica Teorica (IFT-UNESP) in the city of Sao Paulo. Applications are now open for postdoctoral and permanent research professor positions, as well as for scientific visits, proposals of 2013 activities, and participation in 2012 schools.

More information and online application forms are available on the webpage

`http://www.ictp-saifr.org`.

A job advertisement for the permanent and postdoctoral positions can be downloaded from the link

`http://www.ictp-saifr.org/positionsictpsaifr.pdf`,

and we would be very grateful if you could post a printed copy of this job advertisement at your institution.

Any questions may be directed to secretary@ictp-saifr.org .

Nathan Berkovits (acting director of ICTP-SAIFR)

6 SCIENTIFIC HIGHLIGHT OF THE MONTH

Hybrid functionals and *GW* approximation in the FLAPW method

Christoph Friedrich, Markus Betzinger, Martin Schlipf, and Stefan Blügel

Peter Grünberg Institut and Institute for Advanced Simulation, Forschungszentrum Jülich and JARA, 52425 Jülich, Germany

Arno Schindlmayr

Department Physik, Universität Paderborn, 33095 Paderborn, Germany

Abstract

We present recent advances in numerical implementations of hybrid functionals and the *GW* approximation within the full-potential linearized augmented-plane-wave (FLAPW) method. The former is an approximation for the exchange-correlation contribution to the total energy functional in density-functional theory, and the latter is an approximation for the electronic self-energy in the framework of many-body perturbation theory. All implementations employ the mixed product basis, which has evolved into a versatile basis for the products of wave functions, describing the incoming and outgoing states of an electron that is scattered by interacting with another electron. It can thus be used for representing the non-local potential in hybrid functionals as well as the screened interaction and related quantities in *GW* calculations. In particular, the six-dimensional space integrals of the Hamiltonian exchange matrix elements (and exchange self-energy) decompose into sums over vector-matrix-vector products, which can be evaluated easily. The correlation part of the *GW* self-energy, which contains a time or frequency dependence, is calculated on the imaginary frequency axis with a subsequent analytic continuation to the real axis or, alternatively, by a direct frequency convolution of the Green function G and the dynamically screened Coulomb interaction W along a contour integration path that avoids the poles of the Green function. Hybrid-functional and *GW* calculations are notoriously computationally expensive. We present a number of tricks that reduce the computational cost considerably including the usage of spatial and time-reversal symmetries, modifications of the mixed product basis with the aim to optimize it for the correlation self-energy and another modification that makes the Coulomb matrix sparse, analytic expansions of the interaction potentials around the point of divergence at $\mathbf{k} = \mathbf{0}$, and a nested density and density-matrix convergence scheme for hybrid-functional calculations. We show CPU timings for prototype semiconductors and illustrative results for GdN and ZnO.

1 Introduction

Within the last decades density-functional theory (DFT) [1, 2] has evolved into a powerful tool for calculating the electronic ground-state properties of molecules and solids. It is usually applied within the Kohn-Sham (KS) formalism [3], in which the interacting many-electron system is mapped onto a system of fictitious noninteracting particles that, by construction, possesses the same particle density as that of the real system. All exchange and correlations effects of the many-electron system are incorporated into the so-called exchange-correlation (xc) energy functional, which is not known exactly and must be approximated in practice. The choice of the xc functional is the only practical approximation in this otherwise exact theory and determines the precision and efficiency of the numerical DFT calculations.

Fortunately, already simple approximations, such as the local-density (LDA) [4, 5] and generalized gradient approximation (GGA) [6, 7], give reliable results for a wide range of materials and properties. In these approximations the exchange-correlation energy density is given as a function of the local electron density (and density gradient in the case of the GGA) rather than as a functional, which enables a straightforward numerical implementation. However, the missing nonlocal dependence on the density leads to several shortcomings. First, the electrostatic interaction of the electron with the total electron charge, described by the Hartree potential, contains an unphysical interaction of the electron with itself, commonly referred to as self-interaction. This extra term should be compensated exactly by an identical term with opposite sign in the exchange potential, in the same manner as in Hartree-Fock theory. However, as the LDA and GGA exchange potentials are only approximate, this cancellation is incomplete and part of the self-interaction remains. This error leads, in particular, to an improper description of localized states, which appear too high in energy and tend to delocalize. This deficiency is particularly critical in systems whose electronic and magnetic properties are largely governed by the correlated motion of electrons in localized states. The rare-earth chalcogenides are among this class of materials, having incompletely filled f-electron shells. We will show results for one such material, GdN, below. Second, the LDA and GGA functionals do not give rise to a discontinuity of the xc potential with respect to changes in the particle number. Theoretically, the sum of the KS band gap and the discontinuity yields the real band gap [8, 9]. The KS band gap alone is known to underestimate experimental gaps by as much as 50%. This is often called the band-gap problem of LDA and GGA. Finally, the LDA and GGA functionals do not exhibit the correct asymptotic behavior of exchange and correlation effects between interacting but spatially separate parts of an electronic system.

During the last decade hybrid functionals, which combine a local or semi-local xc functional with nonlocal Hartree-Fock (HF) exchange, have been shown to overcome these deficiencies to a great extent [10, 11, 12, 13, 14]. Hybrid functionals are usually applied within the generalized Kohn-Sham (gKS) scheme [15], where the HF exchange term leads to a nonlocal exchange potential in the one-particle equations. The first hybrid functional, a half-and-half mixing of the LDA functional with HF exchange, was proposed by Becke in 1993 [16]. Since then various *ab initio* and semi-empirical hybrid functionals have been published [17, 10, 18, 19]. The hybrid functionals, on which we focus in this article, do not contain any empirical parameters and are thus *ab initio* hybrid functionals.

The presence of the nonlocal exchange potential requires the description of the scattering of two particles interacting with each other via the Coulomb interaction. This involves to treat the incoming and outgoing states of the two particles explicitly, which will lead us to introduce a special basis for the product of wave functions. Once such a basis formulation of the electron-electron interaction is found, the question arises whether one can take a wider perspective beyond the HF exchange term and build up a numerical framework for many-body perturbation theory [20]. We will see that this is, indeed, possible. In many-body perturbation theory, one starts with a noninteracting system and incorporates the electron-electron interaction by adiabatically switching on the interaction. In the limit of full interaction strength, one finds that physical quantities can be written systematically as summations over integrals – the so-called Feynman diagrams – that contain increasingly higher orders of the electron-electron interaction. In this way, one can in principle construct the electronic self-energy in a systematic way. The self-energy incorporates all many-body exchange and correlation effects and is, in this sense, the counterpart of the xc functional of DFT. A very successful approximation of the self-energy is given by the *GW* approximation [21], which contains the electronic exchange exactly while the screening is treated at the level of the random-phase approximation, where noninteracting electron-hole ring diagrams are summed to all orders. The *GW* approximation is mainly used to compute electronic excitation energies and lifetimes from first principles so that it complements DFT, which is in practice restricted to the electronic ground state.

Due to the complexity of hybrid-functional and *GW* calculations, most implementations [22, 23, 24] have been based on the pseudopotential plane-wave approach, which effectively restricts the range of materials that can be examined. In particular, materials containing transition metals and rare earths as well as oxides cannot be treated efficiently in this approach. Two early all-electron calculations using the *GW* approximation were carried out by Hamada *et al.* [25] for Si and by Aryasetiawan [26] for Ni, both within the LAPW method. However, only very recently were further all-electron implementations reported, based on the FLAPW [27, 28], the linearized muffin-tin orbital (LMTO) [29, 30, 31], the projector-augmented-wave (PAW) [32, 33, 34], and the Korringa-Kohn-Rostoker method [35] together with applications to a larger variety of systems. Apart from an early implementation within a Gaussian-type basis [36], the hybrid functionals were adopted to all-electron methods only in recent years. In 2005 Paier *et al.* [37] developed an implementation within the projector-augmented-wave (PAW) technique. In 2006 Novak *et al.* [38] proposed an approximate scheme within the FLAPW approach. There the nonlocal exchange term is evaluated only in individual atomic spheres and only for selected l channels. In 2010 we presented an efficient numerical implementation of hybrid functionals [39] within the FLAPW method, which is not subject to these constraints. The FLAPW method provides a highly accurate all-electron basis, with which the electron structure of a large variety of materials can be studied, including open systems with low symmetry, d- and f-electron systems as well as oxides. It treats core and valence electrons on an equal footing.

In the first Hartree-Fock implementation within the FLAPW method, Massidda *et al.* [40] employed an algorithm that is routinely used for solving the Poisson equation for the electronic and nuclear charge distribution, i.e., it generates the electrostatic potential [41]. This *Poisson solver* can also be used for the nonlocal exchange potential, because its matrix representation involves formally identical six-dimensional integrals over space. Instead of the real charge density

one then uses an artificial charge density formed by the product of two wave functions. Recently, this scheme was employed for an implementation of a Yukawa screened hybrid functional [42]. Unfortunately, although the algorithm is very fast itself, the *Poisson solver* must be called many, many times instead of just once when applied to the Hartree-Fock exchange potential, which makes this approach computationally very expensive. Furthermore, it can only be used to calculate the matrix elements of interaction potentials that possess a simple expansion in dyadic products of regular and irregular radial functions as well as spherical harmonics, e.g., the bare Coulomb and the screened Yukawa potential. The error function used in the HSE functional does not have this property. It also does not provide a framework for an implementation of the screened interaction within the random-phase approximation for the *GW* self-energy.

Here, we describe a numerical realization of hybrid functionals and the *GW* approximation within an auxiliary basis, the so-called mixed product basis, which is constructed from products of LAPW basis functions and consists of muffin-tin (MT) functions and interstitial plane waves [29]. This basis allows to describe the product formed by the incoming and outgoing states of an electron that scatters by interacting with another electron. For example, this leads mathematically to a decomposition of the state-dependent six-dimensional Hartree-Fock exchange integral into two three-dimensional and one state-independent six-dimensional integral. The latter gives rise to the Coulomb matrix represented in the mixed product basis. Thus, the matrix elements of the nonlocal exchange potential are evaluated as Brillouin-zone (BZ) sums over vector-matrix-vector products. It also allows to represent the polarization function, dielectric function, and screened interaction needed in *GW* calculations in an efficient way.

We have employed several tricks to speed up the expensive calculations of the nonlocal quantities. Among them, we employ a suitable unitary transformation, by which nearly all MT functions become multipole-free, which makes the Coulomb matrix sparse and reduces the computational effort considerably. Spatial and time-reversal symmetry is exploited to reduce the number of terms that have to be taken into account explicitly in the summations over the Brillouin zone. Symmetry can also be used to decide in advance which of the matrix elements will be nonzero and have to be calculated. Furthermore, several cutoffs, such as a band cutoff for the hybrid functionals as well as a Coulomb eigenvalue cutoff for the correlation part of the *GW* self-energy, are introduced to speed up the code. The long-range nature of the Coulomb interaction gives rise to a divergence of the Coulomb matrix at the center of the BZ leading to a divergent integrand in the exchange and correlation terms, as well as to an anisotropy of the screened interaction in the BZ center. The divergence of the Coulomb potential has to be taken into account in a numerically efficient way to obtain a favorable **k**-point convergence. Corrections beyond the divergent $1/k^2$ term obtained from $\mathbf{k}\cdot\mathbf{p}$ perturbation theory can improve the convergence further.

The article is organized as follows. Section 2 gives a brief introduction to the theory of hybrid functionals and the *GW* approximation. Our implementations are discussed in detail in Sec. 3. After some test calculations, we present results for prototype semiconductors and insulators in Sec. 4 and compare them with theoretical and experimental results from the literature. We also present illustrative results for GdN and ZnO. Section 5 gives a summary.

2 Theory

In the following, we will summarize the formulas that have to be implemented for the hybrid functionals and the *GW* approximation. Even though the underlying theories are rather different – DFT [1] and many-body perturbation theory [20] – the formulas have a similar structure, and we can use similar strategies for an implementation.

GW **approximation** We start with the *GW* approximation for the electronic self-energy [21]. The self-energy describes the renormalization of an additional particle, which can be an electron or a hole, due to the interaction with the rest of the electron system. From the renormalized Green function, information about the eigenstates of the many-electron system can be obtained, e.g., the excitation energies and lifetimes, which are measured experimentally in photoelectron spectroscopy. The *GW* approximation incorporates the renormalization due to electron exchange exactly and a large part of the renormalization due to electron correlation, where screening effects are taken into account on the level of the random-phase approximation (RPA) [43]. In a many-electron system the bare Coulomb potential $v(|\mathbf{r}-\mathbf{r}'|) = 1/|\mathbf{r}-\mathbf{r}'|$ created by an electron at $\mathbf{r}$ is screened by the redistribution of the electrons nearby.[1] In the RPA this redistribution (excluding the feed-back potential change due to this charge redistribution, which will be included later by solving a Dyson-type equation) is described by the polarization function

$$P(\mathbf{r},\mathbf{r}';\omega) = -i\sum_{\sigma}\lim_{\eta\to 0^+}\int_{-\infty}^{\infty} d\omega' G^{\sigma}(\mathbf{r},\mathbf{r}';\omega')G^{\sigma}(\mathbf{r}',\mathbf{r};\omega'-\omega)e^{i\eta\omega'}\,, \tag{1}$$

where σ is the electron spin. Diagrammatically, P is represented by a bubble formed by two Green function lines. For the non-interacting $G(\mathbf{r},\mathbf{r}';\omega)$ we employ the KS Green function, which can be written in terms of the KS wave functions $\varphi^{\sigma}_{n\mathbf{k}}(\mathbf{r})$ and energies $\epsilon^{\sigma}_{n\mathbf{k}}$ as $G^{\sigma}(\mathbf{r},\mathbf{r}';\omega) = \sum_{n\mathbf{k}}\varphi^{\sigma}_{n\mathbf{k}}(\mathbf{r})\varphi^{\sigma *}_{n\mathbf{k}}(\mathbf{r}')/[\omega-\epsilon^{\sigma}_{n\mathbf{k}}+i\eta\,\mathrm{sgn}(\epsilon^{\sigma}_{n\mathbf{k}}-\epsilon_{\mathrm{F}})]$ with the Fermi energy ϵ_{F}, where $\mathbf{k}$ and n are the Bloch vector and the band index, respectively. Inserting into Eq. (1) yields [43]

$$\begin{aligned} P(\mathbf{r},\mathbf{r}';\omega) \;=\; & \lim_{\eta\to 0^+}\sum_{\sigma}\sum_{\mathbf{q},\mathbf{k}}^{\mathrm{BZ}}\sum_{n}^{\mathrm{occ}}\sum_{n'}^{\mathrm{unocc}} \varphi^{\sigma *}_{n\mathbf{q}}(\mathbf{r})\varphi^{\sigma}_{n'\mathbf{k}}(\mathbf{r})\varphi^{\sigma}_{n\mathbf{q}}(\mathbf{r}')\varphi^{\sigma *}_{n'\mathbf{k}}(\mathbf{r}') \\ & \times\left(\frac{1}{\omega+\epsilon^{\sigma}_{n\mathbf{q}}-\epsilon^{\sigma}_{n'\mathbf{k}}+i\eta}-\frac{1}{\omega-\epsilon^{\sigma}_{n\mathbf{q}}+\epsilon^{\sigma}_{n'\mathbf{k}}-i\eta}\right). \end{aligned} \tag{2}$$

With the polarization function we obtain the dynamically screened interaction $W(\mathbf{r},\mathbf{r}';\omega)$ from the integral equation

$$\begin{aligned} W(\mathbf{r},\mathbf{r}';\omega) &= v(|\mathbf{r}-\mathbf{r}'|) \\ &\quad + \int v(|\mathbf{r}-\mathbf{r}''|)P(\mathbf{r}'',\mathbf{r}''';\omega)W(\mathbf{r}''',\mathbf{r}';\omega)\,d^3r''\,d^3r'''\,, \end{aligned} \tag{3}$$

where the implicit infinite summation of this Dyson-type equation includes the feed-back effects mentioned above.

An expansion of the electronic self-energy $\Sigma^{\sigma}_{\mathrm{xc}}(\mathbf{r},\mathbf{r}';\omega)$ in terms of W up to linear order yields the *GW* approximation

$$\Sigma^{\sigma}_{\mathrm{xc}}(\mathbf{r},\mathbf{r}';\omega) = \frac{i}{2\pi}\lim_{\eta\to 0^+}\int G^{\sigma}(\mathbf{r},\mathbf{r}';\omega+\omega')W(\mathbf{r},\mathbf{r}';\omega')e^{i\eta\omega'}\,d\omega'\,. \tag{4}$$

[1] Here and in the following we use atomic units unless noted otherwise.

If we write the screened interaction as a sum of the bare interaction and a remainder,

$$W(\mathbf{r},\mathbf{r}';\omega) = v(|\mathbf{r}-\mathbf{r}'|) + W^{\mathrm{c}}(\mathbf{r},\mathbf{r}';\omega)\,, \tag{5}$$

the self-energy [Eq. (4)] decomposes into the terms

$$\Sigma^{\sigma}_{\mathrm{x}}(\mathbf{r},\mathbf{r}') = \frac{i}{2\pi}\lim_{\eta\to 0^+}\int G^{\sigma}(\mathbf{r},\mathbf{r}';\omega+\omega')v(|\mathbf{r}-\mathbf{r}'|)e^{i\eta\omega'}d\omega' \tag{6}$$

and

$$\Sigma^{\sigma}_{\mathrm{c}}(\mathbf{r},\mathbf{r}';\omega) = \frac{i}{2\pi}\int G^{\sigma}(\mathbf{r},\mathbf{r}';\omega+\omega')W^{\mathrm{c}}(\mathbf{r},\mathbf{r}';\omega')\,d\omega'\,, \tag{7}$$

which are identified as the exchange and the correlation contributions to the electronic self-energy, respectively. We note that the exponential factor allows to close the integration path over the upper complex half plane in Eq. (6). As $W^{\mathrm{c}}(\mathbf{r},\mathbf{r}';\omega)$ falls off quickly enough with increasing frequencies, we may take the limit $\eta\to 0$ before integrating in Eq. (7).

The excitation energies $E^{\sigma}_{n\mathbf{q}}$ of the $N+1$ and $N-1$ particle system (for unoccupied and occupied states n, respectively) form the poles of the renormalized Green function, which can be calculated as corrections on the KS energies within first-order perturbation theory, yielding the nonlinear equation

$$E^{\sigma}_{n\mathbf{q}} = \epsilon^{\sigma}_{n\mathbf{q}} + \langle\varphi^{\sigma}_{n\mathbf{q}}|\Sigma^{\sigma}_{\mathrm{xc}}(E^{\sigma}_{n\mathbf{q}}) - v^{\sigma}_{\mathrm{xc}}|\varphi^{\sigma}_{n\mathbf{q}}\rangle\,, \tag{8}$$

where $v^{\sigma}_{\mathrm{xc}}(\mathbf{r})$ is the LDA exchange-correlation potential. While the expectation value of the latter and the Kohn-Sham energies are routinely calculated in the DFT code, we are left with the task of evaluating the expectation value $\langle\varphi^{\sigma}_{n\mathbf{q}}|\Sigma^{\sigma}_{\mathrm{xc}}(E^{\sigma}_{n\mathbf{q}})|\varphi^{\sigma}_{n\mathbf{q}}\rangle$, which decomposes into an exchange and a correlation term according to Eqs. (6) and (7). Finally, we must solve the nonlinear Eq. (8). Because of the exponential factor in Eq. (6), we can formally close the frequency integration contour with an infinite half circle over the positive complex plane without changing the value of the integral. This contour integral then equals the sum over the residues of the poles of the Green function. The expectation value of the exchange term with respect to a wave function $\varphi^{\sigma}_{n\mathbf{q}}(\mathbf{r})$ yields the well-known Hartree-Fock (HF) expression

$$\langle\varphi^{\sigma}_{n\mathbf{q}}|\Sigma^{\sigma}_{\mathrm{x}}|\varphi^{\sigma}_{n\mathbf{q}}\rangle = -\sum_{\mathbf{k}}^{\mathrm{BZ}}\sum_{n'}^{\mathrm{occ.}}\int \varphi^{\sigma *}_{n\mathbf{q}}(\mathbf{r})\varphi^{\sigma}_{n'\mathbf{k}}(\mathbf{r})v(|\mathbf{r}-\mathbf{r}'|)\varphi^{\sigma *}_{n'\mathbf{k}}(\mathbf{r}')\varphi^{\sigma}_{n\mathbf{q}}(\mathbf{r}')\,d^3r\,d^3r' \tag{9}$$

and from (7) we obtain

$$\begin{aligned}\langle\varphi^{\sigma}_{n\mathbf{q}}|\Sigma^{\sigma}_{\mathrm{c}}(\omega)|\varphi^{\sigma}_{n\mathbf{q}}\rangle \;=\; & \frac{i}{2\pi}\lim_{\eta\to 0^+}\sum_{\mathbf{k}}^{\mathrm{BZ}}\sum_{n'}^{\mathrm{all}}\int_{-\infty}^{\infty}d\omega' \\ & \times\int\frac{\varphi^{\sigma *}_{n\mathbf{q}}(\mathbf{r})\varphi^{\sigma}_{n'\mathbf{k}}(\mathbf{r})W^{\mathrm{c}}(\mathbf{r},\mathbf{r}';\omega')\varphi^{\sigma *}_{n'\mathbf{k}}(\mathbf{r}')\varphi^{\sigma}_{n\mathbf{q}}(\mathbf{r}')}{\omega+\omega'-\epsilon^{\sigma}_{n'\mathbf{k}}+i\eta\,\mathrm{sgn}(\epsilon^{\sigma}_{n'\mathbf{k}}-\epsilon_{\mathrm{F}})}d^3r\,d^3r'\,.\end{aligned} \tag{10}$$

In contrast to Eq. (9), the frequency integral in the latter expression cannot be replaced by a sum over residues because the poles of W^{c} are unknown.

Hybrid functionals The adiabatic-connection formula [44, 45, 46] establishes a connection between the noninteracting Kohn-Sham system with the fully interacting one by scaling the electron-electron interaction $\lambda v(r)$ from $\lambda = 0$ to $\lambda = 1$. In the weakly interacting limit, the

formula becomes identical to the HF exchange term, which motivated Becke [47, 16, 10] to replace a fraction a of the local exchange functional of DFT by the same fraction of nonlocal HF exchange energy

$$E_{\rm xc}^{\rm HYB} = E_{\rm xc}^{\rm L} + a\left(E_{\rm x}^{\rm HF} - E_{\rm x}^{\rm L}\right) , \tag{11}$$

where $E_{\rm xc}^{\rm L}$ denotes the local xc functional and $E_{\rm xc}^{\rm L}$ its exchange part.

$$\begin{aligned} E_{\rm xc}^{\rm HF} &= -\frac{1}{2}\sum_{\mathbf{q},\mathbf{k}}^{\rm BZ}\sum_{n,n'}^{\rm occ.}\int \varphi_{n\mathbf{q}}^{\sigma *}(\mathbf{r})\varphi_{n'\mathbf{k}}^{\sigma}(\mathbf{r})v(|\mathbf{r}-\mathbf{r}'|)\varphi_{n'\mathbf{k}}^{\sigma *}(\mathbf{r}')\varphi_{n\mathbf{q}}^{\sigma}(\mathbf{r}')d^3r\, d^3r' \\ &= \frac{1}{2}\sum_{\mathbf{q}}^{\rm BZ}\sum_{n}^{\rm occ.}\langle\varphi_{n\mathbf{q}}^{\sigma}|\Sigma_{\rm x}^{\sigma}|\varphi_{n\mathbf{q}}^{\sigma}\rangle \end{aligned} \tag{12}$$

is the HF exchange energy evaluated with the Kohn-Sham wave functions. The last equality shows that there is a direct relation to the expectation value of the exchange self-energy, Eq. (9). As the wave functions are functionals of the effective potential, which in turn is a functional of the density, $E_{\rm xc}^{\rm HF}$ is a true functional of the density, too.

By assuming a certain shape for the adiabatic-connection integrand, Perdew *et al.* [17] deduced a mixing parameter $a = 0.25$. With the Perdew-Burke-Ernzerhof (PBE) functional [6] for the local part, the resulting functional

$$E_{\rm xc}^{\rm PBE0} = E_{\rm xc}^{\rm PBE} + a\left(E_{\rm x}^{\rm HF} - E_{\rm xc}^{\rm PBE}\right) \tag{13}$$

is nowadays referred to as PBE0. For localized basis sets such as Gaussian-type functions, the long-range part of the nonlocal HF term is particularly expensive to evaluate. Therefore, Heyd *et al.* [48, 49] replaced it by a simple local functional, whereas the short-range part is still treated with a nonlocal potential. For this, they decomposed the bare Coulomb potential into a long-range (LR) and a short-range (SR) part

$$v(r) = \frac{\mathrm{erf}(\kappa r)}{r} + \frac{\mathrm{erfc}(\kappa r)}{r} = v^{\rm LR}(r) + v^{\rm SR}(r) , \tag{14}$$

where $\mathrm{erf}(x)$ and $\mathrm{erfc}(x) = 1-\mathrm{erf}(x)$ are the error function and its complement, respectively, and κ is an adjustable screening parameter. Later, this approach was demonstrated to even yield a better description of semiconductor band gaps than PBE0 [50]. The HSE hybrid functional is thus given by

$$E_{\rm xc}^{\rm HSE}(\kappa) = E_{\rm xc}^{\rm PBE} + a\left[E_{\rm x}^{\rm HF,SR}(\kappa) - E_{\rm xc}^{\rm PBE,SR}(\kappa)\right] , \tag{15}$$

where $E_{\rm x}^{\rm HF,SR}(\kappa)$ corresponds to Eq. (12) with the bare Coulomb potential $v(r)$ replaced by $v^{\rm SR}(r)$. The numerical evaluation of $E_{\rm x}^{\rm PBE,SR}(\kappa)$, the local functional for the SR exchange according to the decomposition given in Eq. (14), is described in Refs. 48 and 51. The screening parameter was fitted to a set of benchmark data for molecules yielding $\kappa = 0.15$ [48]. Later Krukau *et al.* published a slightly different value, $\kappa = 0.11$, which was optimized for solids [52]. We employ the latter value in our implementation.

Hybrid functionals are usually applied within the generalized KS formalism [15], which differs from the KS formalism by the fact that the effective potential, in which the fictitious noninteracting electrons move, is not necessarily local. It may contain a nonlocal part in addition to the local part so that the wave functions of the particles are solutions of the differential equation

$$[-\frac{1}{2}\nabla^2 + V^{\sigma,\rm L}(\mathbf{r})]\varphi_{n\mathbf{q}}^{\sigma}(\mathbf{r}) + a\int V^{\sigma,\rm NL}(\mathbf{r},\mathbf{r}')\varphi_{n\mathbf{q}}^{\sigma}(\mathbf{r}')d^3r = \epsilon_{n\mathbf{q}}^{\sigma}\varphi_{n\mathbf{q}}^{\sigma}(\mathbf{r}) , \tag{16}$$

where we have already included the mixing parameter a. The local part $V^{\sigma,\mathrm{L}}(\mathbf{r})$ consists of the contributions that are local *per se*, i.e., the external potential created by the nuclear charges, the Hartree potential (the electrostatic potential produced by the total electron charge density), as well as a contribution that derives from functional differentiation of the local parts of Eqs. (13) and (15) for the PBE0 and HSE functionals, respectively. The implementation of this local part of the xc potential requires only minor modifications of the DFT code, and we will focus on the nonlocal part $V^{\sigma,\mathrm{NL}}(\mathbf{r},\mathbf{r}')$ in the following, which derives from the nonlocal exchange energy functional E_x^HF. Leaving out the scaling factor a, its matrix representation in the basis of Kohn-Sham eigenstates and in reciprocal space is given by

$$\begin{aligned} V^{\sigma,\mathrm{NL}}_{\mathrm{x},nn'}(\mathbf{q}) &= -\sum_{\mathbf{k}}^{\mathrm{BZ}}\sum_{m}^{\mathrm{occ.}} \iint d^3r\, d^3r' \varphi^{\sigma *}_{n\mathbf{q}}(\mathbf{r})\varphi^{\sigma}_{m\mathbf{k}}(\mathbf{r}) v(|\mathbf{r}-\mathbf{r}'|)\varphi^{\sigma *}_{m\mathbf{k}}(\mathbf{r}')\varphi^{\sigma}_{n'\mathbf{q}}(\mathbf{r}') \qquad (17) \\ &= \langle \varphi^{\sigma}_{n\mathbf{q}} | \Sigma^{\sigma}_\mathrm{x} | \varphi^{\sigma}_{n'\mathbf{q}} \rangle \,, \end{aligned}$$

the diagonal elements of which correspond to the expectation value of the exchange self-energy, Eq. (9). In a sense, the hybrid functionals can be regarded as alternative approximations to the electronic self-energy. In fact, the resulting one-particle energies are often in much better agreement to experiment than the usual Kohn-Sham energies within the LDA or GGA, as we will see in Sec. 4. Of course, Eqs. (13) and (15) miss the frequency dependence, which is present in the *GW* self-energy. On the other hand, the hybrid-functional calculations are carried out iteratively until self-consistency in the electron density is achieved, while *GW* calculations are usually performed only perturbatively as *one-shot* calculations.

The sum over the occupied states in Eq. (17) involves core and valence states. Core states are dispersionless, which can be shown to lead to particularly simple and computationally cheap expressions for their contribution to the exchange term [53]. The valence states, on the other hand, show a distinct $\mathbf{k}$ dependence, which must be taken into account properly. Here we employ the mixed product basis (MPB) [54, 29], which is introduced in the next section.

For the HSE functional, the bare interaction $v(r)$ in Eq. (17) would have to be replaced by the short-range interaction $v^\mathrm{SR}(r)$. (Then the last equality would turn into an inequality, of course). Yet in practice, we first evaluate the nonlocal potential in the form of Eq. (17) and subtract a corresponding potential with $v^\mathrm{LR}(r)[= v(r) - v^\mathrm{SR}(r)]$ afterwards, as will be explained in the next section.

3 Implementation

3.1 Basis sets – FLAPW and mixed product basis

Our implementation is based on the all-electron FLAPW method [55, 56, 57], in which space is partitioned into non-overlapping atom-centered muffin-tin (MT) spheres and the remaining interstitial region (IR). The fully relativistic Dirac equation is employed to determine the core states, which are confined to the spheres. The valence and conduction states are obtained by solving Eq. (16) in a basis representation, by which the one-particle differential equations turn into a generalized eigenvalue problem. The basis functions are defined differently in the two regions of space: plane waves $e^{i(\mathbf{k}+\mathbf{G})\mathbf{r}}$ with $|\mathbf{k}+\mathbf{G}| \leq G_\mathrm{max}$ in the IR and linear combinations of

$u_{lp}^{a\sigma}(r)Y_{lm}(\hat{\mathbf{r}})$ in the MT spheres, where r is measured from the sphere center, $u_{lp}^{a\sigma}(r)$ are numerical functions defined on a radial grid, $Y_{lm}(\mathbf{r})$ are spherical harmonics with angular-momentum quantum numbers $0 \leq l \leq l_{\max}$ and $|m| \leq l$, a labels the atom in the unit cell, and p is an index for different radial functions. $G_{\max}$ and $l_{\max}$ are cutoff parameters. The linear combinations are such that the basis functions and their radial derivatives are continuous at the MT sphere boundaries. The radial functions $u_{lp}^{a\sigma}(r)$ are constructed from the radial scalar-relativistic KS equation with the spherical part of the local effective potential. In this way, the basis functions are optimized for the given physical system. Simply speaking, the radial functions already represent approximate solutions of the one-particle KS equations.

Hybrid functionals and the *GW* approximation are methods that distinguish themselves from conventional DFT with local (LDA) or semilocal (GGA) functionals by the fact that individual two-particle scattering processes are described explicitly. In each scattering event the state of the incoming particle and the state that it scatters into form products of wave functions. This is apparent in the above formulas for the different physical quantities, such as the HF potential [Eq. (17)], the polarization function [Eq. (2)], the self-energy [Eqs. (6) and (7)], and so on. All these are given as six-dimensional integrals over products of wave functions. Thus, if the integral equations are rewritten in an auxiliary basis constructed for these product functions, they become matrix equations, which can easily be treated in a computer code using standard linear algebra libraries. In the context of the FLAPW method we have found the mixed product basis (MPB) [29] to be an optimal choice, which consists of two separate sets of functions that are defined only in one of the spatial regions, while being zero in the other. We will describe this basis in the following.

From the above basis representation inside the MT spheres, we would naively just take the product functions $U_{LP}^{a\sigma}(r) = u_{lp}^{a\sigma}(r)u_{l'p'}^{a\sigma}(r)$ as the radial part of a MPB function, while the spherical harmonics $Y_{lm}(\hat{\mathbf{r}})$ and $Y_{l'm'}(\hat{\mathbf{r}})$ multiply to linear combinations of spherical harmonics $Y_{LM}(\hat{\mathbf{r}})$ again with $|l - l'| \leq L \leq l + l'$ and $-L \leq M \leq L$. The index P counts all possible combinations of l, l', p, and p'. However, the set $\{U_{LP}^{a\sigma}(r)\}$ is very large and usually has a high degree of (near) linear dependence. An effective procedure to reduce the size of the set and to remove the linear dependences is to diagonalize the overlap matrix of $\{U_{LP}^{a\sigma}(r)\}$ and to retain only those eigenvectors whose eigenvalues exceed a specified threshold value [58]. By using both spin-up and spin-down products in the construction of the overlap matrix, we make the resulting basis spin independent. In practice, the basis set is reduced further by introducing a cutoff value $L_{\max}$ for the angular quantum number, which can be chosen much smaller than the theoretically exact limit of $2l_{\max}$, and by restricting the product functions to certain combinations of p and p'. On the other hand, it must be supplemented with a constant MT function for each atom in the unit cell, which is later needed to represent the eigenfunction that corresponds to the divergent eigenvalue of the Coulomb matrix in the limit $\mathbf{k} \to \mathbf{0}$. At $\mathbf{k} = \mathbf{0}$, this eigenfunction is the constant function. From the resulting MT functions $M_{LMP}^{a}(\mathbf{r}) = M_{LP}^{a}(r)Y_{LM}(\hat{\mathbf{r}})$, we formally construct Bloch functions.

In the IR, we have to form products of plane waves, which are plane waves $M_{\mathbf{G}}^{\mathbf{k}}(\mathbf{r}) = e^{i(\mathbf{k}+\mathbf{G})\mathbf{r}}$ again. As above, the cutoff value $|\mathbf{k} + \mathbf{G}| \leq G'_{\max}$ can be chosen much smaller than the exact limit $2G_{\max}$ in practice. Together with the MT functions, we thus obtain the MPB $\{M_I^{\mathbf{k}}(\mathbf{r})\} = \{M_{LMP}^{a,\mathbf{k}}(\mathbf{r}), M_{\mathbf{G}}^{\mathbf{k}}(\mathbf{r})\}$ for the representation of wave-function products. Since the interstitial plane

waves are not orthogonal to each other, we must introduce the biorthogonal set $\{\tilde{M}^{\mathbf{k}}_{\mathbf{G}}(\mathbf{r}) = \sum_{\mathbf{G}'} M^{\mathbf{k}}_{\mathbf{G}'}(\mathbf{r}) O^{-1}_{\mathbf{G}'\mathbf{G}}(\mathbf{k})\}$, too, where $O_{\mathbf{G}'\mathbf{G}}(\mathbf{k})$ is the overlap matrix, which can be calculated analytically. (We note that the functions $M^{a,\mathbf{k}}_{LMP}(\mathbf{r})$ are orthonormal by construction.) In the Hilbert space spanned by the MPB, the two sets can be combined to yield the completeness relations

$$\sum_I |M^{\mathbf{k}}_I\rangle\langle\tilde{M}^{\mathbf{k}}_I| = \sum_I |\tilde{M}^{\mathbf{k}}_I\rangle\langle M^{\mathbf{k}}_I| = 1\,, \tag{18}$$

which can be used to decouple the $\mathbf{r}$ and $\mathbf{r}'$ spaces in the nonlocal integrals. This technique is also called *resolution of the identity*. Sometimes, it is helpful to combine the sets $\{M^{a,\mathbf{k}}_{LMP}(\mathbf{r})\}$ and $\{M^{\mathbf{k}}_{\mathbf{G}}(\mathbf{r})\}$ to form a new set of functions that are continuous at the MT sphere boundaries. This basis set contains less functions without a loss of accuracy, which can increase the efficiency of the code. Furthermore, the elimination of the discontinuities can improve the numerical stability if matrices are diagonalized or inverted, e.g., the Coulomb and dielectric matrix in the *GW* approximation as well as the response matrix in the optimized effective potential method [59, 60].

3.2 MPB formulation

Let us first apply the MPB to the nonlocal potential Eq. (17) for the hybrid functionals. By placing the completeness relation Eq. (18) at both sides of $v(|\mathbf{r}-\mathbf{r}'|)$, the integrations over $\mathbf{r}$ and $\mathbf{r}'$ get decoupled, and the six-dimensional integral is replaced by a sum over vector-matrix-vector products

$$\begin{aligned} V^{\sigma,\mathrm{NL}}_{\mathrm{x},nn'}(\mathbf{q}) &= -\sum_m^{\mathrm{occ.}} \sum_{\mathbf{k}}^{\mathrm{BZ}} \sum_{IJ} \langle\varphi^{\sigma}_{n\mathbf{q}}|\varphi^{\sigma}_{m\mathbf{q}-\mathbf{k}} M_{\mathbf{k}I}\rangle v_{IJ}(\mathbf{k}) \langle M_{\mathbf{k}J}\varphi^{\sigma}_{m\mathbf{q}-\mathbf{k}}|\varphi^{\sigma}_{n'\mathbf{q}}\rangle \\ &= \langle\varphi^{\sigma}_{n\mathbf{q}}|\Sigma^{\sigma}_{\mathrm{x}}|\varphi^{\sigma}_{n'\mathbf{q}}\rangle \end{aligned} \tag{19}$$

with the usual bra-ket notation $\langle f|g\rangle = \int d^3r\, f^*(\mathbf{r}) g(\mathbf{r})$. The Coulomb matrix [61]

$$v_{IJ}(\mathbf{k}) = \iint d^3r\, d^3r'\, \tilde{M}^*_{\mathbf{k}I}(\mathbf{r}) v(|\mathbf{r}-\mathbf{r}'|) \tilde{M}_{\mathbf{k}J}(\mathbf{r}')\,, \tag{20}$$

which still involves a six-dimensional integration, must be evaluated only once at the beginning of the self-consistency cycle. In the same manner, Eqs. (2), (3), (9), and (10) become algebraic matrix equations in the space of the MPB. Equation (3) becomes particularly simple if we perform a basis transformation $\{M^{\mathbf{k}}_I(\mathbf{r})\} \rightarrow \{E^{\mathbf{k}}_{\mu}(\mathbf{r})\}$ that diagonalizes the Coulomb matrix. We note that no approximation is involved at this stage. The new normalized basis functions are necessarily orthogonal, and we do not need a biorthogonal set. In this new basis, Eq. (3) becomes

$$W_{\mu\nu}(\mathbf{k},\omega) = v_{\mu}(\mathbf{k})\delta_{\mu\nu} + v_{\mu}(\mathbf{k}) \sum_{\gamma} P_{\mu\gamma}(\mathbf{k},\omega) W_{\gamma\nu}(\mathbf{k},\omega)\,, \tag{21}$$

which by inversion yields

$$W_{\mu\nu}(\mathbf{k},\omega) = \varepsilon^{-1}_{\mu\nu} \sqrt{v_{\mu}(\mathbf{k}) v_{\nu}(\mathbf{k})} \tag{22}$$

with the dielectric matrix

$$\varepsilon_{\mu\nu}(\mathbf{k},\omega) = \delta_{\mu\nu} - P_{\mu\nu}(\mathbf{k},\omega) \sqrt{v_{\mu}(\mathbf{k}) v_{\nu}(\mathbf{k})}\,. \tag{23}$$

The last two equations do not contain any matrix multiplications, but only scalar products with $v_\mu(\mathbf{k})$, the eigenvalues of the Coulomb matrix [Eq. (20)]. In Sec. 3.4 we will come back to this special basis.

We now turn back to the hybrid functionals and, in particular, to the HSE functional, which is defined in terms of a short-range (or model screened) interaction v^{SR} defined in Eq. (14). The way of implementation seems obvious now: the bare Coulomb potential v in Eq. (19) for the PBE0 functional is simply replaced by v^{SR}. However, in this way we would loose a very favorable property of the bare Coulomb matrix, Eq. (20), namely that it can be made sparse by a simple unitary transformation of the MPB (see Sec. 3.4). The sparsity of $v_{IJ}(\mathbf{q})$ speeds up the matrix-vector multiplications in Eq. (19) considerably, while $v^{\mathrm{SR}}_{IJ}(\mathbf{q})$ does not have this mathematical property. Therefore, we evaluate Eq. (19) with the bare interaction as in the PBE0 case and subtract a corresponding expression, where we replace v by v^{LR}, the long-range interaction defined in Eq. (14). While $v(r)$ and $v^{\mathrm{SR}}(r)$ diverge at $r = 0$, $v^{\mathrm{LR}}(r)$ remains finite there and behaves like $v(r)$ for large r. So, it has a very smooth behavior for all distances and should thus be suitable to be described in reciprocal space. In fact, we find that its Fourier transform

$$v^{\mathrm{LR}}_{\mathbf{k}} = \frac{4\pi}{k^2} e^{-ik^2/(4\kappa^2)} \tag{24}$$

falls off rapidly with increasing k. The potential for the long-range interaction corresponding to Eq. (19) can thus be evaluated in reciprocal space

$$V^{\sigma,\mathrm{NL,LR}}_{\mathrm{x},nn'}(\mathbf{q}) = -\sum_{m}^{\mathrm{occ.}} \sum_{\mathbf{k}}^{\mathrm{BZ}} \sum_{\mathbf{G}} \langle \varphi^{\sigma}_{n\mathbf{q}} | \varphi^{\sigma}_{m\mathbf{q}-\mathbf{k}} \frac{e^{i(\mathbf{k}+\mathbf{G})\mathbf{r}}}{\sqrt{V}} \rangle v^{\mathrm{LR}}_{\mathbf{k}+\mathbf{G}} \langle \frac{e^{i(\mathbf{k}+\mathbf{G})\mathbf{r}}}{\sqrt{V}} \varphi^{\sigma}_{m\mathbf{q}-\mathbf{k}} | \varphi^{\sigma}_{n'\mathbf{q}} \rangle \tag{25}$$

with the crystal volume V and

$$\langle \varphi^{\sigma}_{n\mathbf{q}} | \varphi^{\sigma}_{m\mathbf{q}-\mathbf{k}} \frac{e^{i(\mathbf{k}+\mathbf{G})\mathbf{r}}}{\sqrt{V}} \rangle = \sum_{I} \langle \varphi^{\sigma}_{n\mathbf{q}} | \varphi^{\sigma}_{m\mathbf{q}-\mathbf{k}} M_{\mathbf{k}I} \rangle \langle \tilde{M}_{\mathbf{k}I} | \frac{e^{i(\mathbf{k}+\mathbf{G})\mathbf{r}}}{\sqrt{V}} \rangle \,, \tag{26}$$

where the first integrals on the right-hand side are calculated routinely already for $V^{\sigma,\mathrm{NL}}_{\mathrm{x},nn'}(\mathbf{q})$. The nonlocal short-range potential needed for HSE is then given by

$$V^{\sigma,\mathrm{NL,SR}}_{\mathrm{x},nn'}(\mathbf{q}) = V^{\sigma,\mathrm{NL}}_{\mathrm{x},nn'}(\mathbf{q}) - V^{\sigma,\mathrm{NL,LR}}_{\mathrm{x},nn'}(\mathbf{q}) \,. \tag{27}$$

We note that any other form of the screened Coulomb interaction could easily be implemented at this stage. Since the long-range interaction is diagonal in reciprocal space, the evaluation of Eq. (25) takes in practical terms negligible time to compute. From the fact that the Fourier transform Eq. (24) approaches zero very quickly with k, it is clear that the results are easily converged up to machine precision, even if the Fourier coefficients in Eq. (26) fall off very slowly because of the rapidly varying all-electron wave functions. Since $v^{\mathrm{SR}}(r)$ can be understood as a model screened interaction, one might anticipate that a similar treatment of the long-range (or correlation) part W^{c} of the dynamically screened interaction in the GW approximation [Eq. (5)], can give rise to a similar speed-up of the computation time. We will demonstrate in Sec. 3.4 that this is, in fact, possible even without a projection onto plane waves.

3.3 Frequency dependence in *GW*

The *GW* approximation for the self-energy involves quantities that are time or frequency dependent such as the Green function, the polarization function, and the screened interaction. In this section, we show how this frequency dependence is treated in our code.

The polarization function describes the charge redistributions within a many-electron system due to a change in the effective potential. The electrons react quickly to this change but not instantaneous, making the polarization function dependent on the time that has passed since the perturbation or, after Fourier transformation, dependent on frequency. In the basis of eigenstates, the charge redistribution is realized by the formation of electron-hole pairs. Simply speaking, the expression in Eq. (2) can be understood as the summed response of a large number of oscillators with eigenfrequencies $\epsilon^{\sigma}_{n'\mathbf{k}} - \epsilon^{\sigma}_{n\mathbf{q}}$ (corresponding to the electron-hole pairs) to a perturbation that oscillates with frequency ω.

The response of the individual oscillators have a finite value over all frequencies, which complicates a direct summation over the Brillouin zone. It is more convenient to consider the representation $(\operatorname{Im} P)_{IJ}(\mathbf{k},\omega)$ of the imaginary part $\operatorname{Im} P(\mathbf{r},\mathbf{r}';\omega)$ first, which is obtained by replacing expressions of the form $1/(a \pm i\eta)$ by $\mp\pi\delta(a)$. This simplifies the BZ summation significantly. Afterwards a Hilbert transformation yields the full polarization matrix $P_{IJ}(\mathbf{k},\omega)$, where the frequency argument may be complex. In particular, this allows an evaluation on the imaginary-frequency axis, where the frequency-dependent quantities show a smooth behavior and can therefore be sampled and interpolated with few frequency points. As the bracket in Eq. (2) is real for frequencies on the imaginary axis, the corresponding matrix $P_{IJ}(\mathbf{k},i\omega)$ with $\omega \in \mathbb{R}$ becomes Hermitian; it even becomes real symmetric if the system exhibits inversion symmetry and we use a symmetrized MPB as described in Sec. 3.4.

In contrast to the exchange self-energy, the frequency integral in Eq. (7) cannot be replaced by a sum over residues because the positions of the poles of $W^{\mathrm{c}}_{\mu\nu}(\mathbf{k},\omega) = W_{\mu\nu}(\mathbf{k},\omega) - \delta_{\mu\nu}v_{\mu}(\mathbf{k})$ in the complex-frequency plane are unknown. Therefore, the correlation self-energy still contains an explicit integration over frequencies. Unfortunately, the integrand has a lot of structure along the real frequency axis, which makes a direct evaluation difficult. There are two methods that avoid the integration over real frequencies and use the imaginary axis instead: analytic continuation [62] and contour integration [63, 64]. The former allows a faster and easier implementation, but contains a badly controlled fitting procedure, which can be tested with the more accurate contour-integration method. In the latter, the frequency integration path is chosen so as to avoid the real axis in the best possible way. It falls into two contributions: an integral that runs from $-i\infty$ to $+i\infty$ along the imaginary frequency axis and another integral that runs the perimeter of a rectangle only containing poles of the KS Green function. Since these poles are known, the latter integral is easily calculated as a sum over the residues. We have implemented both algorithms and find that they give similar results for the systems considered here. In the following, we hence discuss only the first approach in more detail.

The analytic-continuation method starts with the calculation of the self-energy for imaginary

frequencies

$$\langle\varphi^\sigma_{n\mathbf{q}}|\Sigma^\sigma_\mathrm{c}(i\omega)|\varphi^\sigma_{n\mathbf{q}}\rangle = -\frac{1}{2\pi}\lim_{\eta\to 0^+}\sum_{\mathbf{k}}^{\mathrm{BZ}}\sum_{n'}^{\mathrm{all}}\int_{-\infty}^{\infty}d\omega' \times\int\frac{\varphi^{\sigma*}_{n\mathbf{q}}(\mathbf{r})\varphi^\sigma_{n'\mathbf{k}}(\mathbf{r})W^\mathrm{c}(\mathbf{r},\mathbf{r}';i\omega')\varphi^{\sigma*}_{n'\mathbf{k}}(\mathbf{r}')\varphi^\sigma_{n\mathbf{q}}(\mathbf{r}')}{i\omega+i\omega'-\epsilon^\sigma_{n'\mathbf{k}}}d^3r\,d^3r'\,. \tag{28}$$

on a mesh of points $\{i\omega_n;\,\omega_n\geq 0\}$. The frequency integration is along the imaginary-frequency axis, where the integrand is much smoother than on the real axis. In practice, we use a discrete and finite mesh for the imaginary frequencies, which is dense near $\omega=0$ and contains typically 10-20 points. After evaluating Eq. (28), the self-energy is analytically continued to the whole complex frequency plane either by fitting to a model function given by a sum over N_p poles in the complex plane

$$f(\omega)=\sum_{\nu=1}^{N_\mathrm{p}}\frac{a_\nu}{\omega-\omega_\nu} \tag{29}$$

with complex fit parameters a_p and ω_p or by using a Padé approximant employing Thiele's reciprocal difference algorithm [65], which gives the approximant as a continued fraction. A subsequent search for the poles with the Newton method yields the self-energy again in the form of Eq. (29), usually with many more poles than is possible with the numerical fitting procedure. An accurate analytical continuation is characterized by the fact that all poles (or at least the dominant ones) are below the real frequency axis. We find that the Padé method is more precise than numerical fitting, but it can produce random outliers if a pole happens to appear too close to the real axis. The frequency convolution in Eq. (28) is either performed analytically with a Padé approximant again for the matrix elements of the screened interaction or by a cubic spline interpolation (see Ref. 54 for details).

After finding the parameters a_ν and ω_ν, the correlation self-energy is given by the analytical function

$$\langle\varphi^\sigma_{n\mathbf{q}}|\Sigma^\sigma_\mathrm{c}(\omega)|\varphi^\sigma_{n\mathbf{q}}\rangle=\begin{cases}f(\omega) & \text{for Re }\omega\geq 0\\ f^*(\omega^*) & \text{for Re }\omega<0\end{cases}\,, \tag{30}$$

which allows to solve the nonlinear quasiparticle Eq. (8) to machine precision with the standard iterative Newton method and without any additional linearization of the self-energy.

3.4 Tricks to reduce computational cost

As already mentioned, the explicit orbital dependence and the nonlocality in the effective potential makes DFT calculations with hybrid functionals very expensive. For the same reason and also because of the additional frequency dependence, the same is true for *GW* calculations. In this section, we discuss several numerical tricks that can be applied to reduce the computational expense of these methods. We start with those that can be applied equally to both methods.

Sparsity of Coulomb matrix The Coulomb matrix in the MPB representation, Eq. (20), consists of four distinct blocks, the diagonal parts MT-MT and IPW-IPW as well as the two off-diagonal parts MT-IPW and IPW-MT. Their evaluation was discussed in detail in Ref. 61. The vector-matrix-vector products in Eq. (19), where the wave function products are regarded

as vectors in the MPB, must be evaluated for each combination of band indices n, n', and n'' as well as Bloch vectors $\mathbf{k}$ and $\mathbf{q}$. This easily amounts to billion matrix operations or more and constitutes the computationally most expensive step in the algorithm. Fortunately, we can accelerate these matrix operations considerably, by making the Coulomb matrix sparse by a suitable unitary transformation of the MPB MT functions. These transformations are done within the subspaces of each atom and LM channel, so it involves only few basis functions per subspace. According to Eq. (20), the matrix elements $v_{IJ}(\mathbf{q})$ can be regarded as the electrostatic energy of two charge distributions described by MPB functions. So, it makes sense to define a formal multipole moment for the MPB functions in the muffin-tin spheres

$$\mu^a_{LP} = \int_0^{S_a} M^a_{LP}(r)\, r^{L+2} dr\,. \tag{31}$$

Now, by forming linear combinations

$$M^{a\,\prime}_{L1}(r) = \frac{\mu^a_{L1} M^a_{L1}(r) + \mu^a_{Ln} M^a_{Ln}(r)}{\sqrt{{\mu^a_{L1}}^2 + {\mu^a_{Ln}}^2}} \tag{32a}$$

$$M^{a\,\prime}_{Ln}(r) = \frac{\mu^a_{Ln} M^a_{L1}(r) - \mu^a_{L1} M^a_{Ln}(r)}{\sqrt{{\mu^a_{L1}}^2 + {\mu^a_{Ln}}^2}}\,, \tag{32b}$$

we can make the multipole moment of the nth function vanish. By a successive application of this procedure in each subspace, only one of the resulting functions (the first) will have a nonzero multipole moment. The "charge distributions" represented by all other MT functions do not generate an electrostatic potential outside the MT spheres so that Coulomb matrix elements involving an element of this set can only be nonzero, if the other function is a MT function residing in the same MT sphere; all other matrix elements must vanish. This leads to a very sparse form of the Coulomb matrix, which drastically reduces the number of floating point operations needed in evaluating Eq. (19) and thus the computational cost.

Truncation of matrices The computational cost can be reduced significantly by introducing a cutoff for the basis representation of matrices without compromising the accuracy. Let us start with the nonlocal potential for the hybrid functionals. In Eq. (17) we have represented the exchange operator in terms of the wave functions rather than the LAPW basis functions. Although important, the exchange energy is a relatively small energy contribution compared to kinetic and potential energies. Therefore, we can afford to describe the nonlocal exchange potential in a subspace of wave functions up to a band cutoff $n_{\max}$, all other matrix elements are set to zero. We find that the results converge reasonably fast with the cutoff $n_{\max}$.

Another cutoff can be introduced in the calculation of the GW correlation self-energy. The contribution of Eq. (7) is smaller than the exchange self-energy, Eq. (6), which allows to use a reduced set $\{E^{\mathbf{k}}_{\mu}(\mathbf{r})\}$ for the correlation part. If we assume that the eigenvalues $v_\mu(\mathbf{k})$ are ordered according to decreasing size, then matrix elements $\varepsilon_{\mu\nu}(\mathbf{k},\omega)$ and $W_{\mu\nu}(\mathbf{k},\omega)$ with large indices will be relatively small, cf. Eqs. (22) and (23). We may then introduce a threshold value $v_{\min}$ for the eigenvalues and only retain the functions $E^{\mathbf{k}}_{\mu}(\mathbf{r})$ with $v_\mu(\mathbf{k}) \geq v_{\min}$. We thus restrict ourselves to the dominant part of the electron-electron interaction. The removal of basis functions with small eigenvalues can be viewed as an optimization step for the MPB, because

it reduces the matrix sizes and hence the computational cost. Note that with $v_{\min} = 0$, the full accuracy of the MPB is restored. In our implementation, this optimization of the MPB only affects the correlation self-energy while we calculate the exchange self-energy always with the full MPB.

Symmetry Spatial and time reversal symmetries are exploited to accelerate the code in three ways: (1) Inversion symmetry leads to real-valued quantities such as the Coulomb matrix $v_{IJ}(\mathbf{q})$, the polarization matrix $P_{IJ}(\mathbf{q}, i\omega)$ and the screened interaction $W_{IJ}(\mathbf{q}, i\omega)$ for $\omega \in \mathbb{R}$. (2) The $\mathbf{q}$ and $\mathbf{k}$ vector in Eq. (17) can be chosen from a reduced set of Bloch vectors, i.e., from the irreducible wedge of the BZ and from an *extended* irreducible BZ, respectively. And (3), if the wave functions $\varphi^{\sigma}_{n\mathbf{k}}$ and $\varphi^{\sigma}_{n'\mathbf{k}}$ in Eq. (17) fall into different irreducible representations, the corresponding exchange matrix element vanishes. This can be used as a criterion whether an element must be calculated or not.

In general, the matrix representation of real operators (e.g., the Coulomb interaction) in an arbitrary complex basis $\{f_\mu(\mathbf{r})\}$ is Hermitian. If the system exhibits inversion symmetry and the basis functions fulfill $f_\mu(-\mathbf{r}) = f^*_\mu(\mathbf{r})$, the matrices become real symmetric. Similarly, the representation of wave-function products $\langle M_{\mathbf{q}I}\varphi^{\sigma}_{n\mathbf{k}}|\varphi^{\sigma}_{n'\mathbf{k}+\mathbf{q}}\rangle$, which appear in nearly all equations, are then real instead of complex. Of course, this reduces the computational cost considerably, in terms of both memory consumption and computation time. However, according to the current definition only the IPWs fulfill the above condition, while the MT functions do not. We hence apply a unitary transformation of the MT functions such that the condition is satisfied for the whole basis [66]. From the form of the condition it is clear that the transformation forms linear combinations of MT functions that reside in different, but symmetry-equivalent MT spheres, resulting in functions that resemble bonding and antibonding states. (If the atom is placed in the origin, linear combinations of different magnetic quantum numbers are formed.) In the following, it is understood that all quantities are represented in this symmetrized basis if inversion symmetry is present. We note that this symmetrization leaves the sparsity of the Coulomb matrix intact.

In a reciprocal space formulation, the nonlocal form of the interaction potentials, the GW self-energy, etc. gives rise to computationally expensive double BZ summations. For example, the nonlocal potential [Eq. (17)] at a point $\mathbf{q}$ does not depend only on quantities at that point in reciprocal space but also on the Coulomb matrix and wave functions at all other points in the BZ. Fortunately, if the system is spatially invariant under symmetry operations, we can reduce the computational expense considerably. Here, invariance means that a given symmetry operation Q commutes with the Hamiltonian H, i.e., $QH = HQ$, such that $Q\varphi$ is an eigenstate of H if φ is an eigenstate. Hence, the solutions of the one-particle equations at two different $\mathbf{q}$ points are equivalent, if the $\mathbf{q}$ vectors are related by a symmetry operation. This can be used to restrict the set of $\mathbf{q}$ points, at which the Hamiltonian must be diagonalized, to a smaller set, the so-called irreducible Brillouin zone (IBZ). Of course, this is nothing new, as the IBZ is routinely employed in computer codes that are used to treat systems with periodic boundary conditions. However, we can restrict the additional $\mathbf{k}$ summations in the calculation of the nonlocal quantities in a similar way, with the restriction that, due to the additional dependence on $\mathbf{k}$ and $\mathbf{q}-\mathbf{k}$, only those symmetry operations $Q^{\mathbf{q}}_i$ can be employed that leave the given $\mathbf{q}$

vector invariant, i.e., $Q_i^{\mathbf{q}}\mathbf{q} = \mathbf{q} + \mathbf{G}_i^{\mathbf{q}}$, where $\mathbf{G}_i^{\mathbf{q}}$ is a reciprocal lattice vector that folds the vector back into the BZ if $Q_i^{\mathbf{q}}\mathbf{q}$ is pointing out of it. This subset of operations $\{Q_i^{\mathbf{q}}\}$ is commonly called *little group* LG($\mathbf{q}$). In the same way as for the IBZ, the little group gives rise to a minimal set of inequivalent $\mathbf{k}$ points, which we denote by the extended IBZ [EIBZ($\mathbf{q}$)]. Depending on the particular quantity, the strategies to apply the EIBZ($\mathbf{q}$) are different. The basic strategy is to replace the summation over $\mathbf{k}$ by a summation over the EIBZ($\mathbf{q}$) and over the symmetry operations. The latter is performed such that it produces only little overhead so that the net computation time is much faster than if we summed over the whole BZ. In the following, we only give the final expressions and give additional explanations where necessary. For simplicity, non-symmorphic and time-reversal symmetry operations are omitted. The formulas can be generalized easily to take these operations into account as well (cmp. Refs. 39 and 54).

We first apply the extended IBZ to the polarization function defined in Eq. (2) and represented in the MPB. The final expression is

$$P_{IJ}(\mathbf{k},\omega) = \sum_{i=1}^{N_A^{\mathbf{k}}} \sum_{\sigma} \sum_{\mathbf{q}}^{\mathrm{EIBZ}(\mathbf{k})} \frac{1}{N_{\mathrm{LG}(\mathbf{k},\mathbf{q})}} \sum_{n}^{\mathrm{occ}} \sum_{n'}^{\mathrm{unocc}} \langle Q_i^{\mathbf{k}} \tilde{M}_I^{\mathbf{k}} \varphi_{n\mathbf{q}}^{\sigma} | \varphi_{n'\mathbf{q}+\mathbf{k}}^{\sigma} \rangle \langle \varphi_{n'\mathbf{q}+\mathbf{k}}^{\sigma} | \varphi_{n\mathbf{q}}^{\sigma} Q_i^{\mathbf{k}} \tilde{M}_J^{\mathbf{k}} \rangle \, (...) \; , \tag{33}$$

where the factor $1/N_{\mathrm{LG}(\mathbf{k},\mathbf{q})}$ avoids double counting of $\mathbf{q}$ points. $N_{\mathrm{LG}(\mathbf{k},\mathbf{q})}$ is the number of symmetry operations that are members of both LG($\mathbf{k}$) and LG($\mathbf{q}$). The application of a symmetry operation to a MPB function can be written as a linear combination of MPB basis functions so that the sum over the symmetry operations can be performed at the very end after summing over the bands, the $\mathbf{q}$ points, and the electron spin. We note that this is also possible with the set $\{E_{\mu}^{\mathbf{k}}(\mathbf{r})\}$ instead of $\{M_I^{\mathbf{k}}(\mathbf{r})\}$. In a similar way, we can accelerate the evaluation of the expectation values of $\Sigma_{\mathrm{x}}^{\sigma}$ and $\Sigma_{\mathrm{c}}^{\sigma}(\omega)$. To this end, we write Eqs. (6) and (7) in a general form with a (possibly frequency-dependent) function $f(\mathbf{r},\mathbf{r}')$, which fulfills all symmetry properties of the system. Using the great orthogonality theorem of group theory [67, 54], we can then write

$$\begin{aligned}
\langle \varphi_{n\mathbf{q}}^{\sigma} | \Sigma^{\sigma} | \varphi_{n\mathbf{q}}^{\sigma} \rangle &= \sum_{\mathbf{k}}^{\mathrm{BZ}} \sum_{n'} \iint d^3r \, d^3r' \, \varphi_{n\mathbf{q}}^{\sigma *}(\mathbf{r}) \, \varphi_{n'\mathbf{k}}^{\sigma}(\mathbf{r}) \, \varphi_{n'\mathbf{k}}^{\sigma *}(\mathbf{r}') \, \varphi_{n\mathbf{q}}^{\sigma}(\mathbf{r}') \, f(\mathbf{r},\mathbf{r}') \\
&= \sum_{\mathbf{k}}^{\mathrm{EIBZ}(\mathbf{q})} \frac{N_{\mathrm{LG}(\mathbf{q})}}{N_{\mathrm{LG}(\mathbf{k},\mathbf{q})}(n_2 - n_1 + 1)} \sum_{m=n_1}^{n_2} \sum_{n'} \iint d^3r \, d^3r' \, \varphi_{m\mathbf{q}}^{\sigma *}(\mathbf{r}) \, \varphi_{n'\mathbf{k}}^{\sigma}(\mathbf{r}) \\
&\quad \times \varphi_{n'\mathbf{k}}^{\sigma *}(\mathbf{r}') \, \varphi_{m\mathbf{q}}^{\sigma}(\mathbf{r}') \, f(\mathbf{r},\mathbf{r}')
\end{aligned} \tag{34}$$

where the wave functions $\{\varphi_{m\mathbf{q}}^{\sigma}(\mathbf{r}), n_1 \leq m \leq n_2\}$ form an eigenspace with $n_1 \leq n \leq n_2$ and $N_{\mathrm{LG}(\mathbf{q})}$ is the number of elements in LG($\mathbf{q}$). Instead of summing over the symmetry operations, we average here over the degenerate states of which $\varphi_{n\mathbf{q}}^{\sigma}(\mathbf{r})$ is a member. This is the method of choice if only few diagonal elements must be calculated. For the hybrid functionals, however, we have to calculate a whole matrix according to Eq. (17). Here, we use a different strategy, which is akin to Eq. (33): we calculate a first matrix by summing only over the EIBZ($\mathbf{q}$) and then let all symmetry operations of LG($\mathbf{q}$) act on this matrix and sum up, which adds the contribution of all other $\mathbf{k}$ points. This time, the symmetry operations act on a matrix represented in the LAPW basis, which is particularly simple because it can be written as a one-to-one mapping,

which takes negligible computation time. With the definitions of above,

$$V_{\mathrm{x},\mathbf{G}\mathbf{G}'}^{\mathrm{NL},\sigma}(\mathbf{q}) = -\sum_{i}^{\mathrm{LG}(\mathbf{q})}\sum_{\mathbf{k}}^{\mathrm{EIBZ}(\mathbf{q})}\frac{1}{N_{\mathrm{LG}(\mathbf{k},\mathbf{q})}}\sum_{n}^{\mathrm{occ.}}\iint \chi^{\sigma *}_{\mathbf{q}(P_i^{\mathbf{q}}\mathbf{G}+\mathbf{G}_i^{\mathbf{q}})}(\mathbf{r})\varphi^{\sigma}_{n\mathbf{k}}(\mathbf{r})v(|\mathbf{r}-\mathbf{r}'|) \times\varphi^{\sigma *}_{n\mathbf{k}}(\mathbf{r}')\chi^{\sigma}_{\mathbf{q}(P_i^{\mathbf{q}}\mathbf{G}'+\mathbf{G}_i^{\mathbf{q}})}(\mathbf{r}')\,d^3r\,d^3r'\,. \tag{35}$$

Local orbitals transform in a similar way.

Finally, we can employ the great orthogonality theorem of group theory to reduce the cost of evaluating the exchange matrix in Eq. (17). This theorem demands that the matrix elements can only be nonzero, if the wave functions are members of the same irreducible representation. Since the irreducible representations are not available in our DFT code (and their evaluation in each iteration would be computationally expensive), we exploit the fact that the great orthogonality theorem applies to *any* operator that has the full symmetry of the system. A suitable operator is given by the MT step function $\Theta^{\mathrm{MT}}(\mathbf{r})$, which is one in the MT spheres and zero elsewhere. The calculation of its matrix elements $\langle\varphi^{\sigma}_{n\mathbf{k}}|\Theta^{\mathrm{MT}}|\varphi^{\sigma}_{n'\mathbf{k}}\rangle$ is elementary and takes negligible CPU time. These matrix elements can be used as a *probe* in the sense that we only calculate those exchange matrix elements for which the corresponding Θ^{MT} matrix elements are nonzero.

Treatment of Γ point The Γ point, i.e, $\mathbf{k}=\mathbf{0}$, is a special point in Eqs. (19), (22), and (23), because the long-range nature of the Coulomb interaction makes the Coulomb matrix $v_{IJ}(\mathbf{k})$ and also the screened interaction $W_{\mu\nu}(\mathbf{k},\omega)$ diverge in the limit $\mathbf{k}\to\mathbf{0}$. A proper treatment of this divergence is crucial to obtain a fast and stable convergence with respect to the $\mathbf{k}$-point sampling.

We start with Eq. (19). The integrand contains the Coulomb matrix, whose leading element is proportional to $1/k^2$ in the limit $\mathbf{k}\to\mathbf{0}$. Therefore, the three-dimensional integration over the BZ yields a finite value. We find that the contribution of the divergence is numerically important so that we cannot simply exclude the problematic Γ point from the $\mathbf{k}$-point set. Instead, the Coulomb matrix $v_{IJ}(\mathbf{k})$ is decomposed into a divergent and a nondivergent part [61]

$$v_{IJ}(\mathbf{k}) = \frac{4\pi}{V}\frac{1}{k^2}\langle\tilde{M}_I^{\mathbf{k}}|e^{i\mathbf{k}\cdot\mathbf{r}}\rangle\langle e^{i\mathbf{k}\cdot\mathbf{r}}|\tilde{M}_J^{\mathbf{k}}\rangle + v'_{IJ}(\mathbf{k})\,. \tag{36}$$

The long-wavelength limit of the non-divergent second term replaces the matrix $v_{IJ}(\mathbf{0})$ in Eq. (19), which allows to perform the $\mathbf{k}$ summation numerically. The divergent first term (since the MPB contains the constant function, this term is given exactly, and we may calculate with $e^{i\mathbf{k}\cdot\mathbf{r}}$) gives rise to a contribution

$$V_{\mathrm{x},nn'}^{\mathrm{NL},\sigma}(\mathbf{q})\Big|_{\mathrm{div}} = -\frac{1}{2\pi^2}\left(\sum_{n''}^{\mathrm{occ.}}\int_{\mathrm{BZ}}\langle\varphi^{\sigma}_{n\mathbf{q}}|\varphi^{\sigma}_{n''\mathbf{q}-\mathbf{k}}e^{i\mathbf{k}\cdot\mathbf{r}}\rangle\frac{1}{k^2}\langle e^{i\mathbf{k}\cdot\mathbf{r}}\varphi^{\sigma}_{n''\mathbf{q}-\mathbf{k}}|\varphi^{\sigma}_{n'\mathbf{q}}\rangle d^3k - \mathrm{d.c.}\right), \tag{37}$$

where d.c. is a double-counting correction to be defined later. For the important region close to $\mathbf{k}=\mathbf{0}$ we can replace $\langle\cdot|\cdot\rangle$ by $\delta_{nn''}$ and $\delta_{n'n''}$, respectively, and leave out higher-order corrections [39] for simplicity. Even though this simplifies the integral to $\int_{\mathrm{BZ}} d^3k/k^2$ the $\mathbf{k}$ integration can still not be done analytically because the integration region is bound by the complicated BZ boundary. Therefore, we employ a method that is similar to the one proposed by Massidda *et*

al. in Ref. 40. We replace $1/k^2$ by the function

$$F(\mathbf{k}) \;=\; \sum_{\mathbf{G}} \frac{e^{-\beta|\mathbf{k}+\mathbf{G}|^2}}{|\mathbf{k}+\mathbf{G}|^2}\,, \tag{38}$$

which is defined in the whole reciprocal space. It contains as many terms as the crystal contains BZs. Therefore, we can write

$$V^{\mathrm{NL},\sigma}_{\mathrm{x},nn'}(\mathbf{q})\Big|_{\mathrm{div}} = -\delta_{nn'} f^{\sigma}_{n\mathbf{q}} \left(\frac{1}{2\pi^2} \int \frac{e^{-\beta|\mathbf{k}|^2}}{k^2} d^3k - \frac{1}{N_{\mathbf{k}}\Omega} \sum_{k\neq 0} \frac{e^{-\beta|\mathbf{k}|^2}}{k^2} \right), \tag{39}$$

where the parameter $\beta > 0$ ensures that the integral over the whole reciprocal space is finite and Ω is the unit-cell volume. In contrast to Massidda *et al.,* we choose this parameter as small as possible so that the function remains close to $1/k^2$. (This also ensures that calculations of the same system with different choices of the unit cell yield identical values.) Here, we have defined the double-counting term. $N_{\mathbf{k}}$ denotes the number of $\mathbf{k}$ points and $f^{\sigma}_{n\mathbf{k}}$ is the occupation number. The contribution of large $\mathbf{k}$ vectors tend to cancel in the difference of Eq. (39) so that we may introduce a reciprocal cutoff radius k_0 and finally obtain

$$V^{\mathrm{NL},\sigma}_{\mathrm{x},nn'}(\mathbf{q})\Big|_{\mathrm{div}} = -\delta_{nn'} f^{\sigma}_{n\mathbf{q}} \left(\frac{1}{\sqrt{\pi\beta}} \operatorname{erf}\left(\sqrt{\beta}k_0\right) - \frac{1}{N_{\mathbf{k}}\Omega} \sum_{0<k\leq k_0} \frac{e^{-\beta|\mathbf{k}|^2}}{k^2} \right). \tag{40}$$

By setting $e^{-\beta k_0^2} = \beta$, we are left with β as the only convergence parameter, which just has to be chosen small enough; $\beta = 0.005$ is a good choice.

Fig. 1 demonstrates the performance of the Γ-point treatment for the exchange energy $E^{\mathrm{NL}}_{\mathrm{x}} = 2\sum_{n\mathbf{q}}^{\mathrm{occ.}} V^{\mathrm{NL}}_{\mathrm{x},nn}(\mathbf{q})$ of NaCl. While the contributions from the divergent term, Eq. (40), and the remainder separately converge poorly with respect to the $\mathbf{k}$-point sampling, their sum nearly look constant on the energy scale of the diagram. The $\mathbf{k}$-point convergence can be improved further by taking corrections at $\mathbf{k} = \mathbf{0}$ into account that arise from multiplying $1/k^2$ with second-order terms of $\langle\cdot|\cdot\rangle\langle\cdot|\cdot\rangle$ [39].

We note that the Fourier transform in Eq. (24) diverges as $1/k^2$ in the limit $\mathbf{k} \to \mathbf{0}$. The same divergence is found for the bare Coulomb potential [39, 61], such that the $1/k^2$ terms cancel in the difference. The remainder is finite and is given by

$$\lim_{\mathbf{k}\to\mathbf{0}} \frac{4\pi}{k^2} \left(1 - e^{-k^2/(4\kappa^2)}\right) = \frac{\pi}{\kappa^2}\,. \tag{41}$$

In Fig. 2, we show that this nondivergent behavior of the short-range interaction gives rise to a favorable $\mathbf{k}$-point convergence, here for the example of the silicon band gap. Within HSE the values converge nearly as fast as in PBE, whereas the PBE0 functional requires larger $\mathbf{k}$-point meshes. This was already observed in Ref. 68.

In the calculation of the dielectric matrix [Eq. (23)], we multiply the polarization function with the Coulomb matrix, and in the limit $\mathbf{k} \to \mathbf{0}$ we must again deal with the k^{-2} Coulomb divergence. Its treatment is simplified by the basis transformation $\{M^{\mathbf{k}}_I(\mathbf{r})\} \to \{E^{\mathbf{k}}_\mu(\mathbf{r})\}$ introduced above because this transformation confines the divergence of the Coulomb matrix to a single eigenvalue $v_1(\mathbf{k}) \sim 4\pi/k^2$ [61]. The corresponding eigenfunction $E^{\mathbf{k}}_1(\mathbf{r}) \sim e^{i\mathbf{k}\cdot\mathbf{r}}/\sqrt{V}$ is known analytically. The situation is then analogous to a pure plane-wave basis, but we emphasize that,

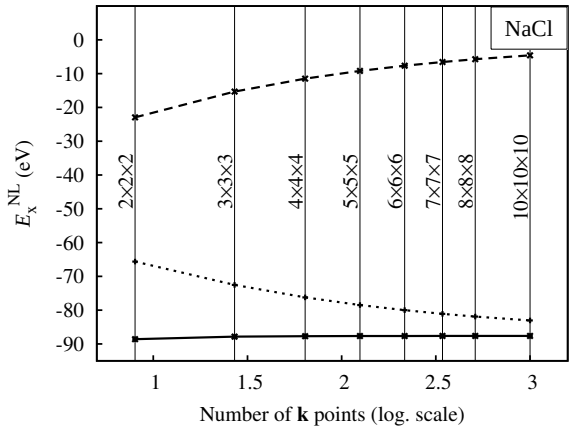

Figure 1: Exchange energy as a function of the **k**-point mesh for NaCl. The dashed and dotted curves correspond to the contributions of the divergent term Eq. (40) and the numerical sum, respectively. Their sum shown by the solid curve converges very quickly. [39]

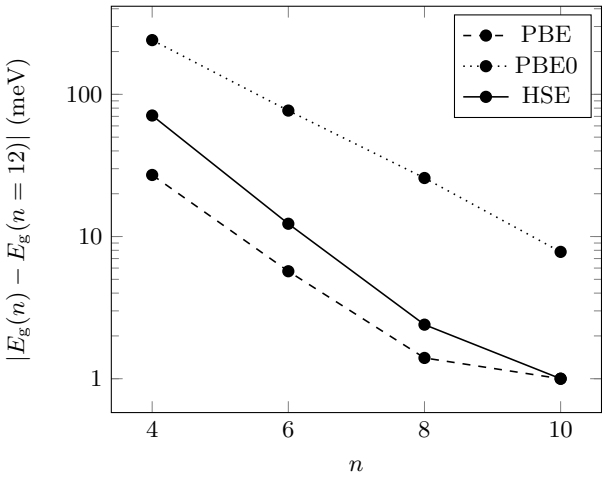

Figure 2: Convergence of the silicon band gap for the functionals PBE (dashed), PBE0 (dotted), and HSE (solid) with respect to the **k**-point mesh ($n \times n \times n$). [69]

since $\{E^{\mathbf{k}}_{\mu}(\mathbf{r})\}$ has been transformed from the MPB, we still retain the all-electron description without a projection onto plane waves. Using $\mathbf{k}\cdot\mathbf{p}$ perturbation theory, we can show that the head ($\mu=\nu=1$) and wing elements ($\mu\neq\nu=1$ and $1=\mu\neq\nu$) of the polarization matrix $P_{\mu\nu}(\mathbf{k},\omega)$ [Eq. (33)] behave as k^2 and k, respectively, so that the resulting dielectric matrix $\varepsilon(\mathbf{k},\omega)$ remains finite albeit angular dependent at $\mathbf{k}=\mathbf{0}$ [70, 71]. This form of the dielectric matrix gives rise to angular and energy dependent head and wing elements that diverge as k^{-2} and k^{-1}, respectively, in the $\mathbf{k}\to\mathbf{0}$ limit of the screened interaction $W_{\mu\nu}(\mathbf{k},\omega)$ [Eq. (22)], which consists of a constant and an angular dependent part. Without a derivation we only give the final expression here

$$W_{\mu\nu}(\mathbf{k},i\omega) \sim \begin{pmatrix} 0 & 0 & \cdots & 0 \\ 0 & \tilde{W}_{22}(\omega) & \cdots & \tilde{W}_{2n}(\omega) \\ \vdots & \vdots & \ddots & \vdots \\ 0 & \tilde{W}_{n2}(\omega) & \cdots & \tilde{W}_{nn}(\omega) \end{pmatrix} \tag{42}$$
$$+\frac{1}{\hat{\mathbf{k}}^{\mathrm{T}}\mathbf{L}(\omega)\hat{\mathbf{k}}} \begin{pmatrix} 4\pi/k^2 & \hat{\mathbf{k}}^{\mathrm{T}}\mathbf{w}_2(\omega)/k & \cdots & \hat{\mathbf{k}}^{\mathrm{T}}\mathbf{w}_n(\omega)/k \\ \hat{\mathbf{k}}^{\mathrm{T}}\mathbf{w}_2^*(\omega)/k & \left|\hat{\mathbf{k}}^{\mathrm{T}}\mathbf{w}_2(\omega)\right|^2 & \cdots & \left[\hat{\mathbf{k}}^{\mathrm{T}}\mathbf{w}_2^*(\omega)\right]\left[\hat{\mathbf{k}}^{\mathrm{T}}\mathbf{w}_n(\omega)\right] \\ \vdots & \vdots & \ddots & \vdots \\ \hat{\mathbf{k}}^{\mathrm{T}}\mathbf{w}_n^*(\omega)/k & \left[\hat{\mathbf{k}}^{\mathrm{T}}\mathbf{w}_n^*(\omega)\right]\left[\hat{\mathbf{k}}^{\mathrm{T}}\mathbf{w}_2(\omega)\right] & \cdots & \left|\hat{\mathbf{k}}^{\mathrm{T}}\mathbf{w}_n(\omega)\right|^2 \end{pmatrix},$$

were $\mathbf{L}(\omega)$ is a 3×3 matrix, $\mathbf{w}_{\mu}(\omega)$ are three-dimensional vectors, and $\hat{\mathbf{k}}$ is a unit Bloch vector denoting the direction from which the limit $\mathbf{k}\to\mathbf{0}$ is taken. The appearance of the divergent wing elements and the angular dependence makes the evaluation of the correlation self-energy more complicated than in the case of the exchange self-energy. For the angular dependence, we choose an expansion in terms of spherical harmonics. (This expansion contains infinitely many terms if $\mathbf{L}(\omega)$ is not a multiple of the unit matrix, but the expansion usually converges rapidly. Furthermore, it can be calculated analytically by solving a system of linear equations.) Once the expansion is found, angular integration over the point $\mathbf{k}=\mathbf{0}$ is straightforward, $\int Y_{lm}(\hat{\mathbf{k}})d\hat{\mathbf{k}}=\delta_{l0}$. The numerically most important contribution derives from the k^{-2} divergence, which is treated with the same strategy as in the case of the exchange self-energy. For further details we refer the reader to our original publication [54].

Let us now turn to the case of a metallic system, where in addition to the interband transitions with $n\neq n'$ there is a contribution from intraband transitions across the Fermi surface. These transitions occur within one electron band, i.e., $n=n'$, and give rise to a contribution to the head element of the polarization function, the so-called Drude term [72]

$$P^{\mathrm{D}}_{11}(\mathbf{k},i\omega) \sim -\frac{k^2}{4\pi}\frac{\omega^2_{\mathrm{pl}}}{\omega(\omega+i\eta)}\,, \tag{43}$$

where ω_{pl} is the plasma frequency obtained by an integration over the Fermi surface. The main contribution to the screened interaction is given by the *bare* Drude term

$$W^{\mathrm{c,D}}_{11}(\mathbf{k},i\omega) \sim -\frac{4\pi}{k^2}\frac{\omega^2_{\mathrm{pl}}}{\omega^2+\omega^2_{\mathrm{p}}}\,. \tag{44}$$

This expression can be convoluted with the Green function in Eq. (28) analytically.

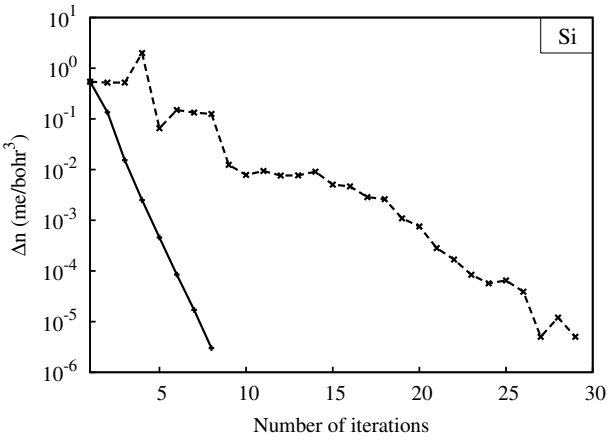

Figure 3: Convergence behavior of the electron density for Si in a self-consistent-field cycle. The solid and dashed curves correspond to calculations with and without the nested density convergence scheme. [39]

Nested density convergence For hybrid functional calculations one must solve the one-particle equation [Eq. (16)] self-consistently, meaning that the input density that generates the local and nonlocal potential coincides with the output density formed by the wave functions that are solutions of the one-particle equation. It is known that already in conventional DFT calculations with purely local functionals a density mixing scheme must be employed that combines the current density with several previous densities, as for example in the standard simple-mixing and Broyden-mixing schemes [73, 74]. However, in addition to the local effective potential, Eq. (16) contains a nonlocal potential that depends on the density matrix, for which no simple mixing procedure is available. Indeed, a standard density-only mixing (without a mixing of the density matrix) leads to poor convergence: 27 iterations for Si, as illustrated in Fig. 3, and more than 200 iterations for $SrTiO_3$ are necessary. Rather than constructing a complicated mixing scheme for the density matrix, we choose a pragmatic approach: The self-consistency cycle is divided into an outer loop, where the density and the density matrix is updated, and an inner loop, where only the density is converged while the density matrix is kept fixed. With this nested iterative procedure the *outer* loop converges after eight steps for Si, see Fig. 3, and after only twelve steps for $SrTiO_3$. One iteration of the *inner* loop lasts only 1.0 s for Si and 8.3 s for $SrTiO_3$ on a single Intel Xeon X5355 at 2.66 GHz (Cache 4 MB) using a 4×4×4 **k**-point set. This is small compared to the cost for the construction of the nonlocal potential in the *outer* loop, which takes 11.9 s for Si and 573.1 s for $SrTiO_3$.

4 Results

We have implemented the hybrid functionals PBE0 and HSE in the FLEUR program package [75] and the *GW* approximation as the SPEX code [54]. In addition to the radial functions $u_{lp}^{a\sigma}(r)$ with $p = 0, 1$, corresponding to the solution of the radial Kohn-Sham equation with the local PBE potential and its energy derivative, respectively, we employ local orbitals with $p \geq 2$ to describe semi-core states as well as high-lying conduction states if necessary [76, 77]. In the

hybrid-functional calculations presented here, the core states are taken from a preceding PBE calculation and kept fixed during the self-consistent-field cycle.

In the following sections we discuss the convergence of the MPB (Sec. 4.1), results for simple materials, comparison to other codes, and timings (Sec. 4.2), as well as results for GdN (Sec. 4.3), and ZnO (Sec. 4.4).

4.1 Test calculations

In this section we analyze the performance of the MPB, in particular its convergence behavior with respect to the parameters $L_{\max}$, $G'_{\max}$, and $n_{\max}$ for single-particle excitation energies and total energy differences. We only show results for the PBE0 functional. A similar performance of the MPB is found for the HSE functional and the *GW* approximation. Figures 4(a) and (b) show excitation energies of Si ($\Gamma_{25'v} \to \Gamma_{15c}$ and $\Gamma_{25'v} \to \mathrm{X}_{1c}$) and $SrTiO_3$ ($\Gamma_{15v} \to \Gamma_{25'c}$ and $\mathrm{R}_{15'v} \to \Gamma_{25'c}$) obtained from the self-consistent PBE0 solution as functions of the MPB parameters. The diagrams show that the convergence of these transition energies to within 0.01 eV is achieved for $G'_{\max} = 2.0\,\mathrm{bohr}^{-1}$ and $G'_{\max} = 2.7\,\mathrm{bohr}^{-1}$ for Si and $SrTiO_3$, respectively. This is not only below the exact limit $G'_{\max} = 2G_{\max}$ for the wave-function products, it is even below the reciprocal cutoff radius $G_{\max}$ for the wave functions themselves ($G_{\max} = 3.6\,\mathrm{bohr}^{-1}$ for Si and $G_{\max} = 4.3\,\mathrm{bohr}^{-1}$ for $SrTiO_3$). Similarly, we find an angular-momentum cutoff value of $L_{\max} = 4$ to be sufficient, while a proper matching of the wave functions at the MT boundaries requires a much larger value of $l_{\max} = 8$. Furthermore, the figures show that the number of bands, in which the exchange potential is represented, can be cut at $n_{\max} = 100$ for Si and at $n_{\max} = 250$ for $SrTiO_3$, corresponding to about 50 bands per atom.

Figure 4(c) shows that the total energy difference between the diamond and wurtzite structure of Si converges even faster than the transition energies above. With a reciprocal cutoff radius of $G'_{\max} = 2.25\,\mathrm{bohr}^{-1}$, an angular-momentum cutoff of $L_{\max} = 4$, and 20 bands per atom we achieve an accuracy of 1 meV, which is well below the error resulting from the BZ discretization. With the finer $8\times8\times8$ **k**-point mesh, the total-energy difference is converged to within 2 meV and amounts to 112 meV, i.e., the diamond structure is lower in energy than the wurtzite structure. This is very close to the value of 92 meV obtained with the PBE functional.

In summary, we find that $G'_{\max}$ can be chosen universally smaller than $G_{\max}$, $G'_{\max} = 0.75\,G_{\max}$ as a rule of thumb, while the cutoff parameter $L_{\max}$ is more material-specific. If the material contains occupied d or f electrons, we have to use $L_{\max} = 5$ or even $L_{\max} = 6$. Also, the band cutoff $n_{\max}$ is material-specific.

In *GW* calculations we also have to deal with a band cutoff $n_{\max}$ that determines the number of bands that are taken into account in the calculation of the polarization function (2) and the correlation self-energy (10), because the number of available eigenstates is limited by the size of the basis set. Furthermore, the computational cost depends strongly on the number of unoccupied states. It is well known that a proper convergence of the *GW* quasiparticle energies requires very many unoccupied states [78, 79, 80, 81]. While for $SrTiO_3$, a relatively modest number of 200 states is sufficient, the band gaps of Si, in particular, the indirect one, are more difficult to converge. We will see in Sec. 4.4 that ZnO is an extreme case in this respect. A

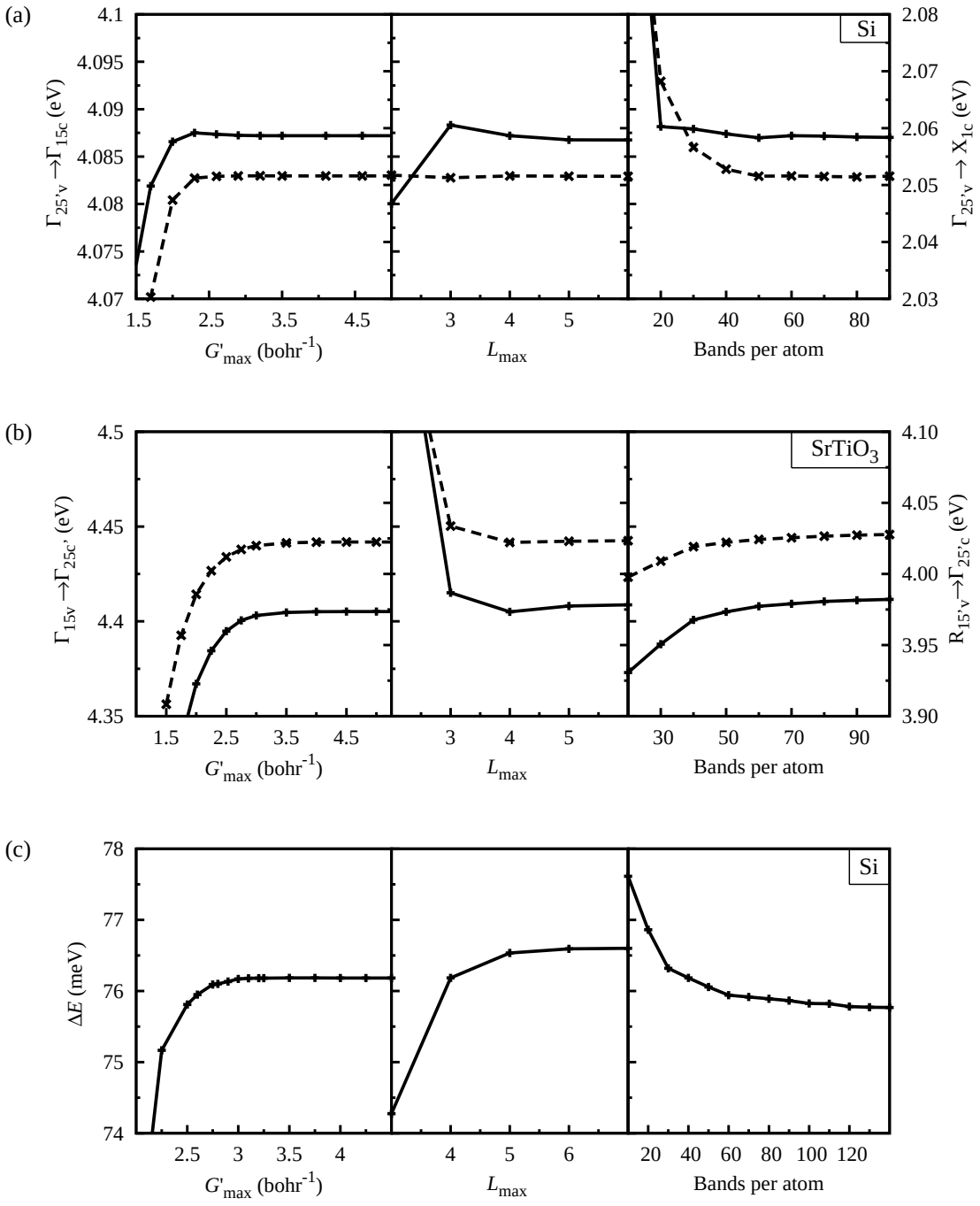

Figure 4: Convergence of single-particle transition energies for (a) Si and (b) $SrTiO_3$ with respect to the MPB parameters (solid line: left scale, dashed line: right scale). (c) Convergence of the total energy difference between the diamond and wurtzite phase of Si with respect to the same parameters. For these test calculations we have employed a 4×4×4 **k**-point set. See the tables for fully converged results and the text for details. [39]

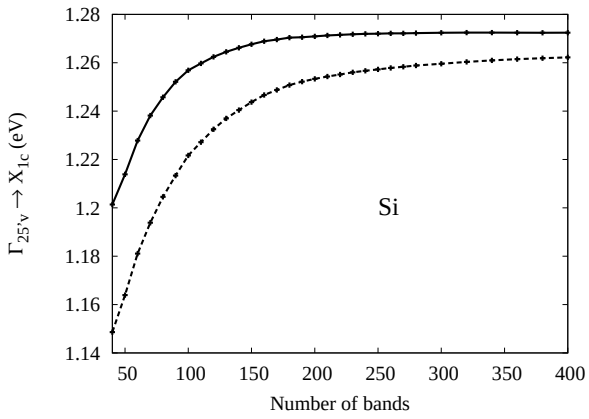

Figure 5: Convergence of the $\Gamma_{25'v} \rightarrow X_{1c}$ gap of Si with respect to the number of bands used in the construction of the polarization function as well as the self-energy (solid line). The dashed line shows the effect of the extrapolar correction. [54]

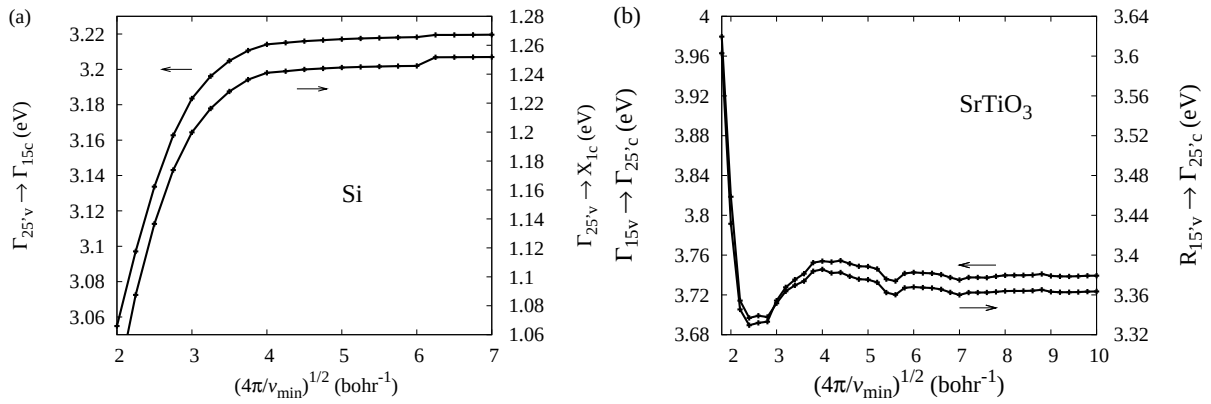

Figure 6: Convergence of single-particle transition energies of (a) Si and (b) $SrTiO_3$ as a function of $\sqrt{4\pi/v_{\min}}$. [54]

possible solution to this problem is the extrapolar correction introduced by Bruneval and Gonze [82], in which the states not explicitly taken into account (i.e., $n' > n_{\max}$) are placed on a fixed energy that is taken as a parameter. In this way, the frequency-dependent term becomes state independent, which allows to apply the completeness relation $\sum_{n'>n_{\max}} |n'\rangle\langle n'| = 1 - \sum_{n' \leq n_{\max}} |n'\rangle\langle n'|$ to eliminate the states $n' > n_{\max}$. Figure 5 shows the normal convergence with respect to the number of states and also the improvement from the extrapolar approximation. However, we have found mixed success with this method. In some cases it works very well, in other cases it is less successful. Another drawback is that the determination of the additional fixed energy requires further test calculations. Therefore, all other results presented here were obtained with the conventional summation. We note that the LAPW basis is a relatively small and accurate basis for the occupied states. In order to get enough unoccupied states for *GW* calculations it is therefore often necessary to extend the LAPW basis by increasing the reciprocal cutoff radius $G_{\max}$ and introducing additional local orbitals.

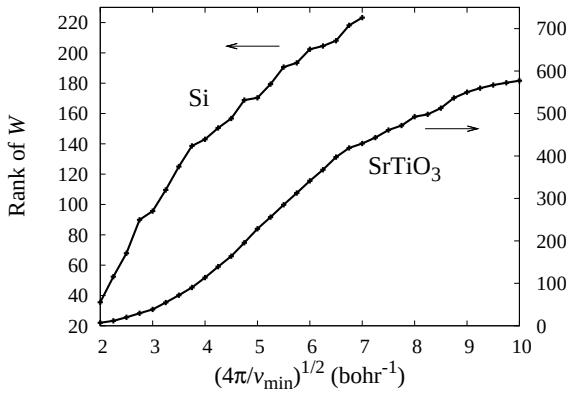

Figure 7: Rank of the matrix W for the screened interaction, i.e., the number of basis functions after the optimization, for Si and $SrTiO_3$ as a function of $\sqrt{4\pi/v_{\min}}$. [54]

Geometry	Atoms	**k** mesh	Symmetry	$v_{\min}$	CPU time
1×1×1	2	4×4×4	No	—	5 min 52 s
			Only IS	—	3 min 34 s
			Only IBZ	—	30 s
			Yes	—	11 s
			Yes	0.65	5 s
2×2×2	16	2×2×2	Yes	0.65	14 min 15 s
4×4×4	128	1×1×1	Yes	0.65	34 h 11 min

Table 1: Computational time for the calculation of quasiparticle shifts of diamond in the conventional (1×1×1) and supercell (2×2×2 and 4×4×4) geometries. For the former we also show corresponding timings without use of symmetry ("No") and with restricted use ("Only IS" and "Only IBZ") as well as the effect of the MPB optimization with a threshold value $v_{\min}$. [54]

The computationally most expensive step in GW calculations is the evaluation of the correlation part of the self-energy, which also involves the calculation of the screened interaction W. This step can be accelerated by introducing a threshold value $v_{\min}$ for the Coulomb eigenvalues as explained in Sec. 3.4. In Fig. 6, we show the convergence of the single-particle transition energies of Si and $SrTiO_3$ with respect to $\sqrt{4\pi/v_{\min}}$. The latter quantity is chosen to relate the threshold value to a reciprocal cutoff radius such as $G_{\max}$. (In a pure plane-wave representation the minimum Coulomb eigenvalue would be $v_{\min} = 4\pi/G_{\max}^2$.) We observe that the energies are converged to within 0.01 eV at around $\sqrt{4\pi/v_{\min}} = 3.5\,\mathrm{bohr}^{-1}$ or $v_{\min} = 1.9\,\mathrm{ha}$. This reduces the rank of the matrix W (see Fig. 7) from 392 (the full MPB) to around 75 and the computation time from 140 to 42s on an Intel Xeon (2.66 GHz, 4 MB cache) work station. (The step-like feature at around 5.3 bohr^{-1} is caused by a sudden increase of the basis set, because there are several Coulomb eigenfunctions with the same eigenvalue of $4\pi/5.3^2$ ha.) A similar improvement is found for $SrTiO_3$.

In order to test the efficiency of the code, we show the computational time for calculating quasiparticle shifts for diamond in the conventional unit cell (1×1×1) containing two atoms as

well as in 2×2×2 and 4×4×4 supercell geometries containing 16 and 128 atoms, respectively. The BZ is sampled with **k**-point sets having the same **k**-point density for all calculations, i.e., a 4×4×4, 2×2×2, and 1×1×1 set, respectively. The computation times on a single CPU are given in Table 1. While the *GW* calculation takes only 5 s for the conventional unit cell, even the treatment of supercells containing 16 and 128 atoms only consumes affordable 0.24 and 34.2 h of computation time, respectively. We also demonstrate the efficiency gain achieved by exploiting the symmetry and by using a threshold parameter $v_{\min}$. The different entries are as follows: "Only IS" refers to the symmetrization of the MPB due to inversion symmetry, which gives rise to real-valued quantities; "Only IBZ", only the IBZ for **q**, but not the EIBZ(**q**) for **k** is used; "Yes", spatial and time-reversal symmetries are fully exploited; the next row shows the effect of introducing a Coulomb eigenvalue threshold $v_{\min}$. With this last step the computation time has been reduced to only 5 s, gaining an overall factor of 70 with respect to the first row.

4.2 Simple materials

In this section we present HSE, PBE0, and *GW* calculations for a prototypical set of semiconductors and insulators and compare the results with previous works from the literature [68, 52, 34, 83]. All calculations are performed at the experimental lattice constant taken from Ref. 84 with an 8×8×8 **k**-point mesh, except for the PBE0 calculations, which are performed with a 12×12×12 mesh. We focus in particular on direct and indirect band transitions. These are calculated as the energy differences of the highest occupied and the lowest unoccupied eigenstates at the corresponding points in the BZ.

In Table 2, our PBE0 and HSE results for the $\Gamma \rightarrow \Gamma$, $\Gamma \rightarrow$ X, and $\Gamma \rightarrow$ L transition energies are compared with those obtained by the projector-augmented-wave (PAW) method [68] and experimental data. Overall, we observe excellent agreement between the calculated values, except for the PBE0 values for systems with wider band gaps, where we find larger discrepancies. This is a basis-set effect caused by the fact that only two radial functions per lm channel have been used for each MT sphere. For the PBE and HSE calculations, which were performed later, we have overcome this slight inaccuracy by including local orbitals (in addition to those that are already in use for the semicore states). In all cases the admixture of the nonlocal exchange potential leads to an increase of the transition energies in such a way that they come close to the measured values. For the materials shown in Table 2 there is still a slight underestimation of the band gaps for large-gap insulators in PBE0 and HSE as well as an overestimation for semiconductors in PBE0.

Although the hybrid functionals thus seem to give an overall better description of excitation energies than conventional DFT functionals such as LDA or PBE, one should not forget that the eigenvalues obtained within a (generalized) Kohn-Sham formalism are merely mathematical Lagrangian parameters without a direct physical meaning. A theoretically better founded theory for excitation (or quasiparticle) energies is provided by the *GW* approximation for the electronic self-energy. Of course, one could interpret the hybrid functionals as approximate self-energies and, thus, the KS eigenvalues as quasiparticle energies. However, the definition of the hybrid functionals is somewhat arbitrary: the mixing parameter $a = 0.25$ is estimated, the parameter κ of the decomposition [Eq. (14)] is fitted to experiment, the mathematical decomposition itself is

		This work [39, 69]			PAW [68]			Expt.
		PBE	PBE0	HSE	PBE	PBE0	HSE	
GaAs	$\Gamma \rightarrow \Gamma$	0.54	2.02	1.43	0.56	2.01	1.45	1.52 [85], 1.63 [86]
	$\Gamma \rightarrow$ X	1.47	2.69	2.06	1.46	2.67	2.02	1.90 [85], 2.01, 2.18 [86]
	$\Gamma \rightarrow$ L	1.01	2.38	1.78	1.02	2.37	1.76	1.74 [85], 1.84, 1.85 [86]
Si	$\Gamma \rightarrow \Gamma$	2.56	3.96	3.32	2.57	3.97	3.32	3.05 [87], 3.35 [88], 3.4 [86]
	$\Gamma \rightarrow$ X	0.71	1.93	1.29	0.71	1.93	1.29	1.13 [88], 1.25 [87]
	$\Gamma \rightarrow$ L	1.54	2.87	2.24	1.54	2.88	2.24	2.06 [89], 2.40 [86]
C	$\Gamma \rightarrow \Gamma$	5.60	7.74	6.98	5.59	7.69	6.97	7.3 [85]
	$\Gamma \rightarrow$ X	4.75	6.69	5.90	4.76	6.66	5.91	—
	$\Gamma \rightarrow$ L	8.46	10.88	10.02	8.46	10.77	10.02	—
MgO	$\Gamma \rightarrow \Gamma$	4.77	7.31	6.49	4.75	7.24	6.50	7.7 [90]
	$\Gamma \rightarrow$ X	9.14	11.63	10.86	9.15	11.67	10.92	—
	$\Gamma \rightarrow$ L	7.93	10.51	9.69	7.91	10.38	9.64	—
NaCl	$\Gamma \rightarrow \Gamma$	5.20	7.13	6.57	5.20	7.26	6.55	8.5 [91]
	$\Gamma \rightarrow$ X	7.58	9.59	9.05	7.60	9.66	8.95	—
	$\Gamma \rightarrow$ L	7.30	9.33	8.66	7.32	9.41	8.67	—
Ar	$\Gamma \rightarrow \Gamma$	8.70	11.15	10.36	8.68	11.09	10.34	14.2 [92]

Table 2: Kohn-Sham transition energies in eV obtained with the functionals PBE, PBE0, and HSE at experimental lattice constants compared with values from PAW calculations and experiment. An 8×8×8 (12×12×12) **k**-point mesh was employed for the PBE and HSE (PBE0) values. The deviation of the PBE0 values from the PAW ones for the large band-gap insulators is a basis-set effect (see text). (Compiled from Refs. 39 and 69.)

	This work [54]		LMTO [29]		PAW [83]		Expt.
	LDA	*GW*	LDA	*GW*	LDA	*GW*	
Ge	0.02	0.75	–0.08	0.57	—	—	0.74 [93]
Si	0.62	1.11	0.46	0.90	0.62	1.12	1.17 [86]
GaAs	0.29	1.31	0.33	1.31	0.49	1.30	1.63 [86]
CdS	1.17	2.18	—	—	1.14	2.06	2.58 [94]
GaN	1.67	2.83	1.81	3.03	1.62	2.80	3.27 [95]
$SrTiO_3$	1.80	3.36	—	—	—	—	3.25 [96]
$BaTiO_3$	2.18	3.18	—	—	—	—	3.3 [97]
CaSe	2.04	3.63	—	—	—	—	3.85 [98]
C	4.15	5.62	4.11	5.49	4.12	5.50	5.48 [86]
BN	4.35	6.20	—	—	4.45	6.10	5.97 [99]
MgO	4.64	7.17	4.85	6.77	4.76	7.25	7.83 [100]
NaCl	4.90	7.53	—	—	—	—	8.5 [101]

Table 3: Fundamental *GW* band gaps for a variety of semiconductors and insulators compared with experimental and theoretical values from the literature. We also indicate the LDA eigenvalue gaps. All values are in electron volts. [54]

non-unique, the choice of the local xc potential is arbitrary, and so on. One should also mention that the meaning of the local xc potential is different from that of a self-energy. Furthermore, retardation effects in the screening process are completely neglected.

In contrast, quasiparticle energies calculated with the *GW* self-energy have the clear physical interpretation of being excitation energies of the many-body system. Within this theory retardation and lifetime effects are taken into account without resorting to adjustable parameters. In Table 3, we list the fundamental LDA and *GW* band gaps for a variety of semiconductors and insulators, together with experimental and other theoretical values for comparison. The latter are calculated with the LMTO (Ref. 29) and the PAW method (Ref. 83). Additional local orbitals are included to improve the description of high-lying unoccupied states (also cmp. Sec. 4.4). Local orbitals are also used to describe the shell below the valence band, e.g., the cation $2s$ and $2p$ states of MgO and NaCl. Overall our LDA and *GW* values agree very well with those of Ref. 83, but somewhat less so with the older Ref. 29. (We note that there are many more convergence parameters in *GW* calculations as there are in PBE0 or HSE calculations, which explains the larger deviations here compared with Table 2.) As expected, the *GW* self-energy corrects the underestimation of LDA in such a way that the results come very close to the measured values. When comparing with Table 2, we see that the *GW* values are at least as close to experiment as the hybrid-functional results and even better for the large-gap insulators.

However, there is still a slight underestimation in most cases. It has been suggested that a self-consistent scheme could improve the *GW* values further [83, 102]. The starting point is then optimized in such a way that the resulting one-particle orbitals are as close as possible to the quasiparticle wave functions; in particular, closer than those from standard local or semilocal functionals such as LDA. In this way, the first-order perturbative correction [Eq. (8)], where the quasiparticle wave functions are approximated by the one-particle orbitals, is better justified.

	This work [69]		PAW [68]	Gaussian [52]	Expt. [84]
Functional	PBE	HSE	HSE	HSE	—
GaAs	5.743	5.660	5.687	5.710	5.648
Si	5.472	5.441	5.435	5.451	5.430
C	3.571	3.549	3.549	3.557	3.567
MgO	4.265	4.217	4.210	4.222	4.207
NaCl	5.703	5.627	5.659	5.645	5.595

Table 4: Optimized lattice constants in Å obtained with the PBE and the HSE functional. An $8 \times 8 \times 8$ **k**-point mesh was employed. Results are compared to experimental results and theoretical calculations. [69]

	This work [69]		PAW [68]	Expt. [84]
Functional	PBE	HSE	HSE	—
GaAs	64.5	79.2	70.9	75.6
Si	88.9	98.0	97.7	99.2
C	433	467	467	443
MgO	153	177	169	165
NaCl	21.3	28.8	24.5	26.6

Table 5: Bulk moduli in GPa obtained with the PBE and the HSE functional. An $8 \times 8 \times 8$ **k**-point mesh was employed. Results are compared to experimental results and calculations using the HSE functional within a PAW method. [69]

However, self-consistent *GW* calculations are computationally very expensive. When compared with the electronic self-energy, the most obvious source of errors in LDA or GGA is the missing self-interaction correction, which influences the shape of the KS wave functions. Therefore, better results might alternatively be obtained if one uses a functional that treats electronic exchange more accurately, e.g., the hybrid functionals [103]. These combined approaches go beyond the scope of the present article. Nevertheless, we note that the numerical procedure for the *GW* approximation presented here is independent of the starting point and could also be applied within a self-consistent scheme or to functionals containing an exact exchange term.

The main virtue of DFT is, of course, its ability to yield accurate total energies rather than the excitation energies discussed above. In Tables 4 and 5 we present equilibrium lattice constants and bulk moduli derived from HSE total energies for different lattice constants and compare the results with other implementations based on plane-wave (PAW) [68] and Gaussian basis sets [52]. The results of all three methods agree very well. Except for diamond, the HSE functional yields lattice constants and bulk moduli in much better agreement with experiment than the semilocal PBE functional, which tends to overestimate the former and underestimate the latter.

	HSE		LSDA+U			B3LYP	Expt.
	This work		([2])	([3])	([4])	([5])	
Latt. const. (Å)	(4.988)	4.967	4.92	5.08	(4.988)	5.05	4.988 [120]
Bulk mod. (GPa)		164		150		159	192 [121]
Mag. mom. (μ_B)	6.99[1]	6.99		6.93[1]		7.0	6.88 [104]
$E_g^{dir.}$(X) (FM)	0.90[1]	0.85	–0.16		0.91[1]	1.18	0.90 [122]
$E_g^{dir.}$(X) (PM)	1.17[1]	1.11	0.10	0.98[1]	1.30[1]	1.77	1.31 [122]
$E_g^{indir.}$($\Gamma \rightarrow$X) (FM)	0.01[1]	–0.06	–0.45	0.14[1]	0.43[1]	0.72	
$E_g^{indir.}$($\Gamma \rightarrow$X) (PM)	0.90[1]	0.85	–0.13	0.69[1]	0.98[1]	1.47	
$\epsilon_{4f}^{\uparrow} - \epsilon_F$	–6.00[1]	–6.00	–7.8	–8.1[1]		–6.3	–7.8 [105]
$\epsilon_{4f}^{\uparrow} - \epsilon_F$	6.05[1]	6.05	6.6	5.0[1]	4.8[1]	5.5	5.5–6.1 [6]

[1] At the experimental lattice constant.

[2] [108, 109, 110]; U optimized for Gd bulk [123].

[3] [118]; U chosen to reproduce the experimental direct gap of paramagnetic GdN [124].

[4] [122]; U chosen to reproduce the experimental direct gap of paramagnetic GdN.

[5] [119]; insulating solution.

[6] [125]; measured for GdX (X =P, As, Sb, and Bi).

Table 6: Comparison of our HSE results [69] for GdN with those from LSDA+U and experiment. For the calculation of the ferro- and paramagnetic states (FM, $T < T_C$; PM, $T > T_C$) see text. Energies are given in eV. The calculations were performed with a 8×8×8 **k**-point set. [69]

4.3 GdN – a HSE study

In this section we present results for the ground-state properties and the band structure of GdN calculated with the HSE functional. Gadolinium nitride (GdN) is widely studied owing to the ferromagnetic order, large magnetic moment of 6.88 μ_B per Gd atom [104] and its large magnetoresistive effect [105], which makes the material interesting for technological applications. The mechanism of the ferromagnetic order is still under debate. Various types are being discussed, such as carrier mediated [106, 107] and superexchange mechanisms [108, 109, 110]. Another point of debate are the electronic properties. It was experimentally demonstrated to be a low carrier semimetal in single crystals [111] and insulating in thin films [112]. There are also several recent reports of thin films of GdN having a degenerately doped semiconducting [113, 114, 115] or a metallic ground state [115] based on the resistivity data measured at low temperatures. Results from LSDA+U calculations are inconclusive. While the linearized muffin-tin orbital (LMTO) approach yields a narrow-gap semiconductor as ground state [116, 117, 118, 106], one obtains a transition from a half-metallic to a semiconducting ground state under strain within the FLAPW method [108, 109, 110]. Two different solutions close in energy were obtained in an investigation using the hybrid functional B3LYP [119]. Both solutions were half-metallic, one in the majority spin channel, the other one in the minority spin channel.

GdN crystallizes in the rocksalt structure with a room-temperature lattice constant of a_{GdN} = 4.988 Å[121]. Half-filling of the Gd 4f states gives rise to ferromagnetic ordering in the electronic ground state at 0 K. The rest of the valence and conduction bands are formed by the N 2s and

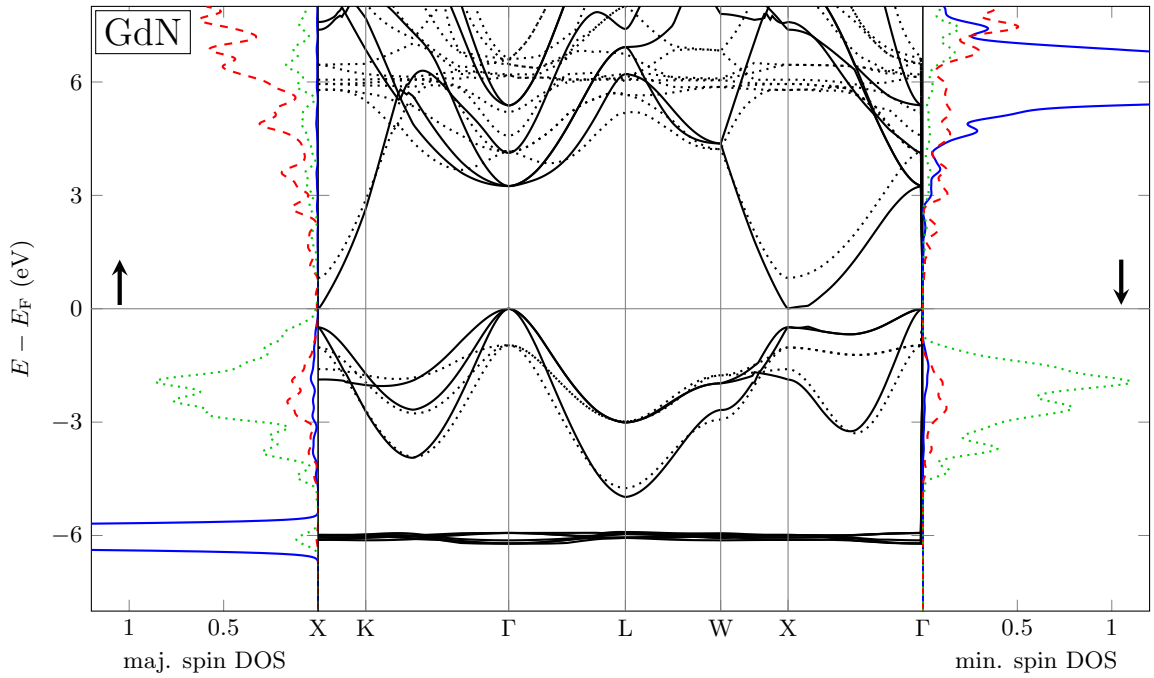

Figure 8: Band structure and density of states (DOS; in states per eV) of GdN at the experimental lattice constant. The majority and minority bands are plotted as solid and dotted lines, respectively. In the DOS, the solid blue line shows the Gd $4f$ states, the red dashed line the Gd $5d$ states, and the green dotted line the N $2p$ states. [69]

$2p$ as well as Gd $5d$ and $6s$ states, respectively. In order to compare our theoretical results with experimental measurements obtained at room temperature, where GdN is in the paramagnetic state, we assume that the exchange splitting and the local magnetic $4f$ moment calculated for the ferromagnetic state at 0 K persist in the paramagnetic state. However, the long-range ordering is lost, and the moments fluctuate resulting in a vanishing macroscopic magnetization. The fluctuating magnetic moments produce a random exchange potential, which effectively leads to electronic single-particle energies that can be approximated by averaging over the corresponding spin-up and spin-down energies of the ferromagnetic phase [118].

In Table 6 we compare the structural and electronic properties calculated with the HSE functional to some of the available experimental [104, 120, 121, 122] and theoretical data, obtained with the hybrid B3LYP functional [119] and within the LSDA+U approach [108, 118, 122]. Our HSE calculations yield a lattice parameter of 4.967 Åin very close agreement to the experiment, while B3LYP and the LSDA+U approach overestimate the value by about 2%. We note that thermal expansion could account for the remaining difference to the experimental lattice parameter, which was determined at the room temperature (whereas the theoretical result corresponds to 0 K). Assuming linear expansion between 0 K and room temperature (293 K) with the thermal expansion coefficient of isostructural and isovalent EuO ($\approx 13 \times 10^{-6}\mathrm{K}^{-1}$; the coefficient of GdN is unknown) [126], one would extrapolate to 4.969 Åat 0 K, which is, indeed, very close to our optimized lattice constant.

Figure 8 shows the spin-resolved band structure and the spin- and orbital-resolved density of

states calculated at the experimental lattice constant. The majority and minority Gd $4f$ states are located at $-6\,\mathrm{eV}$ and $+6\,\mathrm{eV}$, respectively. GdN is in narrow-gap semiconducting ground state with an almost vanishing indirect band gap ($\Gamma \rightarrow \mathrm{X}$) in the majority spin ($0.01\,\mathrm{eV}$), while the minority bands exhibit a robust gap of $1.5\,\mathrm{eV}$. Thus, GdN is just at the border between an insulator and a semimetal. Its electronic properties might change easily depending on the experimental circumstances, which explains the contradicting experimental reports. Upon decreasing the lattice constant isotropically by just 0.02 Å(to the theoretically optimized value), we observe a transition to a half-metallic state or, more precisely, to a semimetallic state just for the majority states, we formally get a negative band-gap value (see Table 6). Duan *et al.* [108] also found this transition but at a much larger lattice constant of 5.63 Å. The proximity of semiconducting and semimetallic states suggest that growth conditions or the lattice expansion upon temperature changes play a decisive role in the transport properties of GdN. Furthermore, upon doping at a small concentration, e.g., with Eu, one might be able to achieve significant charge currents with 100% spin polarization. When the temperature is raised across the Curie temperature, the spin polarization of the charge current disappears and the band gap opens due to the averaged-out exchange potential, giving rise to a possible change of the conductivity by orders or magnitude. A coupling of the electrons to the fluctuating $4f$ moments might also play a role [127]. The band transition energies calculated with our method for the ferromagnetic ($T < T_\mathrm{C}$) and the paramagnetic ($T > T_\mathrm{C}$) state are listed in Table 6. They compare well with the experimental data where available. We note the aforementioned increase of the band gap, both upon increasing the lattice parameter and upon the transition to the paramagnetic state. The partial compensation of the self-interaction error in HSE leads to a pronounced shift of the localized Gd $4f$ majority band to larger binding energies compared to PBE. While the PBE functional yields a much too shallow f majority band, located at $3.1\,\mathrm{eV}$ below the Fermi energy, this band appears at a binding energy of $6.0\,\mathrm{eV}$ in HSE, much closer to its experimentally measured position at $7.8\,\mathrm{eV}$ [105]. We note a very good agreement with the insulating B3LYP result, where the position of the $4f$ peak is located at $6.3\,\mathrm{eV}$ [119].

The ground state of GdN is ferromagnetic (FM), with an experimental Curie temperature of $58\,\mathrm{K}$ [121] and a magnetic moment of $6.88\,\mu_\mathrm{B}$ per Gd atom [104] determined from the saturation magnetization at $1.2\,\mathrm{K}$. The calculated ground state is ferromagnetic, too, with a total magnetic moment of $7\,\mu_\mathrm{B}$, of which $6.99\,\mu_\mathrm{B}$ originates from the Gd muffin-tin sphere. From total-energy differences between ferromagnetic and antiferromagnetic spin configurations, we derive the exchange coupling constants for a Heisenberg spin Hamiltonian, from which the Curie temperature is determined. This is a critical test for the quality of total energies that can be expected from the HSE functional. The classical spin Heisenberg Hamiltonian is given by

$$\mathcal{H} = -\frac{1}{2}\sum_i \mathbf{S}_i \left(J_1 \sum_{j=\mathrm{nn}} \mathbf{S}_j + J_2 \sum_{j=\mathrm{nnn}} \mathbf{S}_j \right) \tag{45}$$

including the nearest-neighbors (nn), and the next-nearest-neighbors (nnn) interaction where J_1 and J_2 are the respective coupling constants with normalized spin vectors $\mathbf{S}_i$ and $\mathbf{S}_j$. The coupling constants are extracted from the differences of the total energies of the ferromagnetic (FM) and two types of antiferromagnetic (AFM) configurations characterized by the planes of ferromagnetically ordered moments that are antiferromagnetically stacked along the crystallo-

	ΔE_I	ΔE_{II}	J_1	J_2	T_C^{MFA}	T_C^{MFA}
This work [69]	8.8	7.6	1.09	0.17	55	42
Duan *et al.* [109]	6.7	4.2	0.84	−0.14	36	26
Mitra *et al.* [106]	3.4	0.4	0.42	−0.36	11	5

Table 7: Total-energies differences for different magnetic configurations [Eq. (46)], the Heisenberg coupling constants, and the corresponding Curie temperatures within the mean-field [Eq. (48)] and the random-phase approximation [Eq. (49)]. Energies and coupling constants are given in meV and the Curie temperatures in K. [69]

graphic [001] or [111] directions (AFM-I and AFM-II, respectively) [109]. For the calculation of the AFM-I (AFM-II) phase, we use an $1 \times 1 \times 2$ ($\sqrt[3]{2} \times \sqrt[3]{2} \times \sqrt[3]{2}$) unit cell. All the calculations are performed at the experimental lattice constant. The Heisenberg coupling constants J_1 and J_2 are obtained from the relations

$$\Delta E_I = E_{\mathrm{AFM,I}} - E_{\mathrm{FM,I}} = 8J_1 \tag{46}$$

$$\Delta E_{II} = E_{\mathrm{AFM,II}} - E_{\mathrm{FM,II}} = 6J_1 - 6J_2\,. \tag{47}$$

The resulting coupling constants shown in Table 7 are both positive, confirming the ferromagnetic nature of the ground state. Compared with previous studies using the LSDA+U method within the FLAPW [109] and LMTO basis [106], our values obtained with HSE yield significantly higher coupling constants and, as a consequence, a higher Curie temperature (T_C), in closer agreement with experiment. The Curie temperature was estimated within two methods: the mean-field approximation (MFA)

$$T_C^{\mathrm{MFA}} = \frac{1}{3k_B}\left(12J_1 + 6J_2\right)\,, \tag{48}$$

yielding $T_C^{\mathrm{MFA}} = 55\,\mathrm{K}$, and the random-phase approximation as described in Refs. 128 and 129

$$T_C^{\mathrm{RPA}} = \frac{1}{3k_B}\left[\int_{\mathrm{BZ}} \frac{d^3q}{J(\mathbf{0}) - J(\mathbf{q})}\right]^{-1}\,, \tag{49}$$

where we evaluate the integral on a discrete mesh of $\mathbf{q}$ points within the Brillouin zone. $J(\mathbf{q})$ is the Fourier transform of the exchange coupling constants defined as

$$J(\mathbf{q}) = \sum_{\mathrm{nn}} J_1 e^{i\mathbf{q}\cdot\mathbf{R}_{\mathrm{nn}}} + \sum_{\mathrm{nnn}} J_2 e^{i\mathbf{q}\cdot\mathbf{R}_{\mathrm{nnn}}}\,, \tag{50}$$

where $\mathbf{R}_{\mathrm{nn}}$ and $\mathbf{R}_{\mathrm{nnn}}$ are the positions of the nearest and the next nearest neighbors, respectively. The resulting $T_C^{\mathrm{RPA}} = 42\,\mathrm{K}$ is smaller than the mean-field estimate, which is not surprising as it is known that the mean-field approximation usually overestimates the Curie temperature. The two theoretical values are in very good agreement with the experimental situation, e.g., $T_C = 68$, 69, 58, or 37 K as reported by Granville *et al.* [113], Khazen *et al.* [130], Leuenberger *et al.* [105], and Yoshitomi *et al.* [131], which vary in value also depending on film thickness, strain, grain size, stoichiometry, and N vacancies [132, 133].

4.4 ZnO – an extreme case for *GW* calculations

In a publication Shih *et al.* [80] presented a new calculation for the band gap of ZnO in the wurtzite structure employing the *GW* approximation [21] for the electronic self-energy in a conventional *one-shot* approach [63, 23] corresponding to Eq. (8). All previous calculations [134, 135, 28, 83] invoking the one-shot LDA+*GW* approach had shown that the band gap of wurtzite ZnO is underestimated with respect to the experimental value by more than 1 eV. They fall in the range 2.12–2.6 eV, while the experimental gap amounts to 3.6 eV, [136] after correction for vibrational effects. This large underestimation is untypical for *GW* calculations of *sp*-bound systems.

Shih *et al.* investigated the convergence of the correlation self-energy and the dielectric matrix with respect to the number of bands. They performed calculations with up to 3000 bands corresponding to a maximal band energy of 67 Ry as well as a cutoff for the dielectric matrix of up to 80 Ry and showed that the resulting *GW* band gaps, 3.4 eV for LDA+*GW* (and 3.6 eV for LDA+*U*+*GW*), turned out to be in very good agreement with experiment. These new results for ZnO are in striking contrast to the other *GW* calculations and seem to indicate that the convergence with respect to the unoccupied states is even more problematic than previously thought. Of course, several points of criticism can be raised. First, the calculation relies on the pseudopotential approximation, in which the numerically important core-valence exchange is neglected, the wave functions are pseudized, and high-lying states are inaccurately described. Second, the study was based on a plasmon-pole model for the dielectric function, which only approximates the full expression of the RPA.

Therefore, we reexamined [81] the one-shot *GW* band gap of wurtzite ZnO with our own code, which neither employs the pseudopotential approximation nor a plasmon-pole model for the dielectric matrix. We employ the contour integration for the frequency convolution in Eq. (7), and Eq. (8) is solved on an energy mesh around $\epsilon^{\sigma}_{n\mathbf{q}}$ with a cubic spline interpolation between the mesh points. We carefully converged the number of empty bands for the calculation of both the polarization function and the correlation self-energy as well as the MPB parameters. While the ground-state electron density was converged with a standard LAPW basis with moderate cutoff parameters ($l_{\max} = 8$, $G_{\max} = 4.3\, a_0^{-1}$, where a_0 is the Bohr radius, and including second-derivative local orbitals [79]), we had to employ much larger cutoffs to generate enough wave functions for the *GW* calculation: $l_{\max} = 12$ and $G_{\max} = 8.0\, a_0^{-1}$. Furthermore, in order to avoid linearization errors in the MT part of the LAPW basis [79, 77], we added local orbitals [137, 76] (LOs) with different angular momentum quantum numbers and energy parameters distributed over the relevant energy range: 292 LOs for Zn (for l = 0-6) and 186 for O (for l = 0-5). We also treat the 3*s* and 3*p* semicore states of Zn explicitly with LOs. We found that relatively modest MPB parameters were sufficient: $L_{\max} = 4$ and $G'_{\max} = 2.4\, a_0^{-1}$. However, we had to include a large number of radial functions in the MT spheres, which after optimization led to 177 MT functions for Zn and 127 for O. Obviously, the rapid variations close to the atomic nuclei must be accurately described. Within the all-electron MPB this is possible with a comparatively small number of MT functions, while in a pure plane-wave approach a very large number of plane waves is necessary to resolve the variations sufficiently. This explains the finding of Shih *et al.* that the dielectric matrix must be converged to very large energy cutoffs. The

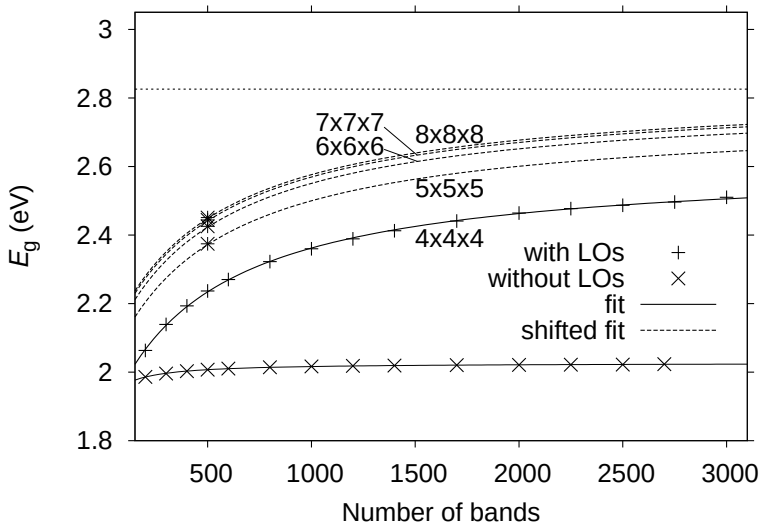

Figure 9: Band convergence of the quasiparticle band gap of ZnO employing a 4×4×4 **k**-point set and calculated with (pluses) and without local orbitals (LOs) (crosses) for high-lying states. The solid lines show hyperbolic fits. We also indicate results with finer **k**-point samplings (stars) calculated with LOs and 500 bands. The dashed lines show the hyperbolic fit shifted to align with these results. The fit asymptote for the 8×8×8 **k**-point set at 2.83 eV (dotted line) is considered the best estimate for the all-electron one-shot *GW* band gap. [81]

total number of MPB functions in the calculations is less than 700 per **k** point. This number is further reduced to around 490 by constructing linear combinations that are continuous in value and radial derivative at the MT sphere boundaries, cmp. Sec. 3.1 and Ref. 39.

Figure 9 shows the quasiparticle band gap of ZnO as a function of the number of states included in the calculation of the polarization function and the correlation self-energy. The calculations were performed with a 4×4×4 **k**-point sampling of the Brillouin zone. There is a large difference between calculations with (pluses) and without the LOs for unoccupied states (crosses), which shows the importance of eliminating the linearization error of the conventional LAPW basis. As the linearization error becomes larger for higher and higher bands, it is not surprising that the difference between the convergence curves grows toward increasing numbers of bands. We find an asymptotic difference of 0.5 eV. The calculations without LOs for unoccupied states show a false convergence behavior, as they seem to converge with a few hundred bands, but toward a much too small value. A similar false convergence behavior was found in Ref. 80 for calculations with underconverged dielectric functions.

As Fig. 9 shows, the calculations with eliminated linearization error (pluses) take far more bands to converge. In fact, even with 3000 bands the band gap is still not completely converged. Therefore, we fitted the values with the hyperbolic function

$$f(N) = \frac{a}{N - N_0} + b \tag{51}$$

where a, b, and N_0 are fit parameters. It is surprising how closely the fitted curve (solid line) follows the calculated data points. This makes us confident in taking the fit asymptote b as the band gap extrapolated to infinite bands. Furthermore, we have recalculated the band gap

with finer **k**-point meshes (up to 8×8×8) and 500 bands (crosses). The dashed lines show correspondingly shifted hyperbolic fits. The asymptote of the fit corresponding to an 8×8×8 **k**-point sampling is found at 2.83 eV, which we take as the final best estimate for the all-electron one-shot *GW* band gap.

This band gap is 0.4–0.9 eV larger than the previously reported values. Both the large number of bands that are needed for proper convergence and the elimination of the linearization error, which has not been undertaken in the previous all-electron studies, are responsible for this large difference. Our value is still about 0.4 eV smaller than the band gap of Shih *et al.*, though. In fact, a certain discrepancy should be expected because of the pseudopotential approximation and the plasmon-pole model for the dielectric function used in Ref. 80. The pseudopotential approximation not only neglects the important contribution of core-valence exchange. It also yields accurate wave functions only in the vicinity of the atomic electron energies, but not for high-lying states. This error is very similar in spirit to the linearization error of the LAPW basis and is also of the same magnitude [79]. Thus, it should have an impact on the *GW* results comparable in size to the linearization error of the LAPW basis.

With the LDA band gap of only 0.73 eV the quasiparticle correction amounts to more than 2 eV. It can be expected that a treatment beyond the one-shot approach, for example, by taking into account offdiagonal elements of the self-energy, by updating the Green function, or by including vertex corrections, will further increase the value and, thus, bring it even closer to the experimental value. As was shown in Ref. 80, already using LDA+U instead of LDA as the mean-field starting point, which corrects the 2p-3d hybridization, gives an upward correction of 0.2 eV in the resulting *GW* band gap. Self-consistency can be simulated in a simplified way by aligning the chemical potential of the LDA starting point in such a way that the ionisation potential (position of the highest occupied state) of the starting point becomes identical to that after the *GW* self-energy correction [138]. In practice, this means that the LDA eigenvalues are all shifted by a constant energy determined by the condition that the self-energy correction for the highest occupied state vanishes. While the LDA band gap trivially remains unchanged, it does influence the *GW* band gap. In the case of ZnO we observe a sizable upward correction by about 0.2 eV toward the experimental value.

5 Conclusions

We have presented details of numerical realizations of the hybrid functionals PBE0 and HSE as well as the *GW* approximation for the electronic self-energy within the all-electron FLAPW method as realized in the FLEUR [75] and SPEX [54] codes. All implementations are based on the all-electron mixed product basis (MPB), which is specifically designed for the representation of wave-function products and retains the full accuracy of the all-electron framework. For example, the six-dimensional integrals for the nonlocal exchange potential (or self-energy) decompose into vector-matrix-vector products in this basis, where the Coulomb matrix must be calculated only once at the beginning of the self-consistent-field cycle. As hybrid-functional and *GW* calculations are notoriously expensive in terms of computation time and memory, we presented ways to accelerate the calculations considerably. As a demonstration, we showed a *GW* calculation

for 128 carbon atoms in a diamond supercell. If inversion symmetry is present, the MPB can be defined in such a way that the Coulomb matrix, the screened interaction (for imaginary frequencies), wave-function products, etc. become real-valued. Spatial and time-reversal symmetries are further exploited (1) to restrict the **k**-point summation for the nonlocal quantities to an irreducible wedge of the BZ and (2) to identify those exchange matrix elements in advance that are zero and need not to be calculated. For the exchange term, the computational cost is considerably reduced by a suitable unitary transformation of the MPB, which makes the Coulomb matrix sparse. The divergence of the bare and the screened interaction potential in the limit $\mathbf{k} \to \mathbf{0}$ is treated analytically, while higher-order corrections can be derived with the help of $\mathbf{k} \cdot \mathbf{p}$ perturbation theory. The anisotropy of the RPA screening at $\mathbf{k} = \mathbf{0}$ is fully taken into account. This procedure gives rise to a fast **k**-point convergence, which is particularly important for the evaluation of the nonlocal quantities in the hybrid functionals and the *GW* method. The short-range nonlocal exchange term for the HSE functional is evaluated by subtracting the corresponding long-range part of exchange from the bare exchange, where we exploit the rapidly converging Fourier series of the long-range interaction potential. This procedure allows constructing the nonlocal HSE potential from PBE0 up to machine precision at a negligible computational cost. We note that this approach is quite general and not restricted to the error function used in the HSE functional. For the correlation part of the *GW* self-energy we can apply an optimization of the MPB that involves a basis transformation to the eigenvectors of the Coulomb matrix. By neglecting eigenvectors with eigenvalues below a certain threshold value we only retain the dominant part of the bare electron-electron interaction. The threshold value then becomes a convergence parameter. This optimization reduces the matrix sizes of response quantities such as the screened interaction, again giving rise to a speed up of the calculation. As a demonstration, we showed CPU timings of calculations, where up to 128 carbon atoms were treated explicitly. Furthermore, we have demonstrated that while a direct iteration of the one-particle equation employing hybrid functionals needs extensively many steps to converge due to the nonlocal exchange potential, a nested density-only and density-matrix iteration scheme accelerates the convergence of the self-consistent-field cycle considerably.

We have analyzed the convergence of the interband transition and total energies with respect to the parameters of the MPB for the example of the PBE0 hybrid functional and found that parameters well below the exact limit with respect to the LAPW basis are sufficient. This makes the MPB an efficient and versatile basis for the calculation of nonlocal two-particle quantities within the FLAPW method.

We have presented results for prototype semiconductors and insulators calculated with the hybrid functional PBE0 and HSE as well as with the *GW* approximation. The resulting gap energies, lattice constants, and bulk moduli for a variety of semiconductors and insulators are consistently closer to experimental measurements than within conventional local xc functionals and compare very well with recent theoretical results obtained with PAW and Gaussian-based methods. We have confirmed the finding of Paier *et al.* [68] that the **k**-point convergence within HSE is comparable to the conventional local PBE functional, whereas in PBE0 much larger **k**-point meshes are necessary.

We have calculated the geometric, electronic, and magnetic properties of the rare-earth compound GdN within the HSE functional. There is an ongoing discussion whether the ground

state is insulating or metallic. In fact, within the HSE functional the ground state is very close to a phase transition: we observe a tiny indirect band gap for the experimental lattice constant at room temperature, which vanishes at the theoretically optimized 0 K lattice constant – the compound becomes half-metallic. The experimentally known band transitions are in good agreement with our theoretical results. Furthermore, we have calculated the coupling constants for the Heisenberg spin Hamiltonian from total-energy differences of ferromagnetic and antiferromagnetic configurations. The resulting Curie temperature of 42 K evaluated in the random-phase approximation is in good agreement with the experimental values varying between 37 and 69 K and gives confidence in the energetics obtained by HSE for different magnetic phases. We note that the HSE functional does not contain an adjustable parameter such as the Hubbard U parameter in LSDA+U calculations.

The band convergence is a serious issue in GW calculations and must be thoroughly dealt with. We have presented results for wurtzite ZnO, which is an extreme case in this respect, and could confirm the main result of a recent GW calculation [80] using the plane-wave pseudopotential approach: the GW band gap of ZnO shows a very slow convergence with respect to the number of states used to construct the polarization function and the correlation self-energy. Furthermore, when high-lying bands are included in the calculation, the linearization error of all-electron approaches becomes another important issue. As we have shown, it can be eliminated systematically within the FLAPW method by augmenting the basis in the MT spheres with LOs (see Ref. 81 for details). In the case of ZnO this procedure yields a correction of about 0.5 eV and brings the calculated band gap (2.83 eV) much closer to experiment than in previous studies.

The numerical approach presented in this article can also be applied to other methods. Recently, we have employed the MPB to solve the optimized-effective-potential (OEP) equation, which yields a local instead of a nonlocal effective potential from the exact Hartree-Fock exchange term [59]. Here, additional contributions from radial Sternheimer solutions can improve the precision and convergence of the density response function significantly [60]. Additional contributions from electron correlation can be considered by using the RPA total energy within the adiabatic-connection fluctuation-dissipation theory, either by a one-shot correction of a preceding DFT calculation or self-consistently by solving the optimized-effective-potential equation. The extension of the numerical procedure to off-diagonal elements of the GW self-energy is straightforward. The quasiparticle equation can then be solved beyond perturbation theory, which also makes self-consistent calculations possible, e.g., employing the quasiparticle self-consistent scheme [102]. When strongly correlated electron systems are studied, one often uses methods that rely on the Hubbard U parameter, which is a measure of the strength of the effective electron-electron interaction in the localized states, such as the LSDA+U method and the dynamical mean-field theory. We have extended our RPA implementation to the constrained RPA (cRPA) approach, with which the Hubbard U parameter defined in a basis of Wannier functions [139] expressed in terms of FLAPW basis functions [140, 141] can be calculated from first principles [142]. A Wannier basis can also be used to represent the four-point T matrix, which describes the correlated motion of an electron-hole pair in terms of ladder diagrams. If the electron and hole are of opposite spin, the two-particle propagation function contains information about the collective spin excitations [143]. These spin waves or magnons can also contribute to the renormalization of quasiparticles. The corresponding self-energy is then approximated by a GT diagram [144].

Acknowledgment

We gratefully acknowledge valuable discussions with Marjana Ležaić, Gustav Bihlmayer, and Mathias C. Müller, as well as financial funding by the Young Investigators Group Programme of the Helmholtz Association ("Computational Nanoferronics Laboratory", Contract VH-NG-409) and by the Deutsche Forschungsgemeinschaft through the Priority Program 1145.

References

[1] P. Hohenberg and W. Kohn, Phys. Rev. **136**, B864 (1964).

[2] C. Fiolhais, F. Noguiera, and M. A. L. Marques, ed., *A Primer in Density Functional Theory*, vol. 620 of *Lecture Notes in Physics* (Springer, Heidelberg, 2003).

[3] W. Kohn and L. J. Sham, Phys. Rev. **140**, A1133 (1965).

[4] D. M. Ceperley and B. J. Alder, Phys. Rev. Lett. **45**, 566 (1980).

[5] S. H. Vosko, L. Wilk, and M. Nusair, Can. J. Phys. **58**, 1200 (1980).

[6] J. P. Perdew, K. Burke, and M. Ernzerhof, Phys. Rev. Lett. **77**, 3865 (1996).

[7] J. P. Perdew and Y. Wang, Phys. Rev. B **33**, 8800 (1986).

[8] J. P. Perdew and M. Levy, Phys. Rev. Lett. **51**, 1884 (1983).

[9] L. J. Sham and M. Schlüter, Phys. Rev. Lett. **51**, 1888 (1983).

[10] A. D. Becke, J. Chem. Phys. **98**, 5648 (1993).

[11] C. Adamo and V. Barone, J. Chem. Phys. **110**, 6158 (1999).

[12] J. Muscat, A. Wander, and N. M. Harrison, Chem. Phys. Letters **342**, 397 (2001).

[13] C. Franchini, V. Bayer, R. Podloucky, J. Paier, and G. Kresse, Phys. Rev. B **72**, 045132 (2005).

[14] T. Bredow and A. R. Gerson, Phys. Rev. B **61**, 5194 (2000).

[15] A. Seidl, A. Görling, P. Vogl, J. A. Majewski, and M. Levy, Phys. Rev. B **53**, 3764 (1996).

[16] A. D. Becke, J. Chem. Phys. **98**, 1372 (1993).

[17] J. P. Perdew, M. Ernzerhof, and K. Burke, J. Chem. Phys. **105**, 9982 (1996).

[18] P. J. Stephens, F. J. Devlin, C. F. Chabalowski, and M. J. Frisch, J. Phys. Chem. **98**, 11623 (1994).

[19] J. Tao, S. Tretiak, and J. Zhu, J. Chem. Phys. **128**, 084110 (2008).

[20] G. D. Mahan, *Many-particle physics* (Plenum, New York, 1990).

[21] L. Hedin, Phys. Rev. **139**, A796 (1965).

[22] R. W. Godby, M. Schlüter, and L. J. Sham, Phys. Rev. Lett. **56**, 2415 (1986).

[23] M. S. Hybertsen and S. G. Louie, Phys. Rev. B **34**, 5390 (1986).

[24] S. Chawla and G. A. Voth, J. Chem. Phys. **108**, 4697 (1998).

[25] N. Hamada, M. Hwang, and A. J. Freeman, Phys. Rev. B **41**, 3620 (1990).

[26] F. Aryasetiawan, Phys. Rev. B **46**, 13051 (1992).

[27] W. Ku and A. G. Eguiluz, Phys. Rev. Lett. **89**, 126401 (2002).

[28] M. Usuda, N. Hamada, T. Kotani, and M. van Schilfgaarde, Phys. Rev. B **66**, 125101 (2002).

[29] T. Kotani and M. van Schilfgaarde, Solid State Commun. **121**, 461 (2002).

[30] A. Yamasaki and T. Fujiwara, Phys. Rev. B **66**, 245108 (2002).

[31] S. V. Faleev, M. van Schilfgaarde, and T. Kotani, Phys. Rev. Lett. **93**, 126406 (2004).

[32] B. Arnaud and M. Alouani, Phys. Rev. B **62**, 4464 (2000).

[33] S. Lebègue, B. Arnaud, M. Alouani, and P. E. Bloechl, Phys. Rev. B **67**, 155208 (2003).

[34] M. Shishkin and G. Kresse, Phys. Rev. B **74**, 035101 (2006).

[35] A. Ernst, M. Lüders, P. Bruno, W. M. Temmerman, and Z. Szotek, unpublished.

[36] V.R. Saunders, R. Dovesi, C. Roetti, M. Causa, N.M. Harrison, R. Orlando, and C.M. Zicovich-Wilson, *CRYSTAL98 User's Manual* (University of Torino, 1998).

[37] J. Paier, R. Hirschl, M. Marsman, and G. Kresse, J. Chem. Phys. **122**, 234102 (2005).

[38] P. Novak, J. Kunes, L. Chaput, and W. E. Pickett, Phys. Stat. Sol. B **243**, 563 (2006).

[39] M. Betzinger, C. Friedrich, and S. Blügel, Phys. Rev. B **81**, 195117 (2010).

[40] S. Massidda, M. Posternak, and A. Baldereschi, Phys. Rev. B **48**, 5058 (1993).

[41] M. Weinert, J. Math. Phys. **22**, 2433 (1981).

[42] F. Tran and P. Blaha, Phys. Rev. B **83**, 235118 (2011).

[43] S. L. Adler, Phys. Rev. **126**, 413 (1962).

[44] J. Harris and R. O. Jones, Journal of Physics F: Metal Physics **4**, 1170 (1974).

[45] O. Gunnarsson and B. I. Lundqvist, Phys. Rev. B **13**, 4274 (1976).

[46] D. C. Langreth and J. P. Perdew, Phys. Rev. B **15**, 2884 (1977).

[47] A. D. Becke, J. Chem. Phys. **104**, 1040 (1996).

[48] J. Heyd, G. E. Scuseria, and M. Ernzerhof, J. Chem. Phys. **118**, 8207 (2003).

[49] B. G. Janesko, T. M. Henderson, and G. E. Scuseria, Phys. Chem. Chem. Phys. **11**, 443 (2009).

[50] E. N. Brothers, A. F. Izmaylov, J. O. Normand, V. Barone, and G. E. Scuseria, J. Chem. Phys. **129**, 011102 (pages 4) (2008).

[51] J. Heyd and G. E. Scuseria, J. Chem. Phys. **120**, 7274 (2004).

[52] A. V. Krukau, O. A. Vydrov, A. F. Izmaylov, and G. E. Scuseria, J. Chem. Phys. **125**, 224106 (pages 5) (2006).

[53] L. Dagens and F. Perrot, Phys. Rev. B **5**, 641 (1972).

[54] C. Friedrich, S. Blügel, and A. Schindlmayr, Phys. Rev. B **81**, 125102 (2010).

[55] E. Wimmer, H. Krakauer, M. Weinert, and A. J. Freeman, Phys. Rev. B **24**, 864 (1981).

[56] M. Weinert, E. Wimmer, and A. J. Freeman, Phys. Rev. B **26**, 4571 (1982).

[57] H. J. F. Jansen and A. J. Freeman, Phys. Rev. B **30**, 561 (1984).

[58] F. Aryasetiawan and O. Gunnarsson, Phys. Rev. B **49**, 16214 (1994).

[59] M. Betzinger, C. Friedrich, S. Blügel, and A. Görling, Phys. Rev. B **83**, 045105 (2011).

[60] M. Betzinger, C. Friedrich, and S. Blügel, Phys. Rev. B (in preparation).

[61] C. Friedrich, A. Schindlmayr, and S. Blügel, Comput. Phys. Commun. **180**, 347 (2009).

[62] H. N. Rojas, R. W. Godby, and R. J. Needs, Phys. Rev. Lett. **74**, 1827 (1995).

[63] R. W. Godby, M. Schlüter, and L. J. Sham, Phys. Rev. B **37**, 10159 (1988).

[64] V. I. Anisimov, ed., *Electronic Structure Calculations in Advances in Condensed Matter Science* (Gordon and Breach, New York, 2000).

[65] G. A. Baker, Jr., *Essentials of Padé Approximants* (Academic Press, New York, 1975).

[66] M. Betzinger, *Efficient implementation of the non-local exchange potential within the flapw method*, Diplomarbeit, RWTH Aachen, Institut für Festkörperphysik, Forschungszentrum Jülich (2007).

[67] S. K. Kim, *Group Theoretical Methods and Applications to Molecules and Crystals* (Cambridge University Press, Cambridge, 1999).

[68] J. Paier, M. Marsman, K. Hummer, G. Kresse, I. C. Gerber, and J. G. Ángyán, J. Chem. Phys. **124**, 154709 (pages 13) (2006); *ibid.* **124**, 249901 (2006).

[69] M. Schlipf, M. Betzinger, C. Friedrich, M. Ležaić, and S. Blügel, Phys. Rev. B **84**, 125142 (2011).

[70] S. Baroni and R. Resta, Phys. Rev. B **33**, 7017 (1986).

[71] C. Freysoldt, P. Eggert, P. Rinke, A. Schindlmayr, R. W. Godby, and M. Scheffler, Comput. Phys. Commun. **176**, 1 (2007).

[72] P. Ziesche and G. Lehmann, ed., *Ergebnisse in der Elektronentheorie der Metalle* (Akademie/Springer Verlag Berlin, 1983).

[73] C. G. Broyden, Math. Comput. **19**, 577 (1965).

[74] C. G. Broyden, Math. Comput. **21**, 368 (1966).

[75] `http://www.flapw.de`.

[76] D. Singh, Phys. Rev. B **43**, 6388 (1991).

[77] E. E. Krasovskii, A. N. Yaresko, and V. N. Antonov, J. Electron Spectrosc. Relat. Phenom. **68**, 157 (1994).

[78] M. L. Tiago, S. Ismail-Beigi, and S. G. Louie, Phys. Rev. B **69**, 125212 (2004).

[79] C. Friedrich, A. Schindlmayr, S. Blügel, and T. Kotani, Phys. Rev. B **74**, 045104 (2006).

[80] B.-C. Shih, Y. Xue, P. Zhang, M. L. Cohen, and S. G. Louie, Phys. Rev. Lett. **105**, 146401 (2010).

[81] C. Friedrich, M. C. Müller, and S. Blügel, Phys. Rev. B **83**, 081101(R) (2011); ibid. **84**, 039906(E) (2011).

[82] F. Bruneval and X. Gonze, Phys. Rev. B **78**, 085125 (2008).

[83] M. Shishkin and G. Kresse, Phys. Rev. B **75**, 235102 (2007).

[84] J. Heyd and G. E. Scuseria, J. Chem. Phys. **121**, 1187 (2004).

[85] K.-H. Hellwege, O. Madelung, M. Schulz, and H. Weiss, eds., *Numerical Data and Functional Relationships in Science and Technology*, vol. 17 & 22 of *Landolt-Börnstein - Group III Condensed Matter* (Springer-Verlag, New York, 1982).

[86] T. C. Chiang and F. J. Himpsel, *Electronic Structure of Solids: Photoemission Spectra and Related Data*, vol. 23 a of *Landolt-Börnstein - Group III Condensed Matter Numerical Data and Functional Relationships in Science and Technology* (Springer Verlag, Berlin, 1989).

[87] J. E. Ortega and F. J. Himpsel, Phys. Rev. B **47**, 2130 (1993).

[88] M. Welkowsky and R. Braunstein, Phys. Rev. B **5**, 497 (1972).

[89] R. Hulthn and N. G. Nilsson, Solid State Commun. **18**, 1341 (1976).

[90] S. Adachi, *Optical Properties of Crystalline and Amorphous Semiconductors: Numerical Data and Graphical Information* (Kluwer Academic, Dordrecht, 1999).

[91] R. T. Poole, J. Liesegang, R. C. G. Leckey, and J. G. Jenkin, Phys. Rev. B **11**, 5190 (1975).

[92] R. J. Magyar, A. Fleszar, and E. K. U. Gross, Phys. Rev. B **69**, 045111 (2004).

[93] G. G. Macfarlane, T. P. McLean, J. E. Quarrington, and V. Roberts, Phys. Rev. **108**, 1377 (1957).

[94] K. O. Magnusson, U. O. Karlsson, D. Straub, S. A. Flodström, and F. J. Himpsel, Phys. Rev. B **36**, 6566 (1987).

[95] H. Okumura, S. Yoshida, and T. Okahisa, Appl. Phys. Lett. **64**, 2997 (1994).

[96] K. van Benthem, C. Elsässer, and R. H. French, J. Appl. Phys. **90**, 6156 (2001).

[97] L. T. Hudson, R. L. Kurtz, S. W. Robey, D. Temple, and R. L. Stockbauer, Phys. Rev. B **47**, 1174 (1993).

[98] Y. Kaneko and T. Koda, J. Cryst. Growth **86**, 72 (1990).

[99] K. Watanabe, T. Taniguchi, and H. Kanda, Nature Mater. **3**, 404 (2004).

[100] R. C. Whited, C. J. Flaten, and W. C. Walker, Solid State Commun. **13**, 1903 (1973).

[101] R. T. Poole, J. G. Jenkin, J. Liesegang, and R. C. G. Leckey, Phys. Rev. B **11**, 5179 (1975).

[102] T. Kotani, M. van Schilfgaarde, and S. V. Faleev, Phys. Rev. B **76**, 165106 (2007).

[103] F. Bechstedt, F. Fuchs, and G. Kresse, Phys. Status Solidi B **246**, 1877 (2009).

[104] D. X. Li, Y. Haga, H. Shida, and T. Suzuki, Physica B: Condensed Matter **199-200**, 631 (1994).

[105] F. Leuenberger, A. Parge, W. Felsch, K. Fauth, and M. Hessler, Phys. Rev. B **72**, 014427 (2005).

[106] C. Mitra and W. R. L. Lambrecht, Phys. Rev. B **78**, 134421 (2008).

[107] A. Sharma and W. Nolting, Phys. Rev. B **81**, 125303 (2010).

[108] C.-G. Duan, R. F. Sabiryanov, J. Liu, W. N. Mei, P. A. Dowben, and J. R. Hardy, Phys. Rev. Lett. **94**, 237201 (2005).

[109] C.-G. Duan, R. F. Sabiryanov, W. N. Mei, P. A. Dowben, S. S. Jaswal, and E. Y. Tsymbal, Appl. Phys. Lett. **88**, 182505 (pages 3) (2006).

[110] C.-G. Duan, R. F. Sabirianov, W. N. Mei, P. A. Dowben, S. S. Jaswal, and E. Y. Tsymbal, J. Phys.: Condens. Matter **19**, 315220 (2007).

[111] P. Wachter and E. Kaldis, Solid State Commun. **34**, 241 (1980).

[112] J. Q. Xiao and C. L. Chien, Phys. Rev. Lett. **76**, 1727 (1996).

[113] S. Granville, B. J. Ruck, F. Budde, A. Koo, D. J. Pringle, F. Kuchler, A. R. H. Preston, D. H. Housden, N. Lund, A. Bittar, et al., Phys. Rev. B **73**, 235335 (2006).

[114] B. M. Ludbrook, I. L. Farrell, M. Kuebel, B. J. Ruck, A. R. H. Preston, H. J. Trodahl, L. Ranno, R. J. Reeves, and S. M. Durbin, J. Appl. Phys. **106**, 063910 (pages 4) (2009).

[115] M. Scarpulla, C. Gallinat, S. Mack, J. Speck, and A. Gossard, J. Cryst. Growth **311**, 1239 (2009).

[116] W. R. L. Lambrecht, Phys. Rev. B **62**, 13538 (2000).

[117] P. Larson and W. R. L. Lambrecht, Phys. Rev. B **74**, 085108 (2006).

[118] P. Larson, W. R. L. Lambrecht, A. Chantis, and M. van Schilfgaarde, Phys. Rev. B **75**, 045114 (2007).

[119] K. Doll, J. Phys.: Condens. Matter **20**, 075214 (2008).

[120] R. C. Brown and N. J. Clark, J. Inorg. Nucl. Chem. **36**, 2507 (1974).

[121] U. Rössler and D. Strauch, *Group IV Elements, IV-IV and III-V Compounds. Part a - Lattice Properties*, vol. 41A1a of *Landolt-Börnstein - Group III Condensed Matter* (Springer-Verlag, Berlin, 2001).

[122] H. J. Trodahl, A. R. H. Preston, J. Zhong, B. J. Ruck, N. M. Strickland, C. Mitra, and W. R. L. Lambrecht, Phys. Rev. B **76**, 085211 (2007).

[123] B. N. Harmon, V. P. Antropov, A. I. Liechtenstein, I. V. Solovyev, and V. I. Anisimov, J. Phys. Chem. Solids **56**, 1521 (1995); proceedings of the 1994 Conference on Magneto-optic Materials.

[124] F. Hullinger, *Handbook on the Physics and Chemistry of Rare Earths*, vol. 4 (North-Holland Physics Publishing, New York, 1979).

[125] H. Yamada, T. Fukawa, T. Muro, Y. Tanaka, S. Imada, S. Suga, D.-X. Li, and T. Suzuki, J. Phys. Soc. Jpn. **65**, 1000 (1996).

[126] F. Lévy, Phys. Kondens. Mater. **10**, 71 (1969).

[127] M. Arnold and J. Kroha, Phys. Rev. Lett. **100**, 046404 (2008).

[128] N. N. Bogoliubov and S. V. Tyablikov, Dokl. Akad. Nauk SSSR **126**, 53 (1959).

[129] U. Nowak, in *Magnetism goes Nano*, edited by S. Blügel, T. Brückel, and C. M. Schneider (Forschungszentrum Jülich, Jülich, 2005), vol. 26 of *Matter and Materials*, p. A3.1.

[130] K. Khazen, H. J. von Bardeleben, J. L. Cantin, A. Bittar, S. Granville, H. J. Trodahl, and B. J. Ruck, Phys. Rev. B **74**, 245330 (2006).

[131] H. Yoshitomi, S. Kitayama, T. Kita, O. Wada, M. Fujisawa, H. Ohta, and T. Sakurai, Phys. Rev. B **83**, 155202 (2011).

[132] K. Senapati, T. Fix, M. E. Vickers, M. G. Blamire, and Z. H. Barber, Phys. Rev. B **83**, 014403 (2011).

[133] A. Punya, T. Cheiwchanchamnangij, A. Thiess, and W. R. L. Lambrecht, MRS Proceedings **1290** (2011).

[134] F. Fuchs, J. Furthmüller, F. Bechstedt, M. Shishkin, and G. Kresse, Phys. Rev. B **76**, 115109 (2007).

[135] P. Gori, M. Rakel, C. Cobet, W. Richter, N. Esser, A. Hoffmann, R. Del Sole, A. Cricenti, and O. Pulci, Phys. Rev. B **81**, 125207 (2010).

[136] S. Tsoi, X. Lu, A. K. Ramdas, H. Alawadhi, M. Grimsditch, M. Cardona, and R. Lauck, Phys. Rev. B **74**, 165203 (2006).

[137] E. Sjöstedt, L. Nordström, and D. J. Singh, Solid State Commun. **114**, 15 (2000).

[138] T. J. Pollehn, A. Schindlmayr, and R. W. Godby, J. Phys.: Condens. Matter **10**, 1273 (1998).

[139] N. Marzari and D. Vanderbilt, Phys. Rev. B **56**, 12847 (1997).

[140] F. Freimuth, Y. Mokrousov, D. Wortmann, S. Heinze, and S. Blügel, Phys. Rev. B **78**, 035120 (2008).

[141] J. Kuneš, R. Arita, P. Wissgott, A. Toschi, H. Ikeda, and K. Held, Computer Physics Communications **181**, 1888 (2010).

[142] E. Şaşıoğlu, C. Friedrich, and S. Blügel, Phys. Rev. B **83**, 121101 (2011).

[143] E. Şaşıoğlu, A. Schindlmayr, C. Friedrich, F. Freimuth, and S. Blügel, Phys. Rev. B **81**, 054434 (2010).

[144] M. C. Müller, *Electron-magnon interaction in the GT approximation*, Master's thesis, Peter Grünberg Institut, Forschungszentrum Jülich, 52425 Jülich (2011), in preparation.